

# Computational Modeling and Optimization of Proton Exchange Membrane Fuel Cells

by

Marc Secanell Gallart

Bachelor in Engineering, Universitat Politècnica de Catalunya, 2002

Masters of Applied Sciences, University of Victoria, 2004

A Thesis Submitted in Partial Fulfillment of the  
Requirements for the Degree of  
**DOCTOR IN PHILOSOPHY**  
in the  
Department of Mechanical Engineering.

© MARC SECANELL GALLART, 2007

University of Victoria

All rights reserved. This thesis may not be reproduced in whole or in part, by  
photocopy or other means, without the permission of the author.

# Computational Modeling and Optimization of Proton Exchange Membrane Fuel Cells

by

Marc Secanell Gallart

Bachelor in Engineering, Universitat Politècnica de Catalunya, 2002

Masters of Applied Sciences, University of Victoria, 2004

## Supervisory Committee

Dr. Ned Djilali, Supervisor (Dept. of Mechanical Engineering,  
University of Victoria)

Dr. Afzal Suleman, Supervisor (Dept. of Mechanical Engineering,  
University of Victoria)

Dr. Bradley Buckham, Departmental Member (Dept. of Mechanical Engineering,  
University of Victoria)

Dr. Wu-Sheng Lu, Outside Member (Dept. of Electrical and Computer Engineering,  
University of Victoria)

Dr. Michael Eikerling, External Examiner (Dept. of Chemistry,  
Simon Fraser University)

## Supervisory Committee

Dr. Ned Djilali, Supervisor (Dept. of Mechanical Engineering,  
University of Victoria)

Dr. Afzal Suleman, Supervisor (Dept. of Mechanical Engineering,  
University of Victoria)

Dr. Bradley Buckham, Departmental Member (Dept. of Mechanical Engineering,  
University of Victoria)

Dr. Wu-Sheng Lu, Outside Member (Dept. of Electrical and Computer Engineering,  
University of Victoria)

Dr. Michael Eikerling, External Examiner (Dept. of Chemistry,  
Simon Fraser University)

## Abstract

Improvements in performance, reliability and durability as well as reductions in production costs, remain critical prerequisites for the commercialization of proton exchange membrane fuel cells. In this thesis, a computational framework for fuel cell analysis and optimization is presented as an innovative alternative to the time consuming trial-and-error process currently used for fuel cell design. The framework is based on a two-dimensional through-the-channel isothermal, isobaric and single phase membrane electrode assembly (MEA) model. The model input parameters are the manufacturing parameters used to build the MEA: platinum loading, platinum to carbon ratio, electrolyte content and gas diffusion layer porosity. The governing equations of the fuel cell model are solved using Netwon's algorithm and an adaptive finite element method in order to achieve quadratic convergence and a mesh independent solution respectively. The analysis module is used to solve two optimization problems: i) maximize performance; and, ii) maximize performance while minimizing

the production cost of the MEA. To solve these problems a gradient-based optimization algorithm is used in conjunction with analytical sensitivities. The presented computational framework is the first attempt in the literature to combine highly efficient analysis and optimization methods to perform optimization in order to tackle large-scale problems. The framework presented is capable of solving a complete MEA optimization problem with state-of-the-art electrode models in approximately 30 minutes. The optimization results show that it is possible to achieve Pt-specific power density for the optimized MEAs of  $0.422 \text{ g}_{Pt}/kW$ . This value is extremely close to the target of  $0.4 \text{ g}_{Pt}/kW$  for large-scale implementation and demonstrate the potential of using numerical optimization for fuel cell design.

# Table of Contents

<b>Supervisory Committee</b>	<b>ii</b>
<b>Abstract</b>	<b>iii</b>
<b>Table of Contents</b>	<b>v</b>
<b>List of Tables</b>	<b>vii</b>
<b>List of Figures</b>	<b>viii</b>
<b>Nomenclature</b>	<b>xii</b>
<b>Acknowledgements</b>	<b>xv</b>
<b>1 Introduction</b>	<b>1</b>
1.1 Background and motivation . . . . .	1
1.2 Literature review . . . . .	2
1.2.1 Mathematical modeling of proton exchange membrane fuel cells	3
1.2.2 Numerical optimization . . . . .	15
1.2.3 Sensitivity analysis . . . . .	19
1.2.4 Numerical optimization of PEM fuel cells . . . . .	22
1.3 Contributions . . . . .	25
1.4 Structure of the thesis . . . . .	26
<b>2 PEM fuel cell modeling</b>	<b>27</b>
2.1 Cathode electrode modeling . . . . .	28
2.1.1 Governing equations . . . . .	28
2.1.2 Numerical solution . . . . .	56
2.2 Membrane modeling . . . . .	64
2.2.1 Governing equations . . . . .	64
2.2.2 Numerical solution . . . . .	72
2.3 Anode electrode modeling . . . . .	74
2.3.1 Governing equations . . . . .	74

2.4	Membrane electrode assembly (MEA) modeling . . . . .	77
2.4.1	Governing equations . . . . .	77
2.4.2	Computational domain and boundary conditions . . . . .	79
2.4.3	Input parameters . . . . .	83
2.5	Validation of the numerical code . . . . .	87
2.5.1	Grid study . . . . .	89
2.5.2	Experimental validation . . . . .	91
2.5.3	Numerical validation and performance evaluation . . . . .	93
2.6	Numerical results and parametric studies . . . . .	95
2.6.1	Transport processes inside the MEA . . . . .	95
2.6.2	Effect of catalyst layer structure: agglomerate vs. pseudo-homogeneous models . . . . .	105
2.6.3	Effect of the gas diffusion layer anisotropy . . . . .	108
<b>3</b>	<b>Membrane electrode assembly optimization</b>	<b>113</b>
3.1	Problem formulation . . . . .	113
3.1.1	Objective function . . . . .	114
3.1.2	Design variables . . . . .	115
3.1.3	Optimization of the MEA performance . . . . .	116
3.1.4	Optimization of the MEA cost and performance . . . . .	117
3.2	Sensitivity analysis . . . . .	120
3.3	Design and optimization numerical framework . . . . .	122
3.4	Optimization results . . . . .	125
3.4.1	Optimization of the MEA performance . . . . .	125
3.4.2	Optimization of the MEA performance and cost . . . . .	142
<b>4</b>	<b>Conclusions and outlook</b>	<b>151</b>
4.1	Conclusions . . . . .	151
4.2	Outlook . . . . .	154
	<b>References</b>	<b>159</b>

## List of Tables

2.1	Sample percolation threshold for different three-dimensional, $d = 3$ , lattices. Data from [110] . . . . .	55
2.2	Membrane electrode assembly geometry and operating conditions . . . . .	84
2.3	Anode gas diffusion layer and catalyst layer physical and electrochemical properties . . . . .	86
2.4	Membrane physical and electrochemical properties . . . . .	87
2.5	Cathode gas diffusion layer and catalyst layer physical and electrochemical properties . . . . .	88
3.1	Initial upper and lower bounds for the design parameters used to optimize the MEA . . . . .	117
3.2	Analytic vs. numeric sensitivities of the current density with respect to the different design variables . . . . .	123
3.3	Base and optimal design at different voltages . . . . .	135
3.4	Base and optimal design starting from different initial designs . . . . .	137
3.5	Base and optimal design at different voltages . . . . .	138
3.6	Catalyst layer volume fractions for base and optimal design. Obtained from equations (2.50), (2.51), (2.52); and, (2.55) . . . . .	139
3.7	Weights used to obtain Pareto optimal solutions . . . . .	142

# List of Figures

1.1	Schematic showing the various layers in a PEMFC and the main transport processes and electrochemical reactions. . . . .	4
1.2	3D schematic of a single channel PEMFC. Red rectangle shows the computational domain of a through-the-channel model. Green rectangle shows the computational domain of an along-the-channel model. . . . .	7
2.1	Curve fit used to estimate the catalyst active area per mass of catalyst	37
2.2	Catalyst layer and gas diffusion layer microstructure, [100] . . . . .	38
2.3	Agglomerate and thin film structure, [100] . . . . .	39
2.4	Definition of a lattice, an occupied site and a cluster. (a) part of a square lattice, (b) a square lattice with several occupied sites, (c) two clusters of different sizes on the lattice, represented by the circle. Figure from reference [103] . . . . .	49
2.5	Percolation lattice of a SOFC anode catalyst layer. The black, grey and white circles represent electric conductor or carbon grains, electrolyte and pores respectively. The two solid lines show the current's path through the system. The dashed line is the fuel path to the reaction site. Figure from reference [111] . . . . .	51
2.6	Curve fit to the experimental data reported by Pantea et al. [115] . . . . .	54
2.7	Diffusion coefficient for different membrane water content at $80^{\circ}C$ . . . . .	67
2.8	Sorption isotherm for water uptake from water vapour by Nafion <sup>TM</sup> , Aciplex <sup>TM</sup> or Flemion <sup>TM</sup> membranes with similar EW of any form at $80^{\circ}C$ . . . . .	70
2.9	Computational domain and initial grid used to solve the equations of the MEA model . . . . .	80
2.10	Grid study at medium current densities. The solid and dashed lines show the evolution of the current density as the grid is both adaptively and globally refined, respectively. . . . .	90
2.11	Grid study at high current densities. The solid and dashed lines show the evolution of the current density as the grid is both adaptively and globally refined, respectively. . . . .	91

2.12	Polarization curves from experimental data and numerical data at 75% and 100% RH . . . . .	93
2.13	Polarization curves obtained with the code developed (FCST) in this thesis and COMSOL . . . . .	94
2.14	Contour plots of the hydrogen mole fraction, electrolyte phase water content, overpotential and volumetric current density in the anode catalyst layer at a voltage across the MEA of 0.4V . . . . .	97
2.15	Contour plots of the oxygen mole fraction, electrolyte phase water content, overpotential and volumetric current density in the cathode catalyst layer at a voltage across the MEA of 0.4V . . . . .	97
2.16	Contour plots of the relative humidity in the anode and cathode GDL and CL, and membrane and CL electrolyte water content at a voltage across the MEA of 0.4V . . . . .	98
2.17	Contour plots of the hydrogen mole fraction, electrolyte phase water content, overpotential and volumetric current density in the anode catalyst layer at a voltage across the MEA of 0.6V . . . . .	100
2.18	Contour plots of the oxygen mole fraction, electrolyte phase water content, overpotential and volumetric current density in the cathode catalyst layer at a voltage across the MEA of 0.6V . . . . .	100
2.19	Contour plots of the relative humidity in the anode and cathode GDL and CL, and membrane and CL electrolyte water content at a voltage across the MEA of 0.6V . . . . .	101
2.20	Contour plots of the hydrogen mole fraction, electrolyte phase water content, overpotential and volumetric current density in the anode catalyst layer at a voltage across the MEA of 0.8V . . . . .	103
2.21	Contour plots of the oxygen mole fraction, electrolyte phase water content, overpotential and volumetric current density in the cathode catalyst layer at a voltage across the MEA of 0.8V . . . . .	103
2.22	Contour plots of the relative humidity in the anode and cathode GDL and CL, and membrane and CL electrolyte water content at a voltage across the MEA of 0.8V . . . . .	104
2.23	Contour plots of the solid phase potential in the anode and cathode GDL and CL, the CL and membrane electrolyte phase potential at a voltage across the MEA of 0.8V . . . . .	105
2.24	Polarization curves obtained using a pseudo-homogeneous (Case1) model and an agglomerate model (Case 2) . . . . .	107
2.25	Polarization curves for the base case model with anisotropic and isotropic GDL . . . . .	110
2.26	Polarization curves for the base case model with anisotropic and isotropic GDL diffusivities . . . . .	110
2.27	Polarization curves for the base case model with an anisotropic and isotropic GDL conductivities . . . . .	111

2.28	Reactant concentrations and volumetric current densities in anode (left) and cathode (right) when the GDL is considered anisotropic (top) and isotropic (bottom). . . . .	112
3.1	Implementation of the multivariable optimization framework with adaptive refinement and analytic sensitivities. 124	
3.2	Evolution of the objective function and design variables during the optimization process for a voltage across the electrode of 0.4V, i.e. a cell voltage of 0.793 V. . . . .	127
3.3	Polarization curve for the base case and for the optimal design for a voltage across the electrode of 0.4V, i.e. a cell voltage of 0.793 V. . .	127
3.4	Contour lines for the optimized electrode design at $dV = 0.4V$ of of anode CL volumetric current density [ $A/cm^3$ ] (left), CL and membrane potential in the electrolyte [V] (center) and cathode CL volumetric current density [ $A/cm^3$ ] (right). . . . .	128
3.5	Evolution of the objective function and design variables during the optimization process for a voltage across the electrode of 0.6V, i.e. a cell voltage of 0.593 V. . . . .	130
3.6	Polarization curve for the base case and for the optimal design for a voltage across the electrode of 0.6V, i.e. a cell voltage of 0.593 V. . .	130
3.7	Contour lines for the optimized electrode design at $dV = 0.6V$ of of anode CL volumetric current density [ $A/cm^3$ ] (left), CL and membrane potential in the electrolyte [V] (center) and cathode CL volumetric current density [ $A/cm^3$ ] (right). . . . .	131
3.8	Polarization curve for the base case and for the optimal design for a voltage across the electrode of 0.6V and 0.8V, i.e. a cell voltage of 0.593 and 0.393 V. . . . .	133
3.9	Contour lines for the optimized electrode design at $dV = 0.8V$ of of anode CL volumetric current density [ $A/cm^3$ ] (left), CL and membrane potential in the electrolyte [V] (center) and cathode CL volumetric current density [ $A/cm^3$ ] (right). . . . .	134
3.10	Pareto front at three different operating conditions. . . . .	143
3.11	Evolution of the objectives (left) and the design variables (right) during the multiobjective optimization problem with $w_1 = 0.75$ and $w_2 = 0.25$ at an operating voltage of $dV = 0.6V$ . . . . .	144
3.12	Pareto front (left) and the set of weights used to obtain the Pareto front (right) at operating condition of $dV = 0.6V$ . . . . .	145
3.13	Cathode design variable values for the design given by weight sets 1 to 4 at operating conditions of $dV = 0.4, 0.6$ and $0.8V$ . . . . .	147

3.14 Cathode CL solid, void and electrolyte phase volume fractions for the design given by weight sets 1 to 4 at operating conditions of $dV = 0.4, 0.6$ and $0.8V$ . . . . .	147
3.15 Anode design variable values for the design given by weight sets 1 to 4 at operating conditions of $dV = 0.4, 0.6$ and $0.8V$ . . . . .	149
3.16 Anode CL solid, void and electrolyte phase volume fractions for the design given by weight sets 1 to 4 at operating conditions of $dV = 0.4, 0.6$ and $0.8V$ . . . . .	149

# Nomenclature

$A_0$	catalyst surface area per unit mass of the catalyst particle, [ $cm^2 \cdot g^{-1}$ ]
$A_v$	specific reaction surface area per volume of catalyst layer, [1/cm]
$a_w$	water activity, [-]
$c_{H_2}^{Nafion}$	concentration of hydrogen dissolved in the Nafion <sup>TM</sup> , [ $mol \cdot cm^{-3}$ ]
$c_{H_2}^{ref}$	reference hydrogen concentration, [ $mol \cdot cm^{-3}$ ]
$c_{O_2}^{ref}$	concentration of oxygen, [ $mol \cdot cm^{-3}$ ]
$c_g$	concentration of the gas mixture, [ $mol \cdot cm^{-3}$ ]
$c_{O_2,l-s}$	concentration of dissolved oxygen at the electrolyte solid interface, [ $mol \cdot cm^{-3}$ ]
$c_{O_2,g-l}$	concentration of oxygen dissolved in the Nafion <sup>TM</sup> , [ $mol \cdot cm^{-3}$ ]
$D^{eff}$	effective oxygen diffusion coefficient inside the agglomerate, [ $cm^2 \cdot s^{-1}$ ]
$D_\lambda$	water diffusion coefficient, [ $cm^2 \cdot s^{-1}$ ]
$D_i$	diffusivity of the gas in the absence of network constraints, [ $cm^2 \cdot s^{-1}$ ]
$D_i^{eff}$	effective diffusivity of component $i$ of the catalyst layer, [ $cm^2 \cdot s^{-1}$ ]
$D_{O_2,N}$	diffusion coefficient of oxygen in Nafion <sup>TM</sup> , [ $cm^2 \cdot s^{-1}$ ]
$dV$	applied voltage to the electrolyte, [V]
$E_r$	effectiveness factor, [-]
$F$	Faraday constant, 96493 [ $C \cdot mol^{-1}$ ]
$H_{H_2,N}$	Henry's law coefficient for the hydrogen in Nafion <sup>TM</sup> , [ $\frac{Pa \cdot cm^3}{mol}$ ]
$H_{O_2,N}$	Henry's law coefficient for the oxygen in Nafion <sup>TM</sup> , [ $\frac{Pa \cdot cm^3}{mol}$ ]

$i$	current density, [ $A \cdot cm^{-2}$ ]
$i_0^{ref}$	exchange current density, [ $A/cm^{-2}$ ]
$k_c$	reaction rate constant, [ $s^{-1}$ ]
$L$	length of the catalyst layer, [cm]
$m_{Pt}$	platinum mass loading per unit area in the catalyst layer, [ $g \cdot cm^{-2}$ ]
$n$	number of agglomerates per unit volume, [ $\mu m^{-3}$ ]
$n_d$	electro-osmotic drag coefficient, [-]
$p$	total pressure of the mixture, [Pa]
$p_{H_2}$	hydrogen partial pressure, [Pa]
$p_{O_2}$	oxygen partial pressure, [Pa]
$p_{sat}$	saturation pressure, [Pa]
$PtC$	mass percentage of platinum catalyst on the support carbon black, [-]
$R$	gas constant, $8.315 [J \cdot K^{-1} \cdot mol^{-1}]$
$r_{agg}$	radius of the agglomerate, [ $\mu m$ ]
$R_{O_2}$	oxygen reaction rate, [ $mol \cdot cm^{-2} s^{-1}$ ]
$S_{agg}$	surface of the agglomerate, [ $cm^2$ ]
$T$	temperature, [K]
$x_{O_2}$	oxygen mole fraction, [-]
$x_w$	water vapour mole fraction, [-]

### Greek Letters

$\alpha_a$	anodic reaction transfer coefficient, [-]
$\alpha_c$	cathodic reaction transfer coefficient, [-]
$\delta_{agg}$	thin electrolyte film surrounding the agglomerate, [ $\mu m$ ]
$\epsilon_N^{cl}$	electrolyte phase volume fraction in the catalyst layer, [-]
$\epsilon_S^{cl}$	solid phase volume fraction in the catalyst layer, [-]

$\epsilon_V^{cl}$	porosity or void volume fraction in the catalyst layer, [-]
$\epsilon_S^{gdl}$	solid phase volume fraction in the GDL, [-]
$\epsilon_V^{gdl}$	porosity or void volume fraction in the GDL, [-]
$\epsilon_{agg}$	volume fraction of ionomer inside the agglomerate, [-]
$\epsilon_{th}$	percolation threshold for the lattice that represents the catalyst layer, [-]
$\gamma$	coefficient in Butler-Volmer equation, [-]
$\gamma$	coefficient in Tafel equation, [-]
$\lambda$	membrane water content, [-]
$\phi_L$	Thiele's modulus, [-]
$\phi_m$	membrane potential, [V]
$\phi_S$	solid phase potential, [V]
$\rho_c$	carbon density, [ $g \cdot cm^{-3}$ ]
$\rho_{Pt}$	platinum density, [ $g \cdot cm^{-3}$ ]
$\sigma_m$	proton conductivity of the pure electrolyte, [ $S \cdot cm^{-2}$ ]
$\sigma_m^{eff}$	effective proton conductivity of the catalyst layer, [ $S \cdot cm^{-2}$ ]
$\sigma_S$	electron conductivity of the pure electronic conductor material, usually carbon black, [ $S \cdot cm^{-2}$ ]
$\sigma_S^{eff}$	effective electron conductivity of the catalyst layer, [ $S \cdot cm^{-2}$ ]

# Acknowledgements

I would like to thank my supervisors Dr. Ned Djilali and Dr. Afzal Suleman for affording me the opportunity to be a part of their research group and for their support and encouragement during the initial stages of my thesis. Thanks also to: Dr. Kunal Karan at Queen's University for the many helpful discussions on catalyst layer modeling and design, and for inviting me to visit the Fuel Cell Research Center in Kingston; Dr. Brian Carnes for introducing me to deal.ii and; Dr. Guido Kanschat at Texas A&M University, for granting me access to his PDE solver, and for his many helpful suggestions regarding finite elements and deal.ii.

Among my fellow graduate students, I would like to give special thanks to Ron Songprakorp for the many helpful discussions on fuel cell modeling and for developing a similar version of my model in COMSOL, and to Dr. Gonçalo Pedro. I would also like to thank my office mates Erik Kjeang and Aimy Bazylak, as well as all the members of the Computational Fuel Cell Engineering and the Advanced Vehicle Technologies groups. Thank you for sharing with me your enthusiasm for research and all your expertise. Your support and companionship made these years of graduate school an amazing experience.

Last but not least, I thank my wife, Tabitha Gillman, for her emotional support and for all those long nights spent reviewing my writing. Thanks also to my parents, Josep and Concepció, for giving me the opportunities and encouragement to learn. Without them this thesis would never have been written.

*To my family*

# Chapter 1

## Introduction

### 1.1 Background and motivation

The success of PEMFC as a competitive energy conversion device will depend upon the advances made in the next decade in PEMFC design; therefore, much research in this area is needed. PEMFC design is not an easy task because PEMFC performance depends on a large number of coupled physical phenomena such as fluid flow, heat, mass and charge transport, and electrochemical processes. These coupled processes are controlled by a large number of physical parameters that might have competing effects on the different physical phenomena. For instance, changing a specific parameter may help the mass transport but reduce reaction kinetics. For this reason, in order to obtain an optimal PEMFC design, all design parameters must be varied simultaneously during the design process. This can readily be done using graphical techniques and parametric studies when the number of design parameters is one or two at the most. However, when the number of parameters increases, it becomes practically impossible to obtain an optimal design using these techniques, and more sophisticated optimization methodologies are required. More sophisticated techniques for optimal design have been developed in other research areas such as

aerospace [1–4] and structural and engineering design [5, 6], but they have yet to be introduced to fuel cell design.

The objective of this thesis is to develop modeling tools and optimization techniques for fuel cell design. In particular, this work is aimed at developing and demonstrating the suitability of a fuel cell optimization framework. This framework will enable researchers to achieve optimal fuel cell designs with a large number of design parameters. In said framework, high-fidelity fuel cell models will be used in conjunction with numerical optimization techniques in order to manipulate the large design space, to achieve an optimal design in a reasonable amount of time. The high-fidelity fuel cell models will provide an accurate prediction of the fuel cell performance, while the numerical optimization algorithm will allow the framework to effectively vary the large number of different PEMFC design parameters in order to achieve optimal fuel cell performance.

## 1.2 Literature review

In order to develop a fuel cell optimal design framework, it is necessary to couple a mathematical fuel cell model with an optimization algorithm. The following sections present a literature review of both fuel cell mathematical modeling and numerical optimization. If gradient-based optimization algorithms are used, in addition to the optimization algorithm, it is necessary to obtain the sensitivities of the objective functions and constraints with respect to the design parameters. Therefore, a literature review in sensitivity analysis is also included. Finally, a review of the very few developments in the area of optimization of fuel cells is presented.

### 1.2.1 Mathematical modeling of proton exchange membrane fuel cells

Fuel cell modeling has received a lot of attention in the past two decades and a large number of fuel cell models have appeared in the literature. All these fuel cell models aim at predicting the behavior of the fuel cell by examining the phenomena occurring inside the fuel cell and, in particular, in each one of its regions.

Fuel cell models range from empirical to physical models [7,8]. Empirical models such as the ones in references [9,10] use an algebraic equation to fit specific polarization curves by using the coefficients of the algebraic expression as fitting parameters. These types of models are extremely useful for fuel cell stack design when more complex models become intractable; however they are able to predict only the behavior of the specific fuel cell used to obtain the empirical relations. Thus, they lack the predictive power necessary for fuel cell design. Physical or mechanistic models, on the other hand, account for the key physical processes that occur inside a fuel cell using basic principles (e.g. conservation) in conjunction with some empirical determined model constants; therefore, they can be used to design and predict the performance of new fuel cells.

Physical models can be classified according to several criteria such as dimensionality [7,8], number of layers the model takes into account, and if it accounts for single or two-phase flow. However, in most cases, the main difference between published models lies in the methodology used to explain the physical phenomena taking place in a specific region of the fuel cell or in the assumptions made regarding water and heat management. For this reason, this literature review is divided into four sections corresponding to each fuel cell region or layer as it is shown in Figure 1.1 and one final section that discusses heat management.

A PEMFC consists of four main components: the bipolar plate, which contain the current collectors and gas channels; the gas diffusion layer (GDL); the catalyst layer

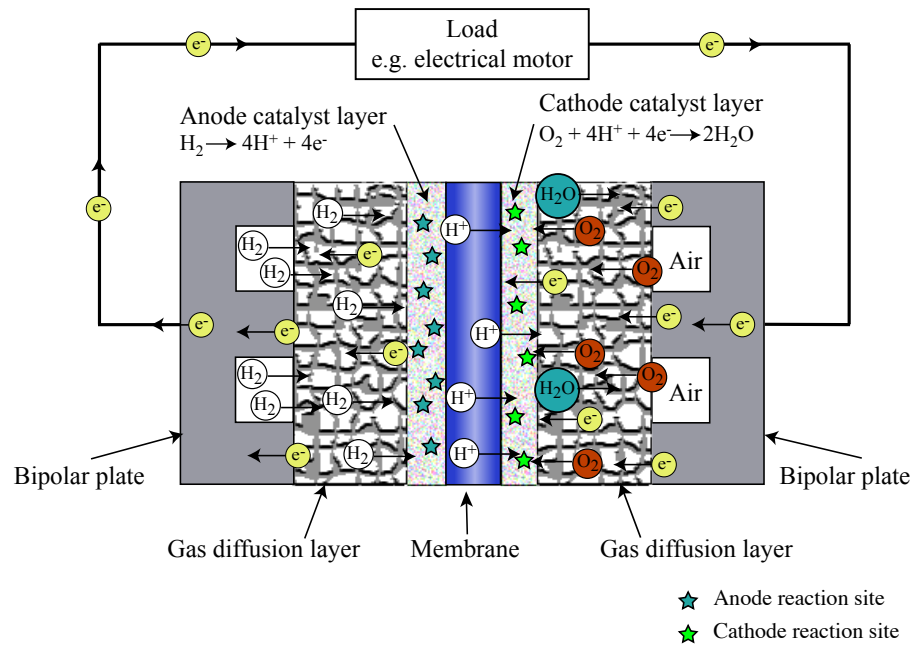


Figure 1.1: Schematic showing the various layers in a PEMFC and the main transport processes and electrochemical reactions.

(CL) or active gas diffusion layer, and; the proton exchange membrane as shown in Figure 1.1. The system formed by the two GDLs, the two CLs and the membrane is known as the membrane electrode assembly (MEA). In the following subsections, a short description is given of the composition and the physical phenomena taking place in each layer as well as a brief outline of the most relevant literature. Because this thesis is focused on optimization of the composition of PEM electrodes (i.e. GDL and catalyst layer) using high-fidelity steady-state two-dimensional models, only one or two-dimensional steady-state models and GDL and catalyst layer models are described in detail. More general fuel cell reviews can be found in references [7, 8, 11–13]

## Bipolar plate

The bipolar plates are made of a highly conductive material such as carbon, graphite or conductive metals and are responsible for

- collecting and transporting electrons from the cell to an external electrical circuit.
- transporting part of the product heat to the environment and to the cooling section of a stack.

Bipolar plates are not usually included in fuel cell models because it is usually assumed that they have very high electronic and thermal conductivities, therefore they usually enter the model only as boundary conditions.

The gas channels are small grooves made by engraving or milling the surface of the bipolar plates, and they are responsible for the transport of fuel and reactants throughout the cell. They also play a key role in water management by controlling the fuel and reactant pressure drop. A large number of gas channels have been designed using a variety of shapes and construction techniques [14]. The gas channels are usually included in three-dimensional models and two-dimensional models that have their  $x$  and  $y$  axes across the cell and in the direction of the flow channel respectively. The latter two-dimensional models are usually referred to as along-the-channel models and their domain is illustrated in Figure 1.2 as a green rectangle. On the other hand, gas channels are not considered in one-dimensional and two-dimensional models that have their axes across the MEA and perpendicular to the gas channel. The latter two-dimensional models are usually referred to as through or across-the-channel models. The red rectangle in Figure 1.2 illustrates their domain. Figure 1.2 also shows a detailed schematic with the layers that are modeled using a through-the-channel model. In this work, a through-the-channel model is used; therefore, the gas channels are not included in the computational domain. The red

rectangle in the two-dimensional schematic in Figure 1.2 represents the computational domain used in this thesis. Given that the gas channels are not included in the model used in this thesis, a literature review of this component of the cell is unnecessary.

### Gas diffusion layer

The gas channels are in direct contact with the gas diffusion layers (GDLs). Diffusion layers are made of highly porous materials such as carbon paper or carbon cloth to allow easy transport of gases. They have a thickness in the range of  $100 - 300\mu m$ . These layers are responsible for

- transporting the fuel and reactant from the gas channels to the catalyst or reaction site.
- transporting product water (vapor or liquid) and heat away from the catalyst layer.
- transporting electrons from the catalyst site to the bipolar plates or vice versa.
- providing structural support to the membrane electrode assembly (MEA).

The gas diffusion layer transports electrons through the solid phase, i.e. carbon fibres. Ohm's law is used to model electron transport. Almost all models use Bruggemann's equation to account for the porosity of the media in determining electron conductivity [15, 16]. Recently, the anisotropic electronic transport in the GDL has received some attention and the necessity for new relationship between the GDL porosity and the GDL effective conductivities has been highlighted [17, 18].

Fuel, reactants, water vapor, and liquid water are all transported through the void phase of the gas diffusion layer. Gas and liquid phase transport are treated separately and some models neglect the water liquid phase by assuming that all water is in vapor state; these models are known as single-phase models. Models that account for gas

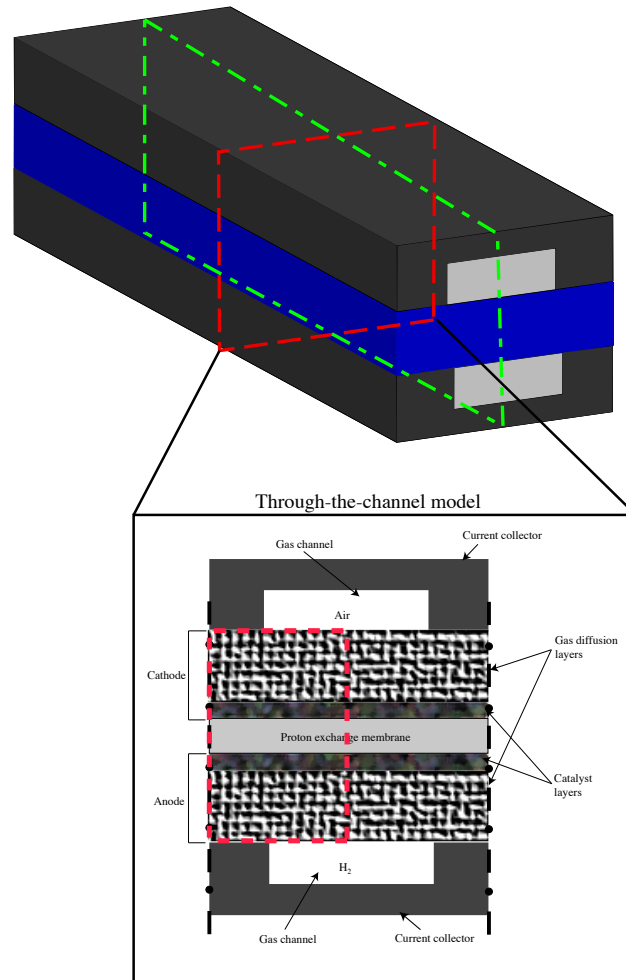


Figure 1.2: 3D schematic of a single channel PEMFC. Red rectangle shows the computational domain of a through-the-channel model. Green rectangle shows the computational domain of an along-the-channel model.

and liquid water are known as two-phase models. An introduction to two-phase flow in porous electrodes is given by Litster and Djilali [19].

In single-phase models, fuel, reactants and water vapor are assumed to be transported either by pure diffusion [16, 20–23] or by diffusion and pressure driven convection [24–26]. Pressure driven effects can be considered negligible for one-dimensional and two-dimensional through-the-channel models that consider only one flow channel. However, they can be important in two-dimensional along-the-channel models and are critical in three-dimensional simulations of fuel cells with interdigitated flow channels, since the pressures between channels can be quite different [27].

When fuel, reactants and water vapor are assumed to be transported only by pure diffusion, the Maxwell-Stefan equations are typically used to model the transport of the species. For binary mixtures, Fick’s law and the Maxwell-Stefan equations are equivalent. For mixtures with three species, under some simplifying assumptions, Fick’s law can also be used instead of the Maxwell-Stefan equations [20, 21, 23]. In addition to the Maxwell-Stefan diffusion, some models also take Knudsen diffusion into account [16, 28]. Knudsen diffusion becomes important when the mean-free path of the diffusing molecules is 10 times greater than the pore radius. This usually does not occur in the gas diffusion layer, but it might occur in the catalyst layer where pore sizes are smaller.

On the other hand, if fuel, reactants and water vapor are assumed to be transported by both diffusion and pressure driven convection, then the Maxwell-Stefan equations are used in conjunction with Darcy’s law to model convection in a porous media. Darcy’s law is usually introduced as the momentum equation in the set of governing equations [24–26].

In two-phase models, the liquid water is also accounted for in the GDL. There are a large variety of methods used to model the liquid water. The simplest method of modeling liquid water is to account for its effect by reducing the void fraction available

for gaseous transport in the GDL. Its transport is not modeled and its volume fraction is used as a fitting parameter. Then, its only effect is to reduce the ability of fuel and reactants to reach the reaction site [29,30]. A more sophisticated approach is to treat gases and liquid water as two different phases with an a priori gas and liquid volume fraction, using Darcy's law to model the liquid water transport [26,31,32].

Both these methods account for some of the effects of liquid water, however they do not take into account that the level of saturation can be different in different locations in the fuel cell, i.e. saturation levels are likely to be higher under the current collector. The saturation of the porous medium (i.e. the amount of pore volume fraction filled with liquid water) depends on the location where it is measured as well as in the medium properties such as the porous size, the hydrophobicity of the porous media and the capillarity pressure (i.e. the difference in pressure across the interface between the gaseous phase and the liquid water). For this reason, a method must be used to obtain the saturation as a function of the porous media and the capillarity pressure. In most models, the saturation is usually obtained by relating saturation to capillarity pressure using an empirical relationship such as the Leverett J-function. This relationship was obtained for one-dimensional steady-state transport on packed sand [19]. Gostick et al. showed good agreement between the Leverett J-function and experimental data from different GDLs [33]. Finally, the partial pressures of liquid water and water vapor are obtained by using Darcy's law for each phase [34,35].

### **Catalyst layer modeling**

The catalyst layers can be viewed as diffuse regions containing both electrolyte and electron conducting phases. These layers are porous. They are made of carbon black particles supporting platinum particles that are mixed together with an electrolyte, usually Nafion<sup>TM</sup>. The thickness of these layers is in the range of  $1 - 20\mu m$ . It is in the catalyst layers that the electrochemical reactions take place; therefore, these

layers are responsible for

- promoting reaction kinetics.
- transporting fuel and reactants.
- transporting electrons and protons.
- transporting water to the GDL or membrane.

Due to the complexity of modeling the catalyst layer, several models have emerged in the literature in the past decade. These models can be subdivided into three main categories: interface models, pseudo-homogeneous models and agglomerate models [11]. The main difference between these three types of models is in the assumed oxygen transport mechanism. While, there is relative agreement regarding the usage of Ohm's law to model electron and proton transport, and on the usage of the Butler-Volmer equation to model the reaction kinetics, such agreement does not exist regarding the modeling of oxygen transport.

Interface models, also called zero-thickness models, are commonly used when the primary interest is in modeling of multidimensional effects of a complete cell, or when studying water or heat management and the effects of catalyst layer composition are not of primary interest [26, 36]. In this model, the catalyst layer is assumed to be infinitely thin, and its composition and structure can be ignored by assuming that all properties are uniform throughout this layer. The catalyst layer is then regarded as an interface between the membrane and the gas diffusion layer. A single equation for the reaction kinetics is used to model the effect of the catalyst layer in the overall cell performance. The equation is introduced in the cell model as a boundary condition between the GDL and the membrane. This model is adequate when other effects are significantly more important than the catalyst layer effects. However, this approach does not resolve the cathode overpotential adequately [15, 37], and clearly it is not suitable for catalyst layer optimization.

Pseudo-homogeneous film models are an improvement over interface models. In a pseudo-homogeneous film model, the catalyst layer is assumed to be a porous random structure made of: a solid conductive material (usually carbon); the catalyst (usually platinum), and; an electrolyte (usually Nafion<sup>TM</sup>). The reaction occurs on the surface of the catalytic particles supported on the solid conductive material; therefore, protons, electrons and oxygen must travel through the catalyst layer to reach this reaction site. In the cathode catalyst layer, electrons are transported through the solid conductive material, protons are transported through the electrolyte and oxygen is transported through the void space. Oxygen is assumed to be transported in two different ways. Some researchers assume that oxygen is transported by diffusion through the liquid water that floods the void spaces [31, 32, 38]. Other researchers assume that oxygen is transported by diffusion as a gas, in gas pores that exist in the void space [16, 21, 39–41]. Each assumption results in a dramatic change in the resistance of the catalyst layer to oxygen transport. If the first assumption is used, oxygen is mostly consumed at the interface between the GDL and the catalyst layer; however, if the second assumption is used, the oxygen is consumed more uniformly in the catalyst layer. Regardless of the differences, both assumptions yield a model that takes into account some of the most important effects occurring at the catalyst layer. Both assumptions also consider the composition of the catalyst layer by relating catalyst layer properties to the volume fraction of each material. Therefore, either of these methods can be used for the optimization of the catalyst layer, even though they will result in very different optimal catalyst layer structures.

Pseudo-homogeneous film models assume that void space, the solid conductive material and the electrolyte are uniformly distributed in the catalyst layer. Recent studies in catalyst layer composition suggest that the conductive carbon support and platinum particles group in small agglomerates bounded by electrolyte [24, 42–45]. The agglomerates are assumed to be either spheres of electrolyte -usually Nafion<sup>TM</sup>- filled with carbon and Pt particles and approximately of one micron in

radius [15, 24, 42–44, 46] or spheres of carbon particles and platinum of around 50nm in radius that are void and are filled with liquid water during cell operation [47, 48]. In this thesis, electrolyte filled agglomerates are used. When the cathode transfer coefficient is one, the results for either type of agglomerates are similar if the size of the agglomerates are the same [48]. The optimal catalyst layer structure obtained using each type of agglomerate however can be quite different. This is because in electrolyte filled agglomerates, the electrolyte has two functions: to transport oxygen inside the agglomerate, and to transport protons in the CL. In water filled agglomerates, the electrolyte is only responsible for proton transport and transport of oxygen inside the agglomerate is achieved by means of the liquid water filling the agglomerates. As a result, if a water filled agglomerate model is used, it is expected that a lower optimal electrolyte content is obtained. According to both agglomerate models, the reaction inside the agglomerate can be modeled in a similar fashion to the reaction in a porous catalyst [49]. These models assume that oxygen diffuses through the gas pores, dissolves into the electrolyte/water around the agglomerate, diffuses through the electrolyte/water into the agglomerate and thereby reaches the reaction site. The transport process described is similar to the one suggested in pseudo-homogeneous film models; however, pseudo-homogeneous film models do not take into account the characteristics of the agglomerate or the diffusion of oxygen into the agglomerate. Therefore, the pseudo-homogeneous models are less likely to be accurate. Models that take into account the agglomerate structure are known as agglomerate models [15, 24, 50, 51]. Several studies have shown that agglomerate models give a better prediction of experimental results [42, 52]. However, agglomerate models require more empirically determined parameters, and this could be a reason for the better fit to experimental data [52].

### Polymer electrolyte membrane

The membrane is made of a solid material that acts simultaneously as a proton conductor, an electric insulator, and a barrier preventing fuel and reactant crossover between anode and cathode. The most commonly used type of membrane material is Nafion<sup>TM</sup>, a member of the perfluorosulfuric acid (PFSA) family of polymer membranes. The membrane is responsible for

- providing a path for the positive charges (ions) to travel from one reaction to the other.
- separating the oxidation and reduction reactions.

The importance given to membrane modeling is due mainly to the need for accurate predictions of the ohmic losses associated with protonic current. These losses depend on the degree of membrane conductivity, which is in turn a function of water content. As water content in the membrane is reduced, the protonic conductivity of the membrane drops, thereby increasing ohmic losses. This conflicts with the necessity to remove water from the GDL and catalyst layer in order to avoid flooding and to achieve better fuel and reactant transport. These conflicting goals are known as the water management problem.

In order to model the polymer electrolyte membrane, most models take into account that the membrane transports two components: protons, and liquid or sorbed water. This means that most models assume that fuel and oxygen cannot penetrate the membrane. Exceptions are those models that take into account fuel or oxygen cross-over. Cross-over is almost negligible for hydrogen fed PEM fuel cells. Cross-over effects can also readily be added to any membrane model [53]; therefore, they will not be further considered.

In most models, proton transport in the membrane is modeled either by Ohm's law or by the Nernst-Planck equation where the transport parameters, such as the

conductivity of the electrolyte, are dependent on the water content ( $\lambda$ , i.e. moles of water per mole of sulfonic acid sites). In the simplest models, water transport is neglected and the membrane is assumed to be fully hydrated, thereby enabling the protonic conductivity inherent to the fully hydrated electrolyte.

An accurate model of the membrane should take into account water transport as well as proton transport. There are two different approaches to modeling water transport: diffusion models [54] and hydraulic models [31, 32]. Diffusion models assume the membrane to be a homogeneous, nonporous matrix into which the dissolved water molecules move only by diffusion and electro-osmotic drag. Hydraulic models assume that the membrane system has two phases: the polymer phase and the liquid water filled pores. In this model, it is assumed that the water is driven by a pressure gradient and also by electro-osmotic drag. The liquid water velocity is obtained using Schlogl's equation. A membrane with a low water content is expected to obey a diffusion model. Conversely, when the membrane is saturated, the hydraulic model provides a better approximation of the water transport [55, 56]. Therefore, the most accurate model would be one that incorporates both assumptions regarding the membrane. Such model was described in references [53, 55]. Finally, recently a more rational framework that couples protonic and water transport has also been proposed [57].

### **Heat management**

A fuel cell operation involves the generation and transport of heat; therefore, these effects should, in principle, also be taken into account during the modeling. The fuel cell reactions generate heat, mainly due to irreversibilities. Furthermore, water condensation and evaporation are also important sources and sinks of heat. In order to include heat generation and transport in the model, the energy conservation equation has to be introduced to the model in order to obtain the temperature distribution inside the cell [25, 28, 34, 36].

Non-isothermal studies such as reference [34] show that temperature variations are relatively small in the cell sandwich (the across-the-channel section), i.e. around one degree. Therefore, the isothermal assumption is reasonable for single-phase one-dimensional and across-the-channel two-dimensional models. Thermal effects become more important for two-phase models and for complete cells and fuel cell stacks and, in such cases, they should be modeled.

### 1.2.2 Numerical optimization

Advances in digital computer technology have spurred spectacular progress in the area of numerical methods for optimization. Active research has produced an abundance of methods for unconstrained and constrained optimization [58–60].

Engineering applications for optimization usually involve solving a nonlinear constrained optimization problem. Nonlinear constrained optimization problems involve the search for a minimum of a nonlinear objective function subject to a set of nonlinear constraints, and it is common for this optimization problem to have multiple extrema. Due to this difficulty, two different approaches have emerged in the area of nonlinear constraint optimization: local methods and global methods. Local methods aim to obtain a local minimum, and they cannot guarantee that the minimum obtained is the absolute one. These methods are usually first-order methods, i.e. they require information about the gradient of the objective function and the constraints. On the other hand, global methods aim to obtain the absolute or global minimum of the function. They do not require any information about the gradient, and they are based primarily on stochastic procedures.

Local constrained methods can be classified into sequential methods and transformation-based methods. Sequential methods aim to solve the nonlinear constrained problem by iteratively solving a simpler constrained optimization problem. The most commonly used local sequential methods include the method of feasible directions (MFD)

and the modified method of feasible directions (MMFD) [5, 58, 61]; sequential linear programming (SLP) [5, 58, 62]; sequential quadratic programming (SQP) [59, 63]; non-linear interior point methods [59, 64], and; response surface approximation methods (RSM) [65, 66].

The MMFD is based on obtaining a sequence of feasible directions, i.e. directions that reduce the objective function and satisfy the constraints. Then, the design is moved in these directions until convergence to the optimum is achieved. The main drawback of this method is that it performs poorly if the constraints are highly non-linear or discontinuous. The SLP method solves iteratively a linear programming subproblem obtained by linearizing the objective function and the constraints. Because linear approximations are only valid in the neighborhood of the linearization point, the norm of the search vector used to improve the design needs to be constrained. This constraint is achieved by imposing limits to the maximum allowable change of the design variables. These limits are known as move limits. The main drawback of SLP methods is the choice of the move limits. If the move limits are large, the method leads to oscillations in the convergence and the algorithm may not converge. On the other hand, if the move limits are too small, the SLP presents a low convergence rate. The main advantages of SLP methods are: they are simple to implement because they only involve the solution of a linear programming problem (LP) and, they are proved to yield good results if the move limits are properly adjusted [67]. Similarly, SQP methods are based on a second-order approximation of the objective function and a linearization of the constraints [58] or on a second-order approximation of the Lagrangian of the original problem [59]. SQP methods are robust, have a fast convergence rate and are the most frequently used local non-linear constrained optimization method. Interior point methods are based on using Newton's method in conjunction with a modified objective function that includes the optimization constraints as penalties to the objective function. The penalty is introduced by means of a merit function, the value of which is adaptively increased

in order to provide joint progress towards the minimization of the original objective function and the feasible region. Interior point algorithms have been developed to solve linear, quadratic and nonlinear problems. The modified optimization problem is solved by solving the equations resulting from the Karush-Kuhn-Tucker optimality conditions using Newton's method. As a result, this method requires information on the gradients and the Hessian of the objective function and constraints. In most cases, the Hessian is approximated using the BFGS approximation. Interior point methods are considered the most efficient optimization algorithms for solving both linear and nonlinear large-scale optimization problems [59, 64]. The quasi-Newton interior-point method used in this thesis belongs to this family of optimization algorithms [68, 69]. Finally, response surface approximation methods use interpolation models to model the objective function and constraints of the original problem. The interpolation model, usually a quadratic model, is then used to optimize the problem. The problem is solved iteratively and the approximation model is updated with the last solution.

Local transformation-based methods transform the original nonlinear optimization problem into an unconstrained optimization problem by adding a penalty function to the objective function. When the constraints are not satisfied, the penalty function increases its value thereby increasing the value of the objective function. Once the constrained problem has been transformed into an unconstrained problem, any unconstrained optimization algorithm can be used to solve the transformed problem. For example, a Quasi-Newton method or a conjugate-gradient method can be used [5, 58, 59, 61]. The most commonly used local transformation-based methods are: penalty methods [5, 58] and augmented Lagrangian methods [5, 58, 61]. The former eliminates the constraints by adding a penalty function to the objective function. The penalty function increases the value of the objective function when the constraints are violated. The main drawback to these methods is that the penalty functions are dependent on the problem at hand and are therefore difficult to generalize. On the

other hand, Lagrangian methods solve the optimization problem by introducing a set of Lagrange multipliers that control the penalty function and make the Lagrange multipliers variables in the optimization program. All penalty methods share a common drawback: due to the introduced penalty, the objective function becomes highly nonlinear, making it difficult for the unconstrained methods to obtain the minimum.

To conclude this description of local constrained methods, it is important to note that, although local methods do not aim for the global optima, they can be used to obtain such global optima. Several approaches can be used to continue searching once a local minimum has been obtained, thereby enabling the identification of all local minima and, therefore, also the global minimum. Some of these methods based on a stochastic approach are: random multi-start methods [70, 71] and ant colony searches [72]. In the former method, once a minimum has been obtained, it restarts the optimizer with a new, randomly generated initial point. The second method uses the information from search agents (ants) in order to find the global minimum. Some other methods introduce a deterministic approach. For example, in the local-minimum penalty method [73] the objective function is penalized if the algorithm tends to go to an already known local minima.

The other group of constrained methods, the global methods, can be classified as direct or transformation-based. Direct methods solve the problem without transforming it into a simple problem. Transformation-based methods transform the initial constrained optimization problem into an unconstrained problem. Direct methods include covering methods and pure random searches. Covering methods follow a deterministic approach where regions of the design space are tested and eliminated if specific design criteria are not met. The most common of these methods are the interval methods [74]. Pure random searches evaluate randomly generated points until a minimum is obtained. The main drawback of both these methods is that they require a large number of function evaluations and are therefore computationally expensive.

Global transformation-based methods start by transforming the original problem

into an unconstrained problem. Then, global unconstrained techniques are used to obtain the global minima. Popular unconstrained global methods are: genetic algorithms [75], evolutionary algorithms [76] and simulated annealing [77]. These methods have the same drawback as the global direct methods: the computational cost of the large number of evaluations of the objective function and constraints is excessive.

### 1.2.3 Sensitivity analysis

Sensitivity analysis is concerned with obtaining the gradients or sensitivities of a certain output variable with respect to an input variable. In the case of optimization, sensitivity analysis is used to obtain the derivatives of objective function and constraints with respect to the design variables.

In the literature, several methods have been suggested to compute the gradients of physical properties with respect to the design variables

- Finite-Difference
- Complex-Step Differentiation
- Automatic Differentiation
- Analytical Differentiation

Forward-difference uses a Taylor series expansion of a function around a point,  $\mathbf{x}_0$ , to obtain an approximation of the gradient. Forward-difference needs  $n + 1$  function evaluations to compute the gradient of a function, with  $n$  being the number of independent variables. First-order forward difference is easy to implement and is computationally more efficient than complex-step differentiation and automatic differentiation methods [78, 79]. However, forward-difference is also the most inaccurate of all the methods described above. This is because the error is proportional to the step size. Therefore, to reduce the error, the step size must be reduced. However, if

the step size becomes too small, the two terms that are subtracted on the numerator become very similar and a numerical error occurs when computing their difference. Therefore, it is necessary to obtain a step size small enough to reduce the error, but not so small that subtractive errors occur. This is known as the *step size dilemma*. This problem is also encountered in higher order methods that use the Taylor series to approximate the gradients, e.g. the central-difference method [78, 79]. Furthermore, for higher order methods more function evaluations are necessary to compute the gradients.

Complex-differentiation solves the step size dilemma encountered in the finite-difference method by using a complex step to compute the gradients [78, 80, 81]. Furthermore, the approximation is second order instead of first order as it is in forward-differentiation. The number of function evaluations necessary to obtain the gradient is still  $n + 1$  where  $n$  is the number of independent variables of the function. In order to obtain the gradients using complex-step differentiation, the source code of the analysis program has to be changed so that all the real variables become complex variables. Some intrinsic functions such as *max* and *min* must also be redefined. If the designer is adept at modifying the source code of the analysis solver, the required changes to the code can be accomplished in a relatively short amount of time. It is important to note that, because all the variables are complex instead of real, the complexified code requires twice as much time as of the original code required to solve the same problem .

Automatic differentiation (AD) - also known as algorithmic differentiation or computational differentiation - is based on successive application of the chain rule to each operation performed in the analysis computer code [82, 83]. Since the structure of a computer code is basically composed of a successive set of arithmetic operations used to compute the value of a function, successive application of the chain rule to each one of the operations in the code will result in the exact (to machine precision) desired derivatives. In order to transform a code into a forward or reverse automatic

differentiation code, there are several programs that, given a list of the dependent and independent variables, precompile the original code and transform it into an AD code. Some of the codes that can be used to transform FORTRAN source codes to AD codes are: ADIFOR, TAMC, DAFOR, GRESS, Odysee, PADRE2, AD01, ADOL-F, IMAS, Tapenade and OPTIMA90.

Finally, analytical differentiation consists of deriving the analytical expressions for the sensitivities and introducing them to the original analysis code. These methods are the most efficient and accurate, however, they are also the most difficult and time consuming to implement because they require a complete knowledge of the original analysis code and the physics of the problem. There are basically two methods used to compute the sensitivities analytically: direct methods and adjoint methods.

Using the direct method to obtain the sensitivities of a function with respect to  $n$  independent variables is computationally equivalent to solving  $n$  times a linear system of equations of the size of the original analysis problem. Therefore, the computational expense is similar to finite-differences in forward mode for a linear problem, but much less costly than forward-differences for nonlinear problems. This is because to solve a nonlinear problem, the original system needs to be solved several times before reaching the solution while the systems of equations to obtain the sensitivities are only solved once. Once the gradient of the unknowns of the model are obtained, they can be used to obtain the gradient of any function with respect to the design variables. Using this method, the computations necessary to obtain the gradients of  $m$  function with respect to  $n$  design variables is the solution of  $n$  linear systems of equations of the size of the original program.

In most cases in design, there are more independent variables, i.e. design variables in the optimization problem, than functions for which the gradients are necessary. To eliminate the dependence of the gradient computations on the number of independent variables, the adjoint method was created. Introduced in the CFD community by Jameson [84], the adjoint method differs from the direct method in that the com-

putations for obtaining the gradient of a function do not depend on the number of independent variables. Therefore, the cost of computing the gradient of  $f$  is similar to the computational time necessary to obtain the solution to the problem, and it is independent of the number of independent variables. This is the key to this method's recent success in areas such as structural and aerodynamic shape optimization.

### 1.2.4 Numerical optimization of PEM fuel cells

A literature review in the area of fuel cell design and optimization shows that most of the work done in fuel cell design is based on parametric studies and graphically aided design. To this author's knowledge, only four research groups - Song et al. [20, 29], Grujicic et al. [85–87], Mawardi et al. [88] and Secanell et al. [89–92] - have attempted to perform single cell fuel cell optimization using a physical or theoretical model.

Song et al. [20, 29] optimized the catalyst layer composition of a PEM fuel cell in order to achieve maximum current density at a specified voltage of 0.6V. They used a one-dimensional pseudo-homogeneous catalyst layer model to analyze the cathode catalyst layer. The design variables that they used are the Nafion volume fraction, the platinum loading and, in paper [20], the thickness of the catalyst layer. The optimization problem is solved with respect to only one or two of these design variables, therefore it does not take full advantage of the numerical optimization capabilities.

On the other hand, Grujicic et al. [85–87] concentrated their efforts on the optimization of the geometric parameters of the fuel cell cathode without taking into account the catalyst layer composition. In particular, in reference [85] the authors used a two-dimensional single-phase model of the fuel cell to optimize the output current density at a given cell voltage (0.7V). The design variables were the inlet cathode pressure, the cathode GDL thickness and length of the current collector and gas channel. The model used to perform the optimization used Fick's law and Darcy's law to account for transport of fuel and reactants and Ohm's law for the transport

of electrons through the GDL. A zero-thickness model is used to account for the active catalyst layer reactions and Ohm's law is used to account for proton transport through the membrane. In reference [86] the same optimization problem is solved but with respect to only the cathode GDL thickness and length of the current collector and gas channel. However, the model is expanded to take into account two-phase flow. In reference [87] the same optimization problem as in [86] is solved. The fuel cell model used is single-phase, but it has been expanded to three dimensions, the Maxwell-Stefan equations are used to model diffusion and the transport of the fuel and reactants through the gas channels are also modeled. In all papers by Grujicic et al. [85–87], the catalyst layer is modeled using a simple zero-thickness model. This is done at the expense of accuracy since the resolution of the catalyst layer has a critical impact on the performance predictions and detailed distributions of current and potentials. The omission of the catalyst layer is necessary in these cases in order to reduce the computational expense of the numerical model, because a very fine grid is necessary in order to properly resolve the active layer.

In Song et al. [20,29] and Grujicic et al. [85–87] gradient-based methods are used, in particular both groups use the sequential quadratic algorithm in MATLAB [93], in order to reduce the computational expense incurred by performing optimization. However, they both use numerical differentiation in order to obtain the gradient of the objective function and its constraints. Numerical differentiation is inaccurate and requires one additional problem solution for each design variable in order to obtain the gradients. Therefore, this method tends to destabilize the optimization algorithm due to numerical errors, and it becomes prohibitively expensive when the number of design variables is large. A more sophisticated optimization framework that takes advantage of new advances in sensitivity analysis and in multiprocessor architecture would alleviate the computational demands incurred during optimization, and would allow researchers to use higher fidelity models to perform optimization of fuel cells with a large number of design variables.

Mawardi et al. [88] used a one-dimensional, non-isothermal model to model the complete fuel cell sandwich. In this case, the objective function was the maximum power density at a given current density and the design variables were nine operating parameters. In particular, the operating parameters were temperature, anode and cathode pressure, stoichiometry and relative humidity, nitrogen to oxygen mole fraction and carbon dioxide to hydrogen mole fraction. Instead of using a gradient-based optimization algorithm, the Nelder-Mead simplex method combined with a simulated annealing algorithm was used. These algorithms are non-gradient based methods and, therefore, the gradients are not necessary. In the paper, the number of calls to the analysis code and the computational time necessary to reach the solution are not discussed. In general and as discussed in section 1.2.2, non-gradient based methods require a large number of calls to the fuel cell model. Therefore, the methodology used in this paper does not allow for the feasible usage of high-fidelity fuel cell models because each fuel cell model call can take hours. When the analysis program requires a large amount of computation time, gradient-based optimization algorithms are a better choice since they can reduce the number of fuel cell model evaluations and therefore, the computational time necessary to reach the optimal solution.

Finally, Secanell et al. used a one-dimensional [89] and two-dimensional through-the-channel model [90–92] to maximize the cell current density at a given operating voltage with respect to either anode or cathode GDL and CL composition. To solve the optimization problem, a gradient-based interior point optimization algorithm was used in conjunction with analytical sensitivities (direct method). Since the problem is nonlinear, using the direct method to obtain the analytical sensitivities resulted in large computational savings and a good convergence to the optimal solution. Due to the low computational requirements of this method, an electrode model with a state-of-the-art catalyst layer model was used to predict fuel cell performance.

## 1.3 Contributions

The main contributions of this work are in the areas of fuel cell diagnostics and design. In the area of fuel cell diagnostics, this work contributes to the field by

- developing a two-dimensional through-the-channel fuel cell model with state-of-the-art catalyst layer models for both anode and cathode.
- introducing a new set of equations to relate the catalyst ink composition to effective catalyst layer parameters.
- presenting an OpenSource software for fuel cell design based on adaptive finite elements and developed using an object-oriented programming language.

In the area of fuel cell design, this work represents one of the first attempts at trying to apply numerical optimization to fuel cell design. As such, it presents for the first time in the literature

- a fuel cell simulation toolbox that provides analytical sensitivities of the current density with respect to design variables.
- a numerical study of the optimal composition of a complete MEA using a detailed two-dimensional model.
- a numerical study of the trade-offs between cost and performance in MEA design by means of a multi-objective optimization formulation.

The development of a framework to obtain analytical sensitivities with respect to design parameters is, in the author's opinion, the key to applying numerical optimization to large-scale fuel cell optimization problems in a reasonable time frame.

## 1.4 Structure of the thesis

This thesis is organized into four chapters. The first chapter presents the motivation for this work and a literature review of past and present research efforts in: fuel cell modeling and optimization; numerical optimization, and; sensitivity analysis. Chapter 2 presents the fuel cell analysis part of this thesis. In this chapter, the governing equations for the anode and cathode electrodes and the membrane are presented as well as their couplings. Then, the computational model is validated against a recent experimental study and other numerical results. The transport mechanisms of the MEA design from the validation study are studied in detail. Chapter 3 presents the optimization analysis and results. Two optimization formulations for fuel cell design are suggested and an optimization framework is presented to solve these two problems. Starting with the design from the previous section as base design, the two optimization problems are solved and the results from the optimization are analyzed. Finally, Chapter 4 presents some final conclusions and possible avenues for future research.

## Chapter 2

# PEM fuel cell modeling

In this chapter, the equations implemented in the fuel cell modeling framework known as Fuel Cell Simulation Toolbox (FCST), developed by the author, are described. The numerical methodology used to solve these equations is also described. Numerical results obtained from the modeling framework are presented together with parametric studies that highlight the main differences between the implemented models. The chapter is divided into five sections. The first four sections describe the models used to analyze: the cathode electrode, the proton exchange membrane, the anode electrode and the complete membrane electrode assembly respectively. The fifth section presents some validation results, and also a study of the transport processes occurring in the MEA for the base design at different operating conditions.

## 2.1 Cathode electrode modeling

### 2.1.1 Governing equations

In a proton exchange membrane fuel cell the oxygen reduction reaction occurs in the cathode



The electrochemical reaction is usually described either by a Tafel or a Butler-Volmer equation. To describe the transport of the different species to the reaction site two models are presented: the pseudo-homogeneous model, also known as macro-homogeneous, and the agglomerate model. Both models take into account the physical structure of the cathode electrode to model the transport of species.

#### Governing equations for the pseudo-homogeneous model

In the pseudo-homogeneous models, the catalyst layer is taken to be a porous structure consisting of a catalyst (usually platinum) supported on a solid conductive material (usually carbon) and an electrolyte (usually Nafion<sup>TM</sup>). The reaction occurs on the surface of the catalytic particles supported on the solid conductive material, and therefore, ions, electrons and oxygen must travel through the catalyst layer to reach the reaction sites. In the cathode catalyst layer, electrons are transported through the solid conductive material, ions through the electrolyte, and oxygen through the void spaces. Two approaches are commonly used to represent oxygen transport. In the first approach, the void spaces are assumed to be flooded with water, and oxygen is assumed to be transported in the dissolved state by diffusion [20, 31, 32, 38]. In the second approach, oxygen is present in the gas phase within wet-proofed pores in the catalyst layer, and transport is considered to take place by gas phase diffusion [16, 21, 39–41]. These two approaches result in drastically different levels of resistance

to oxygen transport thereby resulting in very different results. In the former case, oxygen is consumed primarily at the interface between the GDL and the catalyst layer; in the case of gas phase diffusion, oxygen is distributed more homogeneously throughout the catalyst layer. In reality, both gas and liquid water coexist in the catalyst layer and two-phase models are necessary. In this thesis, a one-phase model is used that assumes that oxygen is transported in the gas phase in the wet-proofed pores in the catalyst layer and that once it reaches the catalyst site, it dissolves into the electrolyte/water before reaching the reaction site. This last step introduces an extra transport limitation similar to the dissolution in water.

Following the discussion above, the model is based on the following assumptions [90]:

- The fuel cell operates at steady state.
- It is at a constant temperature and pressure.
- The gas diffusion layer (GDL) is composed of void space and carbon fibers.
- The catalyst layer (CL) is formed of a mixture of platinum supported on carbon, ionomer membrane electrolyte (Nafion<sup>TM</sup>) and void space [29, 39].
- The transport of reactants from the gas channels to the CL occurs only by diffusion of oxygen gas in wet-proofed pores and can be modeled by Fick's first law [36].
- Once the oxygen arrives at the catalyst site, it has to dissolve into an infinitesimally thin layer of ionomer which covers the catalytic sites. This layer is therefore assumed to be infinitesimal, and this process is modeled using Henry's law.
- The transport of protons takes place only through the electrolyte, usually the Nafion<sup>TM</sup>, and it is governed by Ohm's law.

- The transport of electrons takes place only through the solid phase, i.e. the carbon fibers in the GDL and platinum and carbon in the catalyst layer, and it is governed by Ohm's law.

The reactant transport to the reaction site must obey the law of conservation of species. For an infinitesimal control volume, the conservation of species  $i$  can be written as

$$\frac{dc_i}{dt} + \nabla \cdot \mathbf{N}_i = S_i \quad (2.2)$$

where  $c_i$  is the molar concentration of species  $i$ ,  $\mathbf{N}_i$  is the molar flux of species  $i$  and  $S_i$  is the rate of production/consumption of species  $i$ . In this case, it is assumed that the fuel cell is operating at steady state, therefore equation (2.2) reduces to

$$\nabla \cdot \mathbf{N}_i = S_i \quad (2.3)$$

Oxygen and water transport in the cathode electrode are then governed by equations

$$\nabla \cdot \mathbf{N}_{O_2} = S_{O_2} \quad (2.4)$$

$$\nabla \cdot \mathbf{N}_{H_2O} = S_{H_2O} \quad (2.5)$$

where  $S_{O_2}$  represents the consumption of oxygen and  $S_{H_2O}$  the production of water in the reaction given by equation (2.1). From the reaction kinetics a relation between the rate of production/consumption of the different species in the reaction can be obtained such that

$$S = -S_{O_2} = -\frac{1}{4}S_{H^+} = -\frac{1}{4}S_{e^-} = \frac{1}{2}S_{H_2O} \quad (2.6)$$

where  $S_{H^+}$  and  $S_{e^-}$  represent the consumption of protons and electrons respectively. Given these last relations, a relationship between the oxygen flux, proton flux and the electron current density can be obtained. In order to obtain such relationship, let

us begin by defining the current density as [94]

$$\mathbf{i} = \sum_i z_i F \mathbf{N}_i \quad (2.7)$$

where  $z_i$  and  $\mathbf{N}_i$  are the charge and molar flux of the species and  $F$  is Faraday's constant (96,487C/mol). Using this definition, the current density in the electrolyte phase is related to the protonic flux by

$$\mathbf{i}_p = F \mathbf{N}_{H^+} \quad (2.8)$$

since it is the only charged mobile species. In the solid phase, the current density is related to the electronic flux by

$$\mathbf{i}_e = -F \mathbf{N}_{e^-} \quad (2.9)$$

Using the equations above and equation (2.6) relationships between the consumption/production of electrons and protons and their current densities are obtained

$$S = -\frac{1}{4} S_{H^+} = -\frac{1}{4F} \nabla \cdot \mathbf{i}_p \quad (2.10)$$

and

$$S = -\frac{1}{4} S_{e^-} = \frac{1}{4F} \nabla \cdot \mathbf{i}_e \quad (2.11)$$

Because the last two equations are equal, a relationship can be obtained between the current density in the electrolyte membrane and the solid phase,

$$\nabla \cdot \mathbf{i}_p = -\nabla \cdot \mathbf{i}_e \quad (2.12)$$

Substituting equations (2.6) and (2.10) into the conservation law for the oxygen species, equation (2.4), and using equation (2.12) a relationship is also obtained

between the oxygen molar flux and the electronic and proton current densities

$$\nabla \cdot \mathbf{N}_{O_2} = \frac{1}{4F} \nabla \cdot \mathbf{i}_p = -\frac{1}{4F} \nabla \cdot \mathbf{i}_e \quad (2.13)$$

Using an analogous procedure, the relationship between the water flux and the current density is

$$\nabla \cdot \mathbf{N}_{H_2O} = -\frac{1}{2F} \nabla \cdot \mathbf{i}_p = \frac{1}{2F} \nabla \cdot \mathbf{i}_e \quad (2.14)$$

It is assumed that the domain of the model is isobaric and isothermal, and that the species are transported only by diffusion. Then, oxygen, nitrogen and water vapor transport is modeled by the Maxwell-Stefan equations [95],

$$\sum_{j=1}^N \frac{x_j \mathbf{N}_i - x_i \mathbf{N}_j}{D_{ij}^{eff}} = c \nabla x_i \quad (2.15)$$

which substituting indices becomes a system of three equations

$$\frac{x_{O_2} \mathbf{N}_{N_2} - x_{N_2} \mathbf{N}_{O_2}}{D_{O_2 N_2}^{eff}} + \frac{x_w \mathbf{N}_{N_2} - x_{N_2} \mathbf{N}_w}{D_{w N_2}^{eff}} = -c \nabla x_{N_2} \quad (2.16)$$

$$\frac{x_{N_2} \mathbf{N}_{O_2} - x_{O_2} \mathbf{N}_{N_2}}{D_{O_2 N_2}^{eff}} + \frac{x_w \mathbf{N}_{O_2} - x_{O_2} \mathbf{N}_w}{D_{O_2 w}^{eff}} = -c \nabla x_{O_2} \quad (2.17)$$

$$\frac{x_{N_2} \mathbf{N}_w - x_w \mathbf{N}_{N_2}}{D_{w N_2}^{eff}} + \frac{x_{O_2} \mathbf{N}_w - x_w \mathbf{N}_{O_2}}{D_{O_2 w}^{eff}} = -c \nabla x_w \quad (2.18)$$

where the mole fractions must satisfy that

$$\sum_i x_i = 1 \quad (2.19)$$

or, in this case, assuming that dry air is mainly composed of nitrogen and oxygen and considering the mole fraction of the other species in the air negligible,

$$x_w + x_{N_2} + x_{O_2} = 1 \quad (2.20)$$

where  $x_w$  accounts for the air humidification.

Assuming that both oxygen and water vapour are dilute species in nitrogen and

$$x_{N_2} \rightarrow 1 \quad x_{O_2} \rightarrow 0 \quad \text{and} \quad x_w \rightarrow 0 \quad (2.21)$$

and substituting into equations (2.17) and (2.18) turns the Maxwell-Stefan equations to Fick's first law of diffusion

$$\mathbf{N}_{O_2} = -c_g D_{O_2, N_2}^{eff} \nabla x_{O_2} \quad (2.22)$$

$$\mathbf{N}_w = -c_g D_{w, N_2}^{eff} \nabla x_w \quad (2.23)$$

Note that the assumption of dilute species is a reasonable one taking into account that the nitrogen molar fraction in air is 0.79 and that, for pure humidified oxygen, the system reduces to a binary system and therefore, it is also equivalent to Fick's first law.

Using equation (2.22) and equation (2.13) and defining  $D_{O_2, N_2}^{eff} = D_{O_2}^{eff}$  a relationship between the oxygen mole fraction and the current density is obtained

$$\nabla \cdot \mathbf{N}_{O_2} = \nabla \cdot (c_g D_{O_2}^{eff} \nabla x_{O_2}) = \frac{1}{4F} (\nabla \cdot \mathbf{i}_e) \quad (2.24)$$

This last equation will be used to obtain the oxygen concentration in the cathode electrode.

In addition to mass transport, in the fuel cell cathode there is also transport of protons and electrons. The transport of these two species is modeled using Ohm's law. In the electrolyte phase, the transport of protons is modeled by

$$\mathbf{i}_p = -\sigma_m^{eff} \nabla \phi_m \quad (2.25)$$

where  $\sigma_m^{eff}$  is the effective protonic conductivity of CL and depends on the electrolyte

water content, the CL composition and the physical properties of the CL components. This value will be zero in the gas diffusion layer since this layer does not contain Nafion<sup>TM</sup>.

The transport of electrons occurs in the solid phase where it is the only mobile charged specie. The transport of electrons is also governed by Ohm's law

$$\mathbf{i}_e = -\sigma_S^{eff} \nabla \phi_S \quad (2.26)$$

where in this case  $\sigma_S^{eff}$  is the effective conductivity in the solid phase and depends on the layer composition and physical properties. The methodology to obtain effective properties of the GDL and CL will be discussed in detail in the following sections.

Taking derivatives of equations (2.25) and (2.26) and using equation (2.12), the equations can be both written as a function of the electronic current density as

$$\nabla \cdot \mathbf{i}_e = \nabla \cdot (\sigma_m^{eff} \nabla \phi_m) \quad (2.27)$$

$$\nabla \cdot \mathbf{i}_e = -\nabla \cdot (\sigma_S^{eff} \nabla \phi_S) \quad (2.28)$$

The transport of mass and charges in the gas diffusion and catalyst layers is thus governed by the following set of equations

$$\left. \begin{aligned} \nabla \cdot (c_g D_{O_2}^{eff} \nabla x_{O_2}) &= S_{O_2} \\ \nabla \cdot (\sigma_m^{eff} \nabla \phi_m) &= S_{H^+} \\ \nabla \cdot (\sigma_S^{eff} \nabla \phi_S) &= S_{e^-} \end{aligned} \right\} \quad (2.29)$$

where the effective parameters are different in the GDL and CL and the source term is

$$S_{O_2} = \begin{cases} 0 & \text{in GDL} \\ \frac{1}{4F} \nabla \cdot \mathbf{i} & \text{in CL} \end{cases} \quad (2.30)$$

$$S_{H^+} = \begin{cases} 0 & \text{in GDL} \\ \nabla \cdot \mathbf{i} & \text{in CL} \end{cases} \quad (2.31)$$

$$S_{e^-} = \begin{cases} 0 & \text{in GDL} \\ -\nabla \cdot \mathbf{i} & \text{in CL} \end{cases} \quad (2.32)$$

Finally, the term  $\nabla \cdot \mathbf{i}$ , the current produced per unit volume of catalyst layer, is given by the electrochemical reaction that occurs inside the layer. Given that the kinetics of the oxygen reduction reaction that takes place in the cathode are slow, the Butler-Volmer equation is not necessary and the reaction rate is given by the Tafel equation

$$\nabla \cdot \mathbf{i} = A_v i_0^{ref} \left( \frac{c_{O_2,gl}}{c_{O_2}^{ref}} \right)^\gamma \exp \left( \frac{\alpha_c F}{RT} (\phi_m - \phi_s) \right) \quad (2.33)$$

where  $A_v$  is the specific reaction surface area per volume of the catalyst layer,  $i_0^{ref}$  is the exchange current density,  $c_{O_2}^{ref}$  is the reference oxygen concentration,  $c_{O_2,gl}$  is the oxygen concentration at the reaction site,  $\alpha_c$  is the transfer coefficient of the reaction,  $T$  is the cell temperature,  $\phi_m$  and  $\phi_s$  are the electrolyte and solid potentials and  $\gamma$  is a reaction dependent constant,  $R$  and  $F$  are universal constants. The exchange current density, the reference oxygen concentration, the transfer coefficient and  $\gamma$  are electrochemical data and are obtained from experiments [96, 97].

Given the assumption that oxygen needs to dissolve into the electrolyte before reaching the reaction site, the oxygen concentration at the reaction site is given by Henry's law

$$c_{O_2,gl} = \frac{c_{O_2,g}}{\hat{H}_{O_2,N}} \quad (2.34)$$

where  $c_{O_2,g} = c_g x_{O_2}$  is the oxygen concentration in the wet-proofed pores in the CL and the dimensionless Henry's law constant is obtained using

$$\hat{H}_{O_2,N} = \frac{H_{O_2,N} 10^{-6}}{RT} \quad (2.35)$$

and  $H_{o_2,N}$  is  $3.1664 \times 10^{10} \frac{Pa \cdot cm^3}{mol}$  [15].

The specific reaction surface area per volume of the catalyst layer,  $A_v$ , is dependent on the platinum loading  $m_{Pt}$ , the thickness of the catalyst layer  $L$ , and the catalyst surface area per unit mass of the catalyst particle,  $A_0$ , [20, 38]

$$A_v = A_0 \frac{m_{Pt}}{L} \quad (2.36)$$

The catalyst surface area per unit mass of the catalyst particle,  $A_0$ , depends on the size of the platinum particles and on the platinum content of the catalytic particles in the catalyst layer. In this study, an empirical least squares fit to the data provided by E-TEK [98] is used to estimate this value

$$A_0 = 7.401 \times 10^6 (Pt|C)^4 - 1.811 \times 10^7 (Pt|C)^3 + 1.545 \times 10^7 (Pt|C)^2 - 6.453 \times 10^6 Pt|C + 2.054 \times 10^6 \quad (2.37)$$

Figure 2.1 shows the data from E-TEK and the curve fit of the catalyst surface area per unit mass of the catalyst particle at different platinum to carbon ratios. For comparison with previous papers that used data from an older generation of catalysts such as [38, 91], the data reported by Marr et al. [38] for older catalysts is also shown in the figure and a curve fit used in previous publications by the authors is also shown. From this plot, it can be observed that there has been a remarkable improvement in recent years in increasing the active area of platinum supported catalyst particles.

### Governing equations for the agglomerate model

The agglomerate model used in this thesis assumes that the conductive carbon support and platinum particles are grouped in small spherical agglomerates bonded and surrounded by electrolyte [15, 24, 24, 42, 43, 43–45, 50]. Water filled agglomerates [47, 48] are not considered. A representation of the cathode electrode according to the ag-

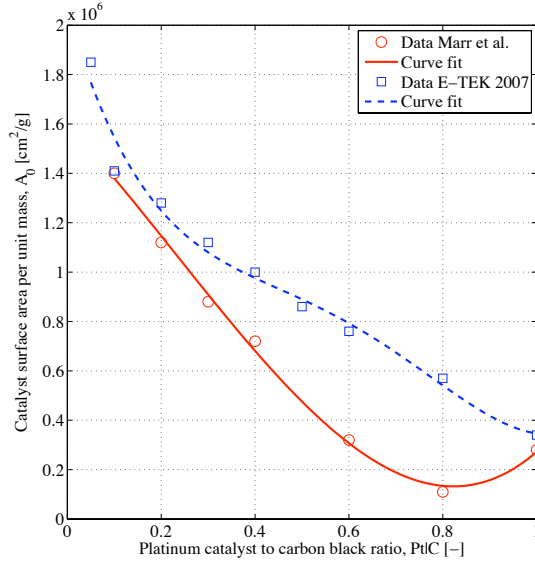


Figure 2.1: Curve fit used to estimate the catalyst active area per mass of catalyst

glomerate model adopted in this thesis can be seen in Figure 2.2. The reaction inside the agglomerate is then modeled as a reaction in a porous catalyst [49]. Oxygen is assumed to diffuse through the gas pores between agglomerates, dissolve into the electrolyte phase and, finally, to diffuse in the electrolyte inside the agglomerate through to the reaction site.

Even though pseudo-homogeneous and agglomerate models are both in use today, several studies have shown that agglomerate models provide a better fit to experimental results [42, 52]. A comprehensive comparative study of the three catalyst layer models was recently presented using three-dimensional numerical solutions [99]. This comparison highlighted the importance of a physically representative model for the catalyst layer, showing that, at low current densities, the thin film model results in different current density distributions compared to the pseudo-homogeneous and agglomerate models. Furthermore, only the agglomerate model was capable of predicting the performance drop at high currents due to the mass transport limitations

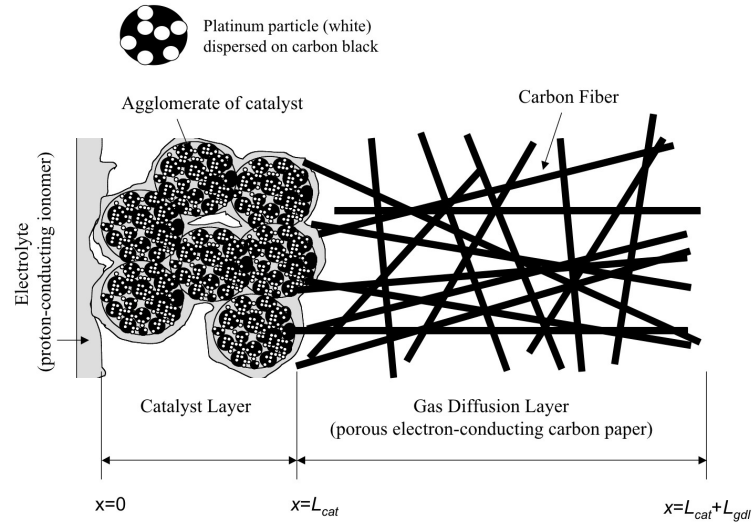


Figure 2.2: Catalyst layer and gas diffusion layer microstructure, [100]

that are observed in an actual fuel cell.

Following the discussion above, the agglomerate model presented in this thesis is based on the following assumptions:

- The fuel cell is at steady state.
- The fuel cell is at constant temperature and pressure.
- The gas diffusion layer is composed of void space and carbon fibers.
- The catalyst layer is composed of agglomerates made of a mixture of platinum supported on carbon and ionomer membrane electrolyte and surrounded by void space, Figure 2.2.
- The electrochemical reaction occurs inside the agglomerates.

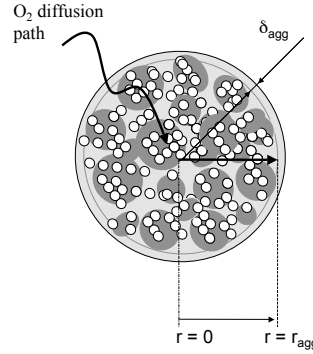


Figure 2.3: Agglomerate and thin film structure, [100]

- The transport of reactants from the gas channels to the catalyst layer occurs only by diffusion of oxygen gas to the agglomerate surface, and then by dissolution and diffusion through the ionomer to the reaction site, Figure 2.3.
- Oxygen gas transport in the GDL and the CL is modeled using Fick's first law instead of the Maxwell-Stefan equations to reduce the nonlinearity of the system of equations under the assumptions in equation (2.21).

Given these assumptions, the system of governing equations remains the same as in the previous model (2.29) with the exception of the source terms which now take a different form in order to account for the different oxygen transport mechanisms and the location of the reaction. This model was recently introduced by Secanell et al. [91] and it is based on the model presented by Sun et al. [15] with additional equations used to relate the transport properties to the catalyst layer structure.

In the agglomerate model, oxygen travels by diffusion to the surface of the agglomerate, and once the oxygen reaches the surface of the agglomerate, it dissolves into the electrolyte phase. This process is the same as the one reported in the pseudo-homogeneous model above and it is described by equation (2.24). However, after

oxygen has dissolved into the electrolyte, it is transported by diffusion through the electrolyte film surrounding the agglomerate, Figure 2.3. This transport process is described by [15]

$$\hat{N}_{O_2} = D_{O_2,N} \frac{\partial c_{O_2}}{\partial r} = D_{O_2,N} \frac{r_{agg}}{r_{agg} + \delta_{agg}} \frac{c_{O_2,g|l} - c_{O_2,l|s}}{\delta_{agg}} \quad (2.38)$$

where  $\hat{N}_{O_2}$  is the oxygen flux through the agglomerate boundary,  $c_{O_2,l|s}$  is the concentration of dissolved oxygen inside the agglomerate at the electrolyte solid interface and  $D_{O_2,N}$  is the diffusion coefficient of oxygen in Nafion<sup>TM</sup> [15].

The oxygen also diffuses inside the agglomerate as it reacts. This transport process is given by

$$D^{eff} \frac{1}{r^2} \frac{\partial}{\partial r} \left( r^2 \frac{\partial c_{O_2}}{\partial r} \right) = -c_{O_2} k_c \quad (2.39)$$

where  $k_c$  is the reaction rate computed using equation (2.45) and the diffusion coefficient inside the agglomerate,  $D^{eff}$ , is given by Bruggemann's relation

$$D^{eff} = D_{O_2,N} \epsilon_{agg}^{1.5} \quad (2.40)$$

where  $D_{O_2,N}$  is the oxygen diffusion inside the electrolyte, in this case Nafion<sup>TM</sup>. This value is assumed constant inside the catalyst layer. Analytical integration of equation (2.39) yields an effectiveness factor,  $E_r$ , for the reaction inside the agglomerate such that the oxygen reaction in the catalyst layer can be written as [15]

$$R_{O_2} = (1 - \epsilon_V^{cl}) E_r k_c c_{O_2,l|s} \quad (2.41)$$

where expressions for  $E_r$  and  $k_c$  are given in equations (2.46) and (2.45) respectively.

Using this last equation, equations (2.34) and (2.38) and the mass balance of

oxygen in the catalyst layer equations [15]

$$\nabla \cdot (c_{tot} D_{O_2}^{eff} \nabla x_{O_2}) = a_{agg} \hat{N}_{O_2} \quad (2.42)$$

$$\nabla \cdot (c_{tot} D_{O_2}^{eff} \nabla x_{O_2}) = R_{O_2} \quad (2.43)$$

the following expression for the volumetric current density is obtained [15]

$$\nabla \cdot \mathbf{i} = 4F \frac{p_{tot} x_{O_2}}{H_{O_2,N}} \left( \frac{1}{E_r k_c (1 - \epsilon_V^{cl})} + \frac{(r_{agg} + \delta_{agg}) \delta_{agg}}{a_{agg} r_{agg} D_{O_2,N}} \right)^{-1} \quad (2.44)$$

where

$$k_c = \frac{A_v i_0^{ref}}{4F(1 - \epsilon_V^{cl}) c_{O_2}^{ref}} \exp \left( -\frac{\alpha_c F}{RT} (\phi_s - \phi_m) \right) \quad (2.45)$$

The term  $1 - \epsilon_V^{cl}$  is used to transform the active area in the catalyst layer,  $A_v$ , to an active area inside the agglomerate and the effectiveness factor is given by

$$E_r = \frac{1}{\phi_L} \left( \frac{1}{\tanh(3\phi_L)} - \frac{1}{3\phi_L} \right) \quad (2.46)$$

Thiele's modulus for a spherical agglomerate,  $\phi_L$ , is given by

$$\phi_L = \frac{r_{agg}}{3} \sqrt{\frac{k_c}{D^{eff}}} \quad (2.47)$$

where  $r_{agg}$  is the radius of the spherical agglomerate and  $D^{eff}$  is the effective oxygen diffusion coefficient inside the agglomerate in equation (2.40). In case of a non-spherical agglomerate [49]

$$r_{agg} = 3 \frac{V_{agg}}{S_{agg}} \quad (2.48)$$

where  $S_{agg}$  and  $V_{agg}$  are the external surface and volume of a single agglomerate respectively.

In these equations, there are several parameters that need to be obtained:  $H_{O_2,N}$ ,  $a_{agg}$ ,  $D_{O_2,N}$ ,  $A_v$ ,  $i_0^{ref}$ ,  $c_{O_2}^{ref}$  and  $D^{eff}$ . Parameters  $H_{O_2,N}$ ,  $D_{O_2,N}$ ,  $i_0^{ref}$  and  $c_{O_2}^{ref}$  are input

parameters to the model and are obtained from transport and electrochemical data. Parameters  $a_{agg}$ ,  $A_v$  and  $D^{eff}$ , however, depend on the composition of the catalyst layer.

The parameter  $a_{agg}$  is defined as the ratio between the effective surface area usable to dissolve oxygen into the agglomerate to the catalyst layer volume. This value can be related to the catalyst layer structure by

$$a_{agg} = n4\pi(r_{agg} + \delta_{agg})^2 \epsilon_V^{cl} \quad (2.49)$$

where  $n$  is the number of agglomerates per unit volume, the term  $4\pi(r_{agg} + \delta_{agg})^2$  is the surface of a single agglomerate and  $\epsilon_V^{cl}$  is the catalyst layer porosity. The catalyst layer porosity is used to compute the effective surface area. Taking into account that oxygen gas only exists in the void phase, i.e. the gas pores, only the fraction of the surface of the agglomerate in contact with the gas pore is able to dissolve oxygen. Since the agglomerates contain all the solid and electrolyte phase, only the pores separate the agglomerates. If there is more space available for pores, then there will also be more exposed surface of the agglomerate. This can be understood by imagining an increase in the volume of the white space in Figure 2.2. This would certainly make the surface of the agglomerate more exposed to the pore. In the extreme case of zero porosity, the catalyst layer would only contain square shaped agglomerates packed together. Since there would be no space for the pores to reach the surface, the oxygen dissolution into the agglomerates in this case would be zero. Similarly, if the porosity were close to unity, the agglomerates would be separated almost completely from each other by gas pores, connected only by small strings of electrolyte. In this case, all the surface area of the agglomerate would be available for the reaction. A more detailed expression for  $a_{agg}$  that accounts for the pore size distribution inside the catalyst layer should be developed in future work.

The parameter  $A_v$  represents the area utilized for the oxygen reduction reaction

per unit volume of catalyst layer and is obtained using equations (2.36) and (2.37).

### Volume fraction of each phase in the gas diffusion layer and catalyst layer

In the GDL, only two phases exist and they are related by

$$\epsilon_V^{gdl} + \epsilon_S^{gdl} = 1 \quad (2.50)$$

where  $\epsilon_V^{gdl}$  is the GDL porosity and  $\epsilon_S^{gdl}$  is the volume fraction occupied by electric conductive material, i.e. carbon fibres. Given the GDL porosity,  $\epsilon_V^{gdl}$ , the solid phase volume fraction can easily be obtained.

In order to compute the effective properties of the CL, the volume fraction of each material in the catalyst layer i.e. solid, electrolyte and void space, need to be obtained. Generally, in previous literature, either the effective properties were assumed directly or the volume fractions were given independently of the catalyst layer ink composition, and the effective parameters were estimated using these volume fractions [15, 16]. However, the catalyst layer ink composition must dictate the amount of each one of these materials in the catalyst layer because the ink is used to create the layer. The CL ink composition is given by: platinum loading, platinum to carbon ratio and electrolyte volume fraction.

The solid phase volume fraction is given by the amounts of platinum and carbon in the catalyst layer. These values can be obtained from the platinum mass loading,  $m_{Pt}$  and the mass platinum to carbon ratio,  $Pt|C$ . Both these values are known a priori and therefore, these should be used to compute the volume fraction in the solid phase. In this model, the solid phase volume fraction,  $\epsilon_S^{cl}$ , is computed using [20]

$$\epsilon_S^{cl} = \left( \frac{1}{\rho_{Pt}} + \frac{1 - Pt|C}{Pt|C\rho_c} \right) \frac{m_{Pt}}{L} \quad (2.51)$$

where  $\rho_{Pt}$  and  $\rho_c$  are the platinum and carbon densities,  $Pt|C$  is the platinum to

carbon ratio,  $m_{Pt}$  is the platinum loading and  $L$  is the catalyst layer thickness. This last parameter is not known a priori but it can be controlled during the electrode preparation [46] or obtained a posteriori.

If the pseudo-homogeneous model is used, assuming that the electrolyte volume fraction,  $\epsilon_N^{cl}$ , is given, the porosity can be obtained readily using

$$\epsilon_V^{cl} = 1 - \epsilon_N^{cl} - \epsilon_S^{cl} \quad (2.52)$$

If the agglomerate model is used, the model input is the amount of the electrolyte in the agglomerate and the thickness of the electrolyte thin film surrounding the agglomerate. Therefore, some extra computations are necessary to obtain the total electrolyte volume fraction and the porosity. Assuming that the catalyst layer is made of spherical agglomerates and that the agglomerates are made only of ionomer and solid phase as shown in figures 2.2 and 2.3, then the total volume occupied by the solid phase in the catalyst layer can be related to the volume occupied by the agglomerates by

$$\epsilon_S^{cl} LH = \hat{n} \frac{4}{3} \pi r_{agg}^3 (1 - \epsilon_{agg}) \quad (2.53)$$

where  $L$  and  $H$  are the thickness and width of the catalyst layer,  $\hat{n}$  is the number of agglomerates in the catalyst layer,  $r_{agg}$  is the radius of the agglomerate and  $\epsilon_{agg}$  is the volume fraction of ionomer inside the agglomerate. Then, rearranging the expression above, the number of agglomerates per unit volume,  $n$ , can be expressed as

$$n = \frac{\hat{n}}{LH} = \frac{\epsilon_S^{cl}}{\frac{4}{3} \pi r_{agg}^3 (1 - \epsilon_{agg})} \quad (2.54)$$

In this equation,  $n$  represents the number of agglomerates per unit volume necessary to obtain the given volume fraction of solid phase. In this study, it is assumed that the shape of the agglomerates is spherical on an average basis and that, in reality, they would change their shape in such a way that they would always fit into the catalyst

layer's volume and thickness. That is, the method does not account for the unused space between spherical agglomerates due to their geometry and it is considered that all the catalyst layer could conceivably be filled with agglomerates.

Once the number of spherical agglomerates is obtained, and assuming that all ionomer in the catalyst layer is present either in the bulk of the agglomerate or the thin film surrounding the agglomerate, as illustrated in Figure 2.3, the electrolyte volume fraction in the catalyst layer can be obtained using geometrical arguments. The volume fraction of ionomer in the catalyst layer is

$$\epsilon_N^{cl} = \frac{4}{3}\pi n[r_{agg}^3\epsilon_{agg} + ((r_{agg} + \delta_{agg})^3 - r_{agg}^3)] \quad (2.55)$$

where  $\delta_{agg}$  is the average thickness of the ionomer film surrounding the agglomerates. This expression is obtained by taking into account both the volume occupied by the electrolyte film and the volume of the agglomerate sphere occupied by the electrolyte.

Once the volume fraction of solid phase and ionomer are obtained, the porosity of the catalyst layer is obtained using equation (2.52) as in the previous case for the pseudo-homogeneous model. Equation (2.52) gives the total porosity, i.e. the space that is occupied by neither the electrolyte nor the solid phase and that is represented in Figure 2.2 in white. This value should be interpreted as the volume fraction of the catalyst layer available for the formation of macro-pores for oxygen transport, and not as the interstitial space between spheres.

### **GDL effective parameters**

The gas diffusion layer and the catalyst layer are both porous materials. In order to account for the effects of porosity, and for the tortuous path of the transport of species, the diffusion coefficients and the conductivities need to be corrected by an expression that depends on either porosity, or both porosity and tortuosity. These corrections depend on the structure of the porous media and, therefore, in order to

obtain an expression for effective coefficients, either experiments or direct numerical simulations are necessary.

In fuel cells, several expressions have been used to compute effective properties. The most common method used to obtain effective diffusivities and conductivities is Bruggeman's relation

$$P^{eff} = P\epsilon^{1.5} \quad (2.56)$$

where  $P$  represents the property and  $\epsilon$  the volume fraction of the transporting phase. For example, in the case of gas diffusivities

$$D^{eff} = D\epsilon_V^{1.5} \quad (2.57)$$

where  $D$  represents the gas diffusivity and  $\epsilon_V$  the void volume fraction. Bruggeman's equation was obtained from experiments using beds of spherical particles of different sizes [18, 101]. Therefore, even though this equation is the most commonly used expression in fuel cell modeling, it is not correct for the GDLs. GDLs are made of carbon fibers, and their structure is quite different from the porous media used to obtain Bruggeman's relation. Bruggeman's relation is also not the most appropriate relation for the catalyst layer, because this layer is formed of a bed of carbon particles of similar size, not of different sizes. Finally, according to Bruggeman's relation, transport will occur even if the volume fraction of the transporting phase is very small. This is in disagreement with percolation theory that suggests that in most cases there is a minimum volume fraction of transporting phase necessary to form a percolation network and, as a consequence, transport only occurs past a volume fraction threshold [102, 103].

In order to achieve more realistic effective parameters in the GDL, direct numerical simulations should be used that take into account the anisotropic nature of the fibrous media. For randomly oriented fibrous structures, Monte Carlo simulations to predict effective diffusivities were performed by Tomadakis et al. [104] and they obtained the

following relation

$$D^{eff} = D\epsilon_V \left( \frac{\epsilon_V - \epsilon_{th}}{1 - \epsilon_{th}} \right)^\mu \Theta(\epsilon_V - \epsilon_{th}) \quad (2.58)$$

where  $D$  is the diffusion coefficient,  $\epsilon_V$  is the void fraction,  $\epsilon_{th}$  and  $\mu$  are constants that depend on the orientation of the fibers and the function  $\Theta(\epsilon_V - \epsilon_{th})$  is the Heaviside unit step function which takes the values

$$\Theta(\epsilon_V - \epsilon_{th}) = \begin{cases} 0 & \text{if } \epsilon_V < \epsilon_{th} \\ 1 & \text{if } \epsilon_V \geq \epsilon_{th} \end{cases} \quad (2.59)$$

In the case of in-plane randomly oriented fibers, the in-plane and through-plane effective diffusivities can be obtained by taking  $\mu = 0.521$  and  $0.785$  respectively and  $\epsilon_{th} = 0.11$ . This relationship is used in this thesis. These values were also discussed in Nam et al. [105] and Pharoah et al. [18]. In the latter, numerical results are presented using both Bruggeman's relation and this last relation and the differences are highlighted.

For the GDL conductivity, to date, there have been no studies done to obtain a relationship between the solid phase volume fraction and the anisotropic effective conductivities. However, as discussed in the previous paragraph, it is clear that, due to the in-plane orientation of the fibres in the GDL, the effective in-plane and through-plane conductivities should have different values. This has been shown experimentally. For example, the Toray TGP-H GDL series has in-plane and through-plane effective resistivities of  $0.08$  and  $0.0058 \Omega cm$  [106]. Furthermore, it is most likely that a different relationship with respect to the solid phase volume fraction exists. For this reason, in this thesis, it is suggested that the GDL conductivity is given by

$$\sigma_S^{eff} = \sigma_S \epsilon_S^\mu \quad (2.60)$$

where  $\mu$  is  $1.0$  and  $1.5$  for the in-plane and through-plane conductivities respectively. The difference in the exponent value is due to the nature of the GDL. In-plane, the electrons are transported on the same fibers for large distances since the fibers are of

3-12 millimeters in length [107]. On the other hand, in the through-plane direction, the electrons must continuously jump from fiber to fiber which have diameters in the order of  $7 \mu m$  [107], resulting in a much more tortuous path and hence requiring a larger coefficient to reflect the tortuous path. Notice that in the through-plane direction, the expression becomes Bruggeman's relation. The values of  $\sigma_S$  for the in-plane and through-plane conductivities are 272.78 and 16.02  $S/cm$  respectively. Due to the lack of data available, these values are obtained by fitting the Toray TGP-H series conductivities reported in reference [106], to the expression above.

### CL effective parameters

Due to the random structure of the catalyst layer, the author suggests that the most appropriate method for studying its effective transport properties is by using percolation theory. This is in agreement with several articles in PEM and SOFC modeling [39, 102, 108, 109]. Percolation theory tries to study the properties of randomly distributed systems and, in particular, it can be used to study the properties of random porous media. To begin the study of randomly distributed media using percolation theory, it is necessary to prescribe a space where the medium is to be distributed, e.g. in a porous media where pores and solid will exist. To do so, imagine a large array of place holders that together fill a space, such as small squares that together form a surface like the one shown in Figure 2.4a. An infinite space divided into small place holders, most commonly known as sites, is called a lattice. There can be an infinite number of lattices depending on the space dimension,  $d$ , and lattice structure.

In order to create the randomly distributed media, it is assumed that a site or holder is either occupied or empty, with a probability  $p$ . Going back to the porous media example, it is assumed that there is a probability  $p$  that a site is a solid and a probability  $1 - p$  that is a pore. Then, using this probability and a random number generator, the holders are fill out such that the result is a lattice such as the one in

Figure 2.4b. From the figure, it can be observed that even though the distribution is random, several groups of occupied neighboring sites have appeared. A cluster is then defined as a group of neighboring sites. Neighboring sites are defined as occupied sites that share at least one face in common (if they share a vertex they are known as next nearest neighbors). Figure 2.4c shows the clusters formed in the square lattice. It is easy to see that as the probability  $p$  increases, more and larger clusters will form. At a specific probability  $p_c$ , known as the percolation threshold, a cluster will span from the top plane to the bottom plane of the lattice as in Figure 2.4a. For probability  $p = 1$ , all sites are occupied and the randomly distributed media becomes a homogeneous media.

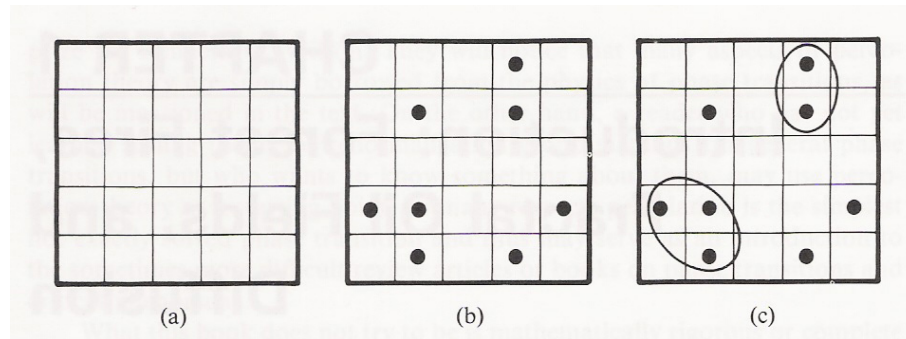


Figure 2.4: Definition of a lattice, an occupied site and a cluster. (a) part of a square lattice, (b) a square lattice with several occupied sites, (c) two clusters of different sizes on the lattice, represented by the circle. Figure from reference [103]

Percolation theory is used to study, for any given lattice, the geometrical properties of the clusters formed at a given probability,  $p$ ; the probability at which a cluster that spans from side to side of a lattice, known as an infinite cluster (usually for infinite lattices) or percolating cluster (usually for finite lattices) is formed and, finally; the effects of the probability  $p$  on properties of the distributed media. Analytical studies exist for simple two dimensional lattices and for the Bethe lattices, but in general, in order to obtain cluster properties and properties of complex randomly distributed media Monte Carlo simulations are necessary. References [103, 110] contain a table

of the most important properties for several lattices of two- and three-dimensions. Percolation as defined thus far has been known as site percolation. However, there is another type of percolation known as bond percolation. This case can be studied by imagining that all sites in the lattice are occupied, and that the lines drawn between neighboring lattice sites are open, with a probability of  $p$ , or closed, with a probability of  $p - 1$  [103].

Neglecting the effects of the agglomerate structure on effective transport properties, the catalyst layer can be idealized to be a randomly distributed media. The catalyst layer can then be studied as a site or bond percolation problem in which three types of sites of equal size exist: electron conductor sites (carbon black supporting the catalyst), void space sites and electrolyte sites with probabilities  $x_{el}$ ,  $x_m$  and  $x_v$  and  $x_{el} + x_m + x_v = 1$ . Making the probabilities  $x_{el}$ ,  $x_m$  and  $x_v$  proportional to the volume fraction of each one of the materials, the catalyst layer composition is readily related to the probability of a site being occupied. Furthermore, for solid oxide [102, 109, 111] and PEM [39, 47, 108] fuel cell studies, it is common to assume that a three-dimensional face-centered cubic (FCC) lattice, which represents a close packing of sites, can represent the catalyst layer appropriately [109, 111, 112]. Recently, other lattices that account for random particle size have also been studied for PEM fuel cells [113]. For this thesis, it is assumed that the sites are distributed in a three-dimensional FCC lattice as illustrated in Figure 2.5. Figure 2.5 is a conceptualization of a SOFC catalyst layer. Percolation theory to model catalyst layers was first introduced in the solid oxide fuel cell (SOFC) literature because in SOFCs the electrolyte is made of ceramic particles and the result is an almost ideal random media. A 3D FCC lattice is formed by using the sites of a face-centred cube. Figure 2.5 is then produced by looking at a (111) plane of the lattice structure. In the figure, each site is represented by a colored circle. We can see the formation of small clusters for each type of site. Percolation theory can now be used with this lattice structure to study the properties of the catalyst layer for a given catalyst layer composition.

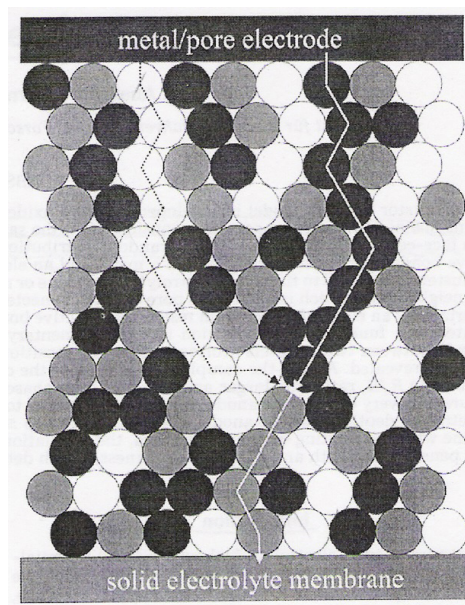


Figure 2.5: Percolation lattice of a SOFC anode catalyst layer. The black, grey and white circles represent electric conductor or carbon grains, electrolyte and pores respectively. The two solid lines show the current's path through the system. The dashed line is the fuel path to the reaction site. Figure from reference [111]

In order for electrons to reach the catalytic sites, the catalyst layer needs a cluster of electron conducting sites that is in contact with the GDL fibers as shown in Figure 2.5 by the black circles. Since electron conductive sites are placed randomly, it is difficult to evaluate when a cluster will reach the GDL and how deep into the CL it will go. However, percolation theory can easily be used to evaluate when a cluster is formed that traverses the catalyst layer. This will happen at the percolation threshold. In this work, it is assumed that the catalyst layer has zero conductivity if there is not a percolating or infinite cluster formed, i.e. below the percolation threshold. Notice that this is a conservative approximation because before a percolating cluster is formed, small clusters could be formed next to the GDL that would allow partial electron transport in the CL. When the probability of having an occupied site, in this case a site that contains electron conductive material, increases above the threshold, an infinite cluster is formed and conductivity increases following some function of the probability of occupied sites.

Following the reasoning above, and noticing that  $\epsilon_S$ , the volume fraction of the solid phase, is equivalent to the probability of a site containing electron conductive material, the effective electron conductivity can be estimated using [39, 47, 103, 108, 110, 114]

$$\sigma_S^{eff} = \sigma_S \left( \frac{\epsilon_S^{cl} - \epsilon_{th}}{1 - \epsilon_{th}} \right)^\mu \Theta(\epsilon_S^{cl} - \epsilon_{th}) \quad (2.61)$$

where  $\sigma_S$  is the electron conductivity of the pure electronic conductor material, usually carbon black supporting the catalyst,  $\epsilon_S^{cl}$  is the volume fraction of the electron conductive material and,  $\epsilon_{th}$  and  $\mu$  are the percolation threshold and, in principle, a universal exponent respectively [103]. Finally, the term  $1 - \epsilon_{th}$  in the denominator is included so that at  $\epsilon_S = 1$ , i.e. when the catalyst layer contains only solid, the effective electron conductivity is equal to the conductivity of the carbon black. This term is not included in all references because percolation theory is primarily concerned with proportionality and not with exact values; however, it is clear that at  $\epsilon_S = 1$ ,  $\sigma^{eff}$  has to be equal to  $\sigma_S$  and therefore in this instance the term is necessary.

In equation (2.61), all values are known constants but  $\mu$  and  $\epsilon_{th}$ . Out of these two constants, it is well known that  $\mu$  is a 'universal' constant that is independent of the lattice structure, and that it depends only on lattice dimensionality [103,110]. In particular, for two-dimensions,  $d = 2$ , it is well established that  $\mu \approx 1.3$  and for  $d = 3$ ,  $\mu \approx 1.7 - 2.0$  even though this result is more controversial [103,110,114]. In this study, because the catalyst layer is a three-dimensional lattice,  $\mu$  is set to 2.0 in accordance with previously published work [39,108]. In order to obtain a satisfactory relationship for the effective electron conductivity, it suffices to find a value for  $\epsilon_{th}$ .

$\epsilon_{th}$  is the percolation threshold value, which is strongly dependent upon both the lattice structure and its dimensionality. Even though the lattice dimensionality is known, the lattice structure that approximates the catalyst layer is more difficult to obtain. For a three-dimensional lattice,  $d = 3$ , the percolation threshold ranges from values of 0.425 for site percolation on a diamond lattice to values of 0.119 for bond percolation on a face-centered cubic (FCC) lattice [110]. Fortunately, Pantea et al. [115] have published conductivity data for packed Vulcan XC-72 carbon black, which is the most commonly used carbon for supporting the catalyst particles. This data can be used to estimate the values of  $\sigma_S$  and  $\epsilon_{th}$ . Note that in this case  $\sigma_S$  is not taken to be equal to the conductivity of carbon because for  $\epsilon_S^d = 1$  this value needs to contain the contact resistances between carbon particles. To estimate  $\sigma_S$  and  $\epsilon_{th}$ , a least-square problem is solved to fit the data in reference [115] to equation (2.61). After curve fitting,  $\sigma_S$  and  $\epsilon_{th}$  take the values of  $88.84S/cm$  and 0.118 respectively. Notice that  $\mu$  is a universal constant; therefore, it is not used as a fitting parameter. Figure 2.6 shows the experimental data and a curve fit using the percolation equation and also Bruggeman's relation with the conductivity,  $\sigma_S$ , as a fitting parameter. It is clear from the figure that there is an advantage to using percolation. The curve obtained by percolation theory closely approximates the data from Pantea et al. in the whole range of experimental values. On the other hand, Bruggemann's equation is only close to the experimental values for solid phase volume fractions of 0.3.

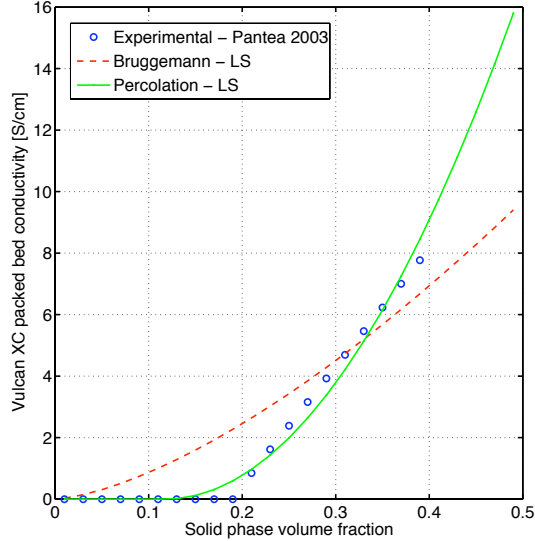


Figure 2.6: Curve fit to the experimental data reported by Pantea et al. [115]

The threshold value obtained by curve fitting of 0.118 is very similar to the threshold value of 0.119 for bond percolation in an FCC lattice. This data provides some evidence that the most appropriate percolation type and lattice structure for modeling the catalyst layer is a bond percolation on a FCC lattice. Since there is some controversy regarding the value of  $\mu$ , the curve fit was also performed with  $\mu = 1.7$ , i.e. its lowest value. In this case,  $\sigma_S$  and  $\epsilon_{th}$  take the values of  $67.54S/cm$  and 0.139. The threshold value is slightly higher than the one predicted by bond percolation on a FCC lattice. This value lies in between the threshold value for a bond percolation of an FCC lattice and a body-centered cubic (BCC) lattice, i.e. 0.178, as shown in table 2.1. The threshold obtained by curve-fitting the data from Pantea et al. is also in agreement with recent publications [39, 108] where either site or bond percolation on a face-centered cubic lattice was used. In reference [39] a value of  $\epsilon_{th} = 0.12$  (bond percolation on a FCC lattice) was used. On the other hand, in reference [108], a value of  $\epsilon_{th} = 0.19$  (site percolation on a FCC lattice) was used instead. Neither of

Table 2.1: Sample percolation threshold for different three-dimensional,  $d = 3$ , lattices. Data from [110]

Lattice	Bond	Site
Simple Cubic	0.24	0.307
Body-centered cubic	0.178	0.243
Face-centered cubic	0.119	0.195
Diamond	0.388	0.425

these publications provided a justification for the selection of the lattice structure. Therefore, the present work provides the first study that includes a justification for the use of a threshold for bond percolation on an FCC lattice.

Applying a similar reasoning to the electron conductive phase, and noticing that  $\epsilon_N^{cl}$ , the volume fraction of the electrolyte, is equivalent to the probability of a site containing electrolyte, then, the effective proton conductivity of the catalyst layer can be approximated by [39, 47, 103, 108, 110, 114]

$$\sigma_m^{eff} = \sigma_m \left( \frac{\epsilon_N^{cl} - \epsilon_{th}}{1 - \epsilon_{th}} \right)^\mu \Theta(\epsilon_N^{cl} - \epsilon_{th}) \quad (2.62)$$

where  $\sigma_m^{eff}$  is the effective proton conductivity,  $\sigma_m$  is the proton conductivity of the electrolyte,  $\epsilon_{th}$  is the percolation threshold,  $\mu$  is, in principle, a universal constant [103] and  $\Theta(\epsilon_N - \epsilon_{th})$  is the Heaviside unit step function given in equation (2.59). It is assumed that since both electrolyte and electronic conductor exist on the same lattice coefficients,  $\epsilon_{th}$  and  $\mu$ , take the same values as in equation (2.61). The percolation value of 0.119 for the proton conductivity can also be supported by its agreement with the experimental data presented by Gode et al. [46] where for very small values of electrolyte, a large decline in electrode performance can be observed. Based on their data, the threshold of 0.119 might be a slightly conservative figure. This difference is most likely due to the presence of conducting clusters that are in contact with the membrane prior to the formation of a percolating network.

Diffusivity in a random network is proportional to the conductivity of a random resistor network [103]. Therefore, diffusivity will be related to the void or porous volume fraction by a similar expression to the ones shown in the last two sections. The reason for this proportionality is that in statistical physics diffusivity and conductivity are both proportional to mobility; therefore, they must be proportional to each other. Then, the effective diffusivity of species  $i$ ,  $D_i^{eff}$ , can be written as

$$D_i^{eff} = D_i \left( \frac{\epsilon_V^{cl} - \epsilon_{th}}{1 - \epsilon_{th}} \right)^\mu \Theta(\epsilon_V^{cl} - \epsilon_{th}) \quad (2.63)$$

where  $D_i$  is the diffusivity constant of the gas  $i$ , in this case oxygen, in the absence of network constraints,  $\epsilon_V^{cl} = 1 - \epsilon_N^{cl} - \epsilon_S^{cl}$  is the volume fraction of void space,  $\epsilon_{th}$  and  $\mu$  are the percolation threshold and a 'universal' constant respectively.  $\epsilon_{th}$  and  $\mu$  take the same value as in equation (2.62) since pores, electrolyte and electronic conductor exist on the same lattice and therefore, these coefficients must be the same. Notice that in reference [108] the authors wrote that a different value for  $\mu$  could be used when estimating the diffusivity and the conductivity, even though in the article they used the same value for simplicity. Taking into account that  $\mu$  is, in principle, a universal constant that depends only on dimensionality, and that conductivity and diffusivity are proportional, the coefficient  $\mu$  for diffusivity and conductivity should always be the same according to percolation theory [103]. Finally, the percolation threshold value of 0.119 is in accordance with the experimental data presented by Gode et al. in reference [46] where for electrode porosities in the range of 0.2 - 0.1, large drops in performance can be observed at high current densities.

## 2.1.2 Numerical solution

The system of partial differential equations (PDE) that describes the cathode electrode model in equation (2.29) is discretized using the finite element method. In particular, the Galerkin method is used with a set of second order elements. The

implementation of the numerical procedure was performed using the linear solvers, element shape functions and adaptive meshing algorithms given in deal.ii: Finite Element Differential Equations Analysis Library, [116]. In this section, the variational form of the problem is developed, the discretization of the variational equation is described and, the algorithms used for the solution of the problem are stated.

### Linearization and weak formulation

Each equation in the system of PDEs in (2.29) can be written in matrix notation as

$$\nabla \cdot (\mathbf{A}(\mathbf{u})\nabla u) = f(\mathbf{u}) \quad (2.64)$$

where  $\mathbf{A}$  is a second order tensor that provides the effective transport values in each direction and  $f(\mathbf{u})$  is a nonlinear source term that could depend on all unknowns of the system of equation. As an example, for the oxygen transport

$$\mathbf{A}(\mathbf{u}) = \mathbf{A} = \begin{pmatrix} c_{tot}D_{O_2,xx}^{eff} & 0 & 0 \\ 0 & c_{tot}D_{O_2,yy}^{eff} & 0 \\ 0 & 0 & c_{tot}D_{O_2,zz}^{eff} \end{pmatrix} \quad (2.65)$$

$$\mathbf{u} = \begin{pmatrix} x_{O_2} \\ \phi_m \\ \phi_S \end{pmatrix} \quad (2.66)$$

$$f(\mathbf{u}) = \frac{1}{4F}\nabla \cdot \mathbf{i} \text{ and } u = x_{O_2}.$$

Due to the nonlinear source term,  $f(\mathbf{u})$ , the equations that form the system of equations in (2.29) are all nonlinear. A nonlinear equation such as the one above can be solved by means of an iterative procedure where a linearization of the system is solved. Starting with an initial guess solution  $\mathbf{u}^0$ , a solution increment is obtained,  $\delta\mathbf{u}$ , by solving a linearization of the nonlinear problem. Then, the solution is updated

$\mathbf{u}^{n+1} = \mathbf{u}^n + \delta\mathbf{u}$ . This process is repeated until the solution increment, i.e. the solution of the linearized system  $\delta\mathbf{u}$ , approaches zero. This is known as the Newton-Raphson method for solving nonlinear systems [117].

In order to be able to solve the nonlinear system of equations using the Newton-Raphson method, a linearization of the nonlinear equations must be obtained. This is done prior to obtaining the variational formulation of the equations by linearizing the equations around  $\mathbf{u}^n$ . Using directional derivatives of functional analysis [118, 119], the left hand side of equation (2.64) becomes

$$\nabla \cdot (\mathbf{A}(\mathbf{u}^{n+1})\nabla u^{n+1}) \approx \nabla \cdot \left[ \mathbf{A}(\mathbf{u}^n)\nabla u^n + \left( \frac{\partial \mathbf{A}(\mathbf{u})}{\partial u_k} \Big|_{\mathbf{u}=\mathbf{u}^n} \delta u_k \right) \nabla u_i^n + \mathbf{A}(\mathbf{u}) \Big|_{\mathbf{u}=\mathbf{u}^n} \nabla \delta u \right] \quad (2.67)$$

and the right hand side of the equation becomes

$$f(\mathbf{u}^{n+1}) \approx f(\mathbf{u}^n) + \frac{\partial f(\mathbf{u})}{\partial u_k} \Big|_{\mathbf{u}=\mathbf{u}^n} \delta u_k \quad (2.68)$$

where  $\frac{\partial}{\partial u_k}$  represents the derivative with respect to unknown  $k$  of the problem and  $\delta u_k$  the increment of the unknown  $u_k$ . Note that each of these increments,  $\delta u_k$ , is obtained by solving the complete system of discretized equations. Then, the terms  $\frac{\partial \mathbf{A}}{\partial u_k} \Big|_{\mathbf{u}=\mathbf{u}^n}$ ,  $f(\mathbf{u})$  and  $\frac{\partial f(\mathbf{u})}{\partial u_k} \Big|_{\mathbf{u}=\mathbf{u}^n}$  can be understood as the coupling terms between the different equations. Assuming that the diffusion coefficient and conductivities do not depend on any of the unknowns, all the governing equations in the system in equation (2.64) have a constant matrix  $\mathbf{A}$  and, as a consequence, the term  $\frac{\partial \mathbf{A}}{\partial u_k}$  vanishes. Then, using (2.67) and (2.68) the linearized form of equation (2.64) around  $\mathbf{u}^n$  is

$$\nabla \cdot (\mathbf{A}\nabla u^n + \mathbf{A}\nabla \delta u) = f(\mathbf{u}^n) + \frac{\partial f(\mathbf{u})}{\partial u_k} \Big|_{\mathbf{u}=\mathbf{u}^n} \delta u_k \quad (2.69)$$

Once the problem has been linearized, the Galerkin method is used in order to obtain the variational or weak formulation. In order to obtain the weak formulation, the equation is multiplied by a test function,  $v$ , and the equation is integrated over

the domain. This results in

$$\int_{\Omega} v[\nabla \cdot (\mathbf{A}\nabla u^n + \mathbf{A}\nabla \delta u)]d\Omega = \int_{\Omega} v \left[ f(\mathbf{u}^n) + \frac{\partial f(\mathbf{u})}{\partial u_k} \Big|_{\mathbf{u}=\mathbf{u}^n} \delta u_k \right] d\Omega \quad (2.70)$$

This last equation can be rearranged using the relation from vectorial calculus [49],

$$s(\nabla \cdot \mathbf{v}) = \nabla \cdot s\mathbf{v} - \nabla s \cdot \mathbf{v} \quad (2.71)$$

where  $s$  is a scalar quantity and  $\mathbf{v}$  is a vector into

$$\begin{aligned} \int_{\Omega} \nabla \cdot [v(\mathbf{A}\nabla u^n + \mathbf{A}\nabla \delta u)] d\Omega - \int_{\Omega} (\nabla v) \cdot (\mathbf{A}\nabla u^n + \mathbf{A}\nabla \delta u) d\Omega = \\ \int_{\Omega} v \left[ f(\mathbf{u}^n) + \frac{\partial f(\mathbf{u})}{\partial u_k} \Big|_{\mathbf{u}=\mathbf{u}^n} \delta u_k \right] d\Omega \end{aligned} \quad (2.72)$$

This equation can be further reduced using the divergence theorem [49]

$$\int_{\Omega} (\nabla \cdot \mathbf{v}) d\Omega = \int_{\partial\Omega} (\mathbf{n} \cdot \mathbf{v}) d\partial\Omega \quad (2.73)$$

where  $\mathbf{v}$  is a vector function and  $\mathbf{n}$  is the normal to the domain boundary,  $\partial\Omega$ . Then, the system of equations becomes

$$\begin{aligned} \int_{\partial\Omega} \mathbf{n} \cdot v\mathbf{A}\nabla u^{n+1} d\partial\Omega - \int_{\Omega} (\nabla v) \cdot (\mathbf{A}\nabla u^n + \mathbf{A}\nabla \delta u) d\Omega = \\ \int_{\Omega} v \left[ f(\mathbf{u}^n) + \frac{\partial f(\mathbf{u})}{\partial u_k} \Big|_{\mathbf{u}=\mathbf{u}^n} \delta u_k \right] d\Omega \end{aligned} \quad (2.74)$$

where the surface integral is evaluated at the problem boundary,  $\partial\Omega$ , and  $\nabla u^{n+1} = \nabla u^n + \nabla \delta u$ . Rearranging to leave on the left hand side only the terms with the

unknown,  $\delta u$ ,

$$\begin{aligned}
& - \int_{\Omega} (\nabla v) \cdot (\mathbf{A} \nabla \delta u) d\Omega - \int_{\Omega} v \frac{\partial f(\mathbf{u})}{\partial u_k} \Big|_{\mathbf{u}=\mathbf{u}^n} \delta u_k d\Omega = \\
& \int_{\Omega} v f(u^n) d\Omega + \int_{\Omega} (\nabla v) \cdot (\mathbf{A} \nabla u^n) d\Omega - \int_{\partial\Omega} \mathbf{n} \cdot (v \mathbf{A} \nabla u^{n+1}) d\partial\Omega \quad (2.75)
\end{aligned}$$

### Discretization and solution

Equation (2.75) is the weak formulation of the linearized problem. This equation is solved in the computational domain by dividing the domain into finite elements and solving the equations in each domain with the appropriate set of boundary conditions. For elements inside a continuous domain, such as inside the GDL and catalyst layer, the boundary integral is zero if the solution is continuous. At the interface between domains and at the boundaries of the computational domain, the boundary integrals must be evaluated. Fortunately, in this case, since there is continuity in the solution values across the boundary between the GL and CL, the integral vanishes and both GDL and catalyst layer can be treated as one single domain. Furthermore, the boundary conditions that will be discussed in section 2.4.2 translate into a zero value boundary integral for the system of equations. Therefore, the surface integral vanishes entirely from the analysis. Finally, the Dirichlet boundary conditions are imposed directly onto the final algebraic system of equations.

In order to solve the system of equations using the finite element method, the solution of the system and the test functions are substituted by a linear approximation in each finite element. Then, the solution and test functions for equation  $i$  are substituted by

$$\delta u_i = \phi_l \delta_{i,comp(l)} \delta u_l \quad \forall l = 1, \dots, N \quad i = 1, 2, 3 \quad (2.76)$$

$$u_i = \phi_l \delta_{i,comp(l)} u_l \quad \forall l = 1, \dots, N \quad i = 1, 2, 3 \quad (2.77)$$

$$v_i = \phi_p \delta_{i,comp(p)} v_p \quad \forall p = 1, \dots, N \quad i = 1, 2, 3 \quad (2.78)$$

where  $N$  is the degrees of freedom of the system, i.e. the number of equations times the number of nodes,  $\delta_{i,comp(l)}$  is the delta Dirac and  $comp(l)$  returns the solution component  $i$  for the system degree of freedom  $l$  where  $i = 1, 2, 3$  and  $l = 1, \dots, N$ .

For equation  $i$  in the system of equations, substituting (2.76), (2.77) and (2.78) into (2.75), taking  $u = u_i$ ,  $v = v_i$  and eliminating  $v_i$  yields

$$-\int_{\Omega} (\nabla(\phi_p \delta_{i,comp(p)})) \cdot (\mathbf{A} \nabla(\phi_l \delta_{i,comp(l)} \delta u_l)) d\Omega - \int_{\Omega} \phi_p \delta_{i,comp(p)} \frac{\partial f(\mathbf{u})}{\partial u_k} \Big|_{\mathbf{u}=\mathbf{u}^n} \phi_l \delta_{k,comp(l)} \delta u_l d\Omega = \int_{\Omega} \phi_p \delta_{i,comp(p)} f(\mathbf{u}^n) d\Omega + \int_{\Omega} (\nabla(\phi_p \delta_{i,comp(p)})) \cdot (\mathbf{A} \nabla(\phi_l \delta_{i,comp(l)} u_l)) d\Omega \quad (2.79)$$

and taking into account that  $\delta u_i$  and  $\delta$  are constant and rearranging

$$\left( \int_{\Omega} (\nabla \phi_p \cdot (\delta_{comp(p),comp(l)} \mathbf{A} \nabla \phi_l)) d\Omega + \int_{\Omega} \phi_p \delta_{i,comp(p)} \frac{\partial f(\mathbf{u})}{\partial u_{comp(l)}} \Big|_{\mathbf{u}=\mathbf{u}^n} \phi_l d\Omega \right) (-\delta u_l) = \int_{\Omega} \phi_p \delta_{i,comp(p)} f(\mathbf{u}^n) d\Omega + \int_{\Omega} \nabla \phi_p \cdot (\delta_{comp(p),comp(l)} \mathbf{A} \nabla(\phi_l u_l^n)) d\Omega \quad (2.80)$$

The last set of equations describes a system of algebraic linear equations,

$$K_{pl}(-\delta u_l) = f_p \quad (2.81)$$

where the negative sign is kept with the unknown vector in an attempt to make matrix  $K_{pl}$  semi-definite positive,  $K_{pl}$  is known as the stiffness matrix,  $f_k$  as the force vector of the system and  $p, l = 1, \dots, N$ . From equation (2.80) and (2.81), the stiffness matrix and the force vector are

$$K_{pl} = \int_{\Omega} \nabla \phi_p \cdot (\delta_{comp(p),comp(l)} \mathbf{A} \nabla \phi_l) d\Omega + \int_{\Omega} \phi_p \delta_{i,comp(p)} \frac{\partial f(\mathbf{u})}{\partial u_{comp(l)}} \Big|_{\mathbf{u}=\mathbf{u}^n} \phi_l d\Omega \quad (2.82)$$

$$f_p = \int_{\Omega} \phi_p \delta_{i,comp(p)} f(\mathbf{u}^n) d\Omega + \int_{\Omega} \nabla \phi_p \cdot (\delta_{comp(p),comp(l)} \mathbf{A} \nabla(\phi_l u_l^n)) d\Omega \quad (2.83)$$

To obtain the values of the stiffness matrix and the force vector, the integrals

are evaluated using a Gauss numerical integration with eight quadrature points. The Dirichlet boundary conditions are applied to the system by eliminating unnecessary rows. This results in a system of linear equations with a non-symmetric stiffness matrix. The non-symmetry of the stiffness matrix is due to the gradient of the source term. Due to the non-symmetric matrix, iterative linear solvers such as the conjugate gradient method do not work [120]. In this case, to solve the linear system of equations, either the direct solver UMFPACK [121,122] or the Generalized Minimal Residual (GMRES or GMRes) algorithm with an incomplete LU (ILU) preconditioner are used providing good convergence to the linear solution [116,120]. For the iterative solver, the stopping criteria is that the residual of the linear system is smaller than  $10^{-14}$ . Even though both options can be used in the code developed by the author, in this thesis, all the problems are solved using UMFPACK because it provides the solution to the linear system approximately 20 to 50 times faster. The iterative solver is implemented for the cases where the amount of memory available does not allow the use of a direct solver.

The nonlinear system is solved iteratively using the Newton-Raphson algorithm. Once the linear system in equation (2.81) is solved, the initial solution is updated using a rudimentary line search to improve robustness of the algorithm such that  $\mathbf{u}^{n+1} = \mathbf{u}^n + \alpha\delta\mathbf{u}$ . For the line search, the residual of the updated solution with  $\alpha$  equal to one is computed to verify that the new solution is successful in reducing the residual. If the updated solution does not yield an improvement, a new updated solution is obtained by adding only half the solution update vector,  $\alpha = 1/2$ , to the original solution. This process is repeated until an improvement in the residual is obtained or the solution update has been reduced ten times. Once the solution update is obtained, the linearization and solution update processes are repeated until the residual of the nonlinear governing equations is smaller than  $10^{-12}$ .

The nonlinear system is solved in a sequence of adaptively refined grids in order to achieve a grid independent solution. An adaptive refinement loop is used in order

to refine the mesh automatically during the solution process where the largest numerical errors are predicted. This allows the solver to always provide a grid independent solution, even though during optimization or parametric studies the design parameters and, as a consequence, the physics of the problem are changing. Furthermore, because refinement occurs only where the errors are largest, grid adaptivity reduces computational cost by refining the grid only where necessary.

In the adaptive refinement loop, the error estimator in each cell used to decide which areas must be refined is obtained using the *a posteriori* error estimator developed by Kelly et al. [123]

$$\eta_K^2 = \frac{h}{24} \int_{\partial K} \left[ a_h(\mathbf{x}) \frac{\partial u_h}{\partial n} \right] dA \quad (2.84)$$

and implemented in deal.ii [116]. In this case,  $\partial K$  is the cell boundary,  $n$  is the normal to the cell,  $u_h$  is the oxygen and water mole fraction and the solid and membrane potential components of the solution, and  $a_h$  is set equal to one. Note that, after using several error estimators, it was found that this error estimator resulted in a faster convergence to a grid independent solution than using all components at once. This is most likely due to the values of the electrolyte phase in the GDL which have no physical meaning and result in a meaningless error estimator. The error estimator is computed for each cell at each adaptive refinement and the 30% of cells with the highest error are refined by dividing them into four cells, while the 3% of cells with the smallest error estimation are coarsened by merging four neighboring cells. This loop is terminated after a given number of grid refinements that yield a grid independent solution.

## 2.2 Membrane modeling

### 2.2.1 Governing equations

There are primarily two species transported in the membrane: water and protons. In addition to these species, gases are also transported through diffusion; however, this transport mechanism is not accounted for in the present work. Transport of hydrogen and oxygen account for the cross-over losses, especially those losses that occur close to open circuit voltage.

There are several models that predict the transport of water and protons through the membrane. Of particular interest are the models by Bernardi et al. [32], Springer et al. [54], Thampan et al. [124], Weber et al. [53, 125, 126] and Fimrite et al. [56, 57]. Of all these models, Springer's model (a semi-empirical model) is the most widely used model. For simplicity, Springer's model is chosen to be implemented in the fuel cell framework. In the future, a more sophisticated membrane model should also be implemented such as the binary friction model of Fimrite et al. [56, 57].

#### Springer et al. model

Inside the membrane, water is transported by two different mechanisms: electro-osmotic drag and water diffusion. When using a liquid water equilibrated membrane, convective transport should also be accounted for [125]. Springer et al. model does not account for the latter transport process and, therefore should only be used for water vapour equilibrated membranes or membranes with equal pressure in anode and cathode.

Using the Springer et al. model, water transport by electro-osmotic drag is described by

$$\mathbf{N}_{w,drag} = n_d \frac{I}{F} \quad (2.85)$$

where  $I$  is the proton flux. Taking into account that, by definition

$$\mathbf{i}_p = F\mathbf{N}_{\mathbf{H}^+} = IF \quad (2.86)$$

and that Ohm's law states that

$$\mathbf{i}_p = -\sigma_m \nabla \phi_m \quad (2.87)$$

we can write the electro-osmotic drag in terms of the membrane potential as

$$\mathbf{N}_{w,drag} = -n_d \frac{\sigma_m}{F} \nabla \phi_m \quad (2.88)$$

where  $n_d$  is the electro-osmotic drag coefficient,  $F$  is Faraday's constant,  $\sigma_m$  is the membrane conductivity and  $\phi_m$  is the membrane electrical potential. In this equation, both the electro-osmotic drag coefficient and the membrane conductivity depend on the water content. The water content inside the membrane is defined by the variable  $\lambda$  which is defined as

$$\lambda = \frac{\text{moles of sorbed water}}{\text{moles of } SO_3^-} \quad (2.89)$$

and the moles of sulfonate heads,  $SO_3^-$ , in the membrane are given by either its ion exchange capacity (IEC) or its equivalent weight (EW) defined as

$$EW = \frac{1}{IEC} = \frac{\text{weight of dry polymer electrolyte in grams}}{\text{moles of } SO_3^-} \quad (2.90)$$

The electro-osmotic drag coefficient is given by [54]

$$n_d = \frac{2.5\lambda}{22} \quad (2.91)$$

The membrane conductivity is

$$\sigma_m(\lambda) = \sigma_{m,30}(\lambda) \exp \left[ 1268 \left( \frac{1}{303} - \frac{1}{T_{cell}} \right) \right] \quad (2.92)$$

where  $T_{cell}$  is the cell temperature and

$$\sigma_{m,30}(\lambda) = 0.005139\lambda - 0.00326 \quad \text{for } \lambda > 1 \quad (2.93)$$

where  $\sigma_{m,30}$  is in  $S/cm$  and  $T_{cell}$  is in Kelvin.

Water transport by diffusion in the membrane is given by [54]

$$\mathbf{N}_{w,diffusion} = -\frac{\rho_{dry}}{EW} D_\lambda \nabla \lambda \quad (2.94)$$

where  $\rho_{dry}$  and  $EW$  are the membrane density in its dry state and its equivalent weight,  $D_\lambda$  is the water diffusion coefficient and, finally,  $\lambda$  is the membrane water content as defined in equation (2.89). The water diffusion coefficient is a function of the water content and is given in Springer et al. [54] at  $\lambda > 4$  by

$$D_\lambda = D_{\lambda,30} 10^{-6} \exp \left[ 2416 \left( \frac{1}{303} - \frac{1}{T_{cell}} \right) \right] \quad (2.95)$$

and

$$D_{\lambda,30} = 2.563 - 0.33\lambda + 0.0264\lambda^2 - 0.000671\lambda^3 \quad (2.96)$$

where  $D_{\lambda,30}$  is in  $cm^2/s$  and  $T_{cell}$  is in Kelvin.

More recently, Motupally et al. [127] have reported values for the Fickian diffusion of water in the membrane by measuring the flux of water across Nafion<sup>TM</sup> 115 membranes equilibrated on one side with liquid water and on the other with nitrogen

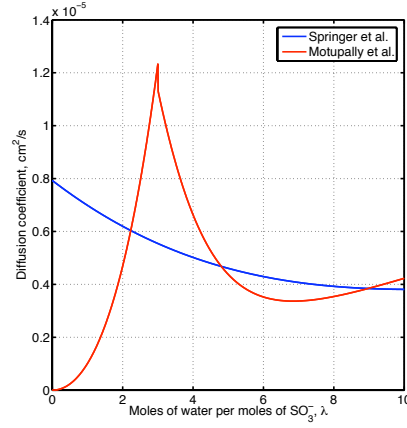


Figure 2.7: Diffusion coefficient for different membrane water content at 80°C.

gas. Motupally et al. suggest the following diffusion coefficients [127]

$$D_{\lambda} = \begin{cases} 3.10 \times 10^{-3} \lambda (-1 + \exp(0.28\lambda)) \exp\left(\frac{-2436}{T_{cell}}\right) & \text{for } 0 < \lambda \leq 3 \\ 4.17 \times 10^{-4} \lambda (1 + 161 \exp(-\lambda)) \exp\left(\frac{-2436}{T_{cell}}\right) & \text{for } 3 < \lambda < 17 \end{cases} \quad (2.97)$$

Figure 2.7 shows the value of the diffusion coefficient at different membrane water content for a cell temperature of 80°C. This figure highlights the main differences between equations (2.94) and (2.97). The largest errors occur at medium water contents, i.e. at about 50%RH. In this thesis, equation (2.95) is used to compute the diffusion coefficient unless stated otherwise.

Finally, since water is neither produced nor consumed inside the membrane, a water mass balance in the membrane leads to the following governing equation,

$$\nabla \cdot \mathbf{N}_w = \nabla(N_{w,drag} + N_{w,diffusion}) = 0 \quad (2.98)$$

Using equations (2.88) and (2.94) in the mass balance equation above, the gov-

erning equation for water transport inside the membrane is obtained

$$\nabla \cdot \left[ -n_d \frac{\sigma_m}{F} \nabla \phi_m - \frac{\rho_{dry}}{EW} D_\lambda \nabla \lambda \right] = 0 \quad (2.99)$$

where  $n_d$  is the electro-osmotic drag coefficient,  $\sigma_m$  and  $\phi_m$  are the membrane conductivity and potential respectively,  $F$  is Faraday's constant,  $\rho_{dry}$  and  $EW$  are the membrane density in its dry state and its equivalent weight,  $D_\lambda$  is the water diffusion coefficient.

The other species that is transported through the membrane are the protons. Assuming that the only transport mechanism for proton motion is a potential gradient, proton transport inside the membrane is given by Ohm's law

$$\mathbf{N}_{H^+} = \frac{\mathbf{i}}{F} = \frac{\sigma_m}{F} \nabla \phi_m \quad (2.100)$$

where  $\sigma_m$  is given by equation (2.92) and  $\phi_m$  is the membrane potential. Finally, since protons are neither produced nor consumed inside the membrane

$$\nabla \cdot \mathbf{N}_{H^+} = \frac{1}{F} \nabla \cdot \mathbf{i} = \nabla \cdot \mathbf{i} = 0 \quad (2.101)$$

and substituting equation (2.100) into the previous equation the governing equation for the proton transport is

$$\nabla \cdot [\sigma_m \nabla \phi_m] = 0 \quad (2.102)$$

### Coupling of the membrane and the catalyst layer

Water content in the membrane is given by  $\lambda$  as defined in equation (2.89). In the catalyst layer, three types of waters co-exist: water vapor in the wet-proofed pores in the CL, liquid water in the CL and sorbed water in the membrane. These three types of water must be in equilibrium at steady state. The value of  $\lambda$  at equilibrium for any value of liquid and water vapor mole fraction is given by an

empirical relation known as the sorption isotherm [53, 128]. The equilibrium  $\lambda$  value for a liquid equilibrated membrane depends on the water temperature, the membrane type and the pre-treatment, i.e. boiling water (E-form), drying at  $80^\circ\text{C}$  (N-form) or drying at  $105^\circ\text{C}$  (S-form) [128]. In this thesis, it is assumed that water only exist inside the membrane or as water vapour in the pores inside the CL. In the case of a vapour equilibrated membrane, the equilibrium  $\lambda$  is independent of the membrane form and only depends on the equivalent weight (EW) of the membrane, temperature and water vapour mole fraction or water vapour activity [128]. At the temperatures typical of a operating cell, i.e. at 353K, Hinatsu et al. [128] obtained the following relationship between water activity and water sorbed in the membrane,

$$\lambda = 0.3 + 10.8a_w - 16a_w^2 + 14.1a_w^3 \quad \text{for } a_w > 0.05 \quad (2.103)$$

where  $a_w$  is the water activity and is given by

$$a_w = \frac{p_{H_2O}}{p_{sat}(T_{cell})}, \quad (2.104)$$

where  $p_{H_2O} = p_{tot}x_w$  is the partial pressure of water vapor at the membrane—gas interface,  $T_{cell}$  is the cell temperature in degrees Celsius and  $p_{sat}(T)$  is given by [54]

$$\log_{10}(p_{sat}(T_{cell})) = -2.1794 + 0.02953T_{cell} - 9.1837 \times 10^{-5}T_{cell}^{2.0} + 1.4454 \times 10^{-7}T_{cell}^{3.0} \quad (2.105)$$

Figure 2.8 illustrates the shape of the sorption isotherm. At low water activity, the amount of water in the membrane is low. Then, as the water activity increases, membrane water content also increases slowly up to water activity values of around 0.75. At high water activities, the membrane water content raises rapidly up to a value of 9.2 for a water activity of 1. Membrane water content at high temperatures are much lower than water uptakes reported at lower temperatures, i.e.  $\lambda = 12$  at  $30^\circ\text{C}$  [54]. These values are in agreement with theoretical studies based on the

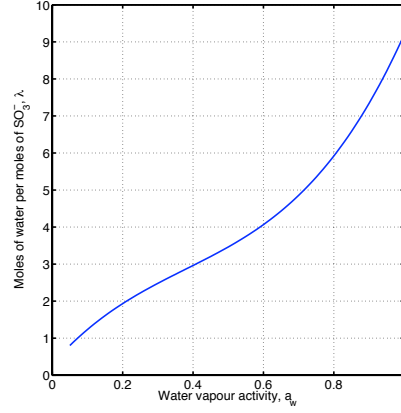


Figure 2.8: Sorption isotherm for water uptake from water vapour by Nafion<sup>TM</sup>, Aciplex<sup>TM</sup> or Flemion<sup>TM</sup> membranes with similar EW of any form at 80°C.

equilibrium of electrochemical potentials [53].

During steady state operation of the catalyst layer, the water vapour molar fraction and the amount of water in the membrane should be in equilibrium; therefore, a coupling term needs to be introduced to the equations that describe water vapour and membrane water content transport. This term will guarantee that the membrane water content and the water vapour are in equilibrium: it will guarantee that equation (2.103) is satisfied everywhere in the catalyst layer. In order to do so, the following source term is added to the membrane and water vapour transport equations

$$S_\lambda = k \frac{\rho_{dry}}{EW} (\lambda_{eq} - \lambda) \quad \text{in CL} \quad (2.106)$$

where  $k$  is a time constant and the term  $\frac{\rho_{dry}}{EW}$  is used in order to yield the same units as the other terms in the equation.  $\lambda$  is in terms of number of moles of water per mole of sulfuric acid heads, the term  $k \frac{\rho_{dry}}{EW}$  transforms these units into moles of  $\text{H}_2\text{O} \cdot \text{cm}^{-3} \cdot \text{s}^{-1}$  in accordance with the other terms in the equations. Finally, the term  $\lambda_{eq} - \lambda$  where  $\lambda_{eq}$  is given by equation (2.103) provides the driving force for  $\lambda$ . If the water vapor

mole fraction is too high, then  $\lambda_{eq}$  will be larger than  $\lambda$  and  $S_\lambda$  will be positive. If  $S_\lambda$  is a source term for the water vapor transport equation, this is equivalent to a water sink (Note: Due to the negative sign of Fick's law, a positive source term is a sink and a negative source term is a source). This represents the water that is sorbed by the membrane in order to achieve equilibrium. On the other hand, if there is a lack of water vapor, then,  $\lambda_{eq} < \lambda$  and  $S_\lambda$  becomes a water source, modeling the release of water by the membrane.

Taking into account the water transport and proton transport equations in the previous sections, as well as the coupling function, the membrane, gas diffusion and catalyst layer governing equations can be written, for the case of the Springer et al. model, as

$$\left. \begin{aligned} \nabla \cdot (c_g D_{O_2}^{eff} \nabla x_{O_2}) &= S_{O_2} \\ \nabla \cdot (c_g D_w^{eff} \nabla x_w) &= S_w + S_\lambda \\ \nabla \cdot (\sigma_m^{eff} \nabla \phi_m) &= S_{H^+} \\ \nabla \cdot (\sigma_S^{eff} \nabla \phi_S) &= S_{e^-} \\ \nabla \cdot (n_d \frac{\sigma_m}{F} \nabla \phi_m + \frac{\rho_{dry}}{EW} D_\lambda \nabla \lambda) &= -S_\lambda \end{aligned} \right\} \quad (2.107)$$

where the effective parameters are different in the membrane, GDL and CL and the source term is

$$S_{O_2} = \begin{cases} 0 & \text{in GDL and membrane} \\ \frac{1}{4F} \nabla \cdot \mathbf{i} & \text{in CL} \end{cases} \quad (2.108)$$

$$S_w = \begin{cases} 0 & \text{in GDL and membrane} \\ -\frac{1}{2F} \nabla \cdot \mathbf{i} & \text{in CL} \end{cases} \quad (2.109)$$

$$S_{H^+} = \begin{cases} 0 & \text{in GDL and membrane} \\ \nabla \cdot \mathbf{i} & \text{in CL} \end{cases} \quad (2.110)$$

$$S_{e^-} = \begin{cases} 0 & \text{in GDL and membrane} \\ -\nabla \cdot \mathbf{i} & \text{in CL} \end{cases} \quad (2.111)$$

and, finally

$$S_\lambda = \begin{cases} 0 & \text{in GDL and membrane} \\ k \frac{\rho_{dry}}{EW} (\lambda_{eq} - \lambda) & \text{in CL} \end{cases} \quad (2.112)$$

where  $k$  is a time constant and  $\lambda_{eq}$  is given by equation (2.103). The source term  $S_\lambda$  couples the water vapor activity to the membrane water content. The value of the time constant  $k$  is of extreme importance in order to guarantee the coupling. For  $k < 10^{-2}$ , the coupling source term,  $S_\lambda$  becomes negligible compared to the reaction rate source term,  $S_w$ , and the coupling of the water vapor and the membrane water content is very weak. Several authors have suggested that the transfer of water from the vapor phase to the membrane is in the order of 100-1000s [129,130]. In this thesis, the constant  $k$  is set to 10000 in order to guarantee the coupling between the CL and the membrane.

### 2.2.2 Numerical solution

In this case, the governing equations for oxygen, water vapor and electron transport remain the same. However, for the sorbed water and proton transport equations, the coefficients of the governing equation are nonlinear; therefore, the assumption made in order to obtain equation (2.70) in the previous section is no longer valid. In this case, the governing equations need to be written in the following form

$$\nabla \cdot (\mathbf{A}_i(\mathbf{u}) \nabla u_i) = f(\mathbf{u}) \quad (2.113)$$

where  $\mathbf{A}_i$  is a matrix of coefficients that provides the effective transport values for each unknown,  $i$ , of the equation and  $f(\mathbf{u})$  is a nonlinear source term that could depend on all unknowns of the system of equation as in the previous case. Notice that due to the isotropic properties of the membrane,  $\mathbf{A}_i$  can be replaced by  $a_i$ , a scalar coefficient. This replacement is applicable to the transport of water inside the

membrane. For example, for the water transport

$$\mathbf{a}_{\phi_m}(\mathbf{u}) = \mathbf{a}_3(\mathbf{u}) = n_d \frac{\sigma_m}{F} \quad (2.114)$$

$$\mathbf{a}_\lambda(\mathbf{u}) = \mathbf{a}_5(\mathbf{u}) = \frac{\rho_{dry}}{EW} D_\lambda \quad (2.115)$$

$$f(\mathbf{u}) = \begin{cases} 0 & \text{in the GDL and membrane} \\ S_\lambda & \text{in the CL} \end{cases} \quad (2.116)$$

$$\mathbf{u} = \begin{pmatrix} x_{O_2} \\ x_w \\ \phi_m \\ \phi_S \\ \lambda \end{pmatrix} \quad (2.117)$$

To solve this equation, we follow the same process outlined in section 2.1.2; however, in this case, the term  $\frac{\partial \mathbf{A}}{\partial u_k}$  from the linearization of equation (2.113) does not vanish and an extra term appears in the equations. Furthermore, in the previous cases, the only coupling between equations was due to the source term. In this case, the right hand side contains additional couplings due to the existence of several unknowns inside the equation. Nevertheless, the linearization and discretization process is similar to the one described in section 2.1.2 and therefore, it is not repeated here.

## 2.3 Anode electrode modeling

### 2.3.1 Governing equations

In a proton exchange membrane fuel cell, the anode reaction is described by the hydrogen oxidation reaction (HOR)



The electrochemical reaction can be described either by a Butler-Volmer equation [32, 131] or by the dual-path reaction [132]. Notice that Tafel's equation cannot be used due to the fast kinetics of the HOR. To describe the transport of hydrogen inside the electrode, the same models are used as those for the cathode.

#### Governing equations for the pseudo-homogeneous model

Under the same assumptions and using a similar approach to the cathode electrode model in section 2.1, the anode GDL and CL are governed by the following set of equations

$$\left. \begin{aligned} \nabla \cdot (c_g D_{H_2}^{eff} \nabla x_{H_2}) &= S_{H_2} \\ \nabla \cdot (\sigma_m^{eff} \nabla \phi_m) &= S_{H^+} \\ \nabla \cdot (\sigma_S^{eff} \nabla \phi_S) &= S_{e^-} \end{aligned} \right\} \quad (2.119)$$

where the effective parameters are different in the GDL and CL and are obtained as described in section 2.1 and the source term is

$$S_{H_2} = \begin{cases} 0 & \text{in GDL} \\ \frac{1}{2F} \nabla \cdot \mathbf{i} & \text{in CL} \end{cases} \quad (2.120)$$

$$S_{H^+} = \begin{cases} 0 & \text{in GDL} \\ -\nabla \cdot \mathbf{i} & \text{in CL} \end{cases} \quad (2.121)$$

$$S_{e^-} = \begin{cases} 0 & \text{in GDL} \\ \nabla \cdot \mathbf{i} & \text{in CL} \end{cases} \quad (2.122)$$

where in  $S_{H_2}$  the number two in the denominator occurs because two electrons are produced per hydrogen molecule consumed.

The anode mixture is a binary one. Therefore, having assumed that the electrode mixture is at constant pressure and that convective transport is negligible [23, 54, 126, 130, 133–137], the species transport can be modeled using Fick's law without the necessary assumptions used the cathode, see equation (2.21). Once the mole fraction of one of the two species is known, the mole fraction of the other specie needs to be obtained using

$$x_{H_2O} + x_{H_2} = 1 \quad (2.123)$$

to guarantee mole conservation of the mixture.

In this model, the Butler-Volmer equation is used to model the hydrogen reaction

$$\nabla \cdot \mathbf{i} = A_v i_0^{ref} \left( \frac{c_{H_2,g|l}}{c_{H_2}^{ref}} \right)^\gamma \left[ \exp \left( \frac{\alpha_a F}{RT} (\phi_S - \phi_m) \right) - \exp \left( -\frac{\alpha_c F}{RT} (\phi_S - \phi_m) \right) \right] \quad (2.124)$$

where the specific reaction surface area per volume of catalyst layer,  $A_v$ , is computed using the expressions in equations (2.36) and (2.37). The electrochemical data is obtained from the literature and is described in the following sections. The hydrogen concentration at the surface of the infinitesimally thin film of electrolyte surrounding the catalyst,  $c_{H_2,g|l}$ , is given by

$$c_{H_2,g|l} = \frac{c_{total} x_{H_2}}{\hat{H}_{H_2,N}} \quad (2.125)$$

and the dimensionless Henry's law constant is obtained using

$$\hat{H}_{H_2,N} = \frac{H_{H_2,N} 10^{-6}}{RT} \quad (2.126)$$

In the latter equation,  $\hat{H}_{H_2,N}$  is taken to be  $6.94 \times 10^{10} \frac{\text{Pa}\cdot\text{cm}^3}{\text{mol}}$  [100]. This value is taken as a constant in this work, but it is reported to change with cell temperature and membrane hydration [138–143]. However, the data in the literature is scattered. For example, Henry’s law values for hydrogen in Nafion<sup>TM</sup> in reference [143] is more than one order of magnitude smaller than the values reported by Gode et al. [142]. Also, some research, such as that of Broka et al. [138], only obtained gas permeation properties instead of diffusion and solubility. Finally, some of the experiments have only been performed at one temperature or relative humidity. Due to the lack of a consistent expression for the hydrogen Henry constant and diffusivity, a constant value is used in this thesis.

### Governing equations for the agglomerate model

Under the same assumptions and using a similar approach to the cathode agglomerate electrode model in section 2.1, the anode agglomerate governing equations are the same as those in equation (2.119).

As in the cathode electrode, the main differences between the pseudo-homogenous model and the agglomerate model are its effective transport properties and the source term. The effective transport properties in the anode are obtained as discussed in the cathode agglomerate model in section 2.1 with appropriate values for hydrogen diffusivity. The source term is obtained using

$$\nabla \cdot \mathbf{i} = 2F \frac{p_{tot} x_{H_2}}{H_{H_2,N}} \left( \frac{1}{E_r k_c (1 - \epsilon_V^{cl})} + \frac{(r_{agg} + \delta_{agg}) \delta_{agg}}{a_{agg} r_{agg} D_{H_2,N}} \right)^{-1} \quad (2.127)$$

where the effectiveness factor and all the agglomerate parameters are computed similarly to the cathode case and the physical parameters such as diffusivity and Henry’s law are input data. The reaction rate,  $k_c$ , is obtained using either the Butler-Volmer equation (2.124) or the dual-pathway kinetic equations. They are both implemented into the program. Unless otherwise stated, in this thesis, the dual-pathway kinetics

are used to describe the hydrogen oxidation reaction (HOR) kinetics [132]. Using the dual-pathway kinetics the reaction rate is given by

$$k_c = \frac{A_v}{2F(1 - \epsilon_V)c_{H_2}^{ref}} \left[ j_{OT} \left( 1 - \exp \left( -\frac{2F}{\gamma RT} \eta \right) \right) + j_{OH} \left( \exp \left( \frac{F}{2RT} \eta \right) - \exp \left( -\frac{F}{\gamma RT} \eta \right) \exp \left( -\frac{F}{2RT} \eta \right) \right) \right] \quad (2.128)$$

where  $j_{OT} = 0.47 A/cm^2$ ,  $j_{OH} = 0.01 A/cm^2$ ,  $\gamma = 1.2$  and  $c_{H_2}^{ref} = 0.59 \times 10^{-6} mol/cm^3$  [100] OR  $c_{H_2}^{ref} = 0.4089 \times 10^{-4} mol/cm^3$  [132] for  $p_{H_2} = 1 atm$  and  $T = 25^\circ C$

## 2.4 Membrane electrode assembly (MEA) modeling

### 2.4.1 Governing equations

The governing equations for the complete MEA are obtained by combining the last set of equations to obtain

$$\left. \begin{aligned} \nabla \cdot (c_g D_{O_2}^{eff} \nabla x_{O_2}) &= S_{O_2} \\ \nabla \cdot (c_g D_w^{eff} \nabla x_w) &= S_w + S_\lambda \\ \nabla \cdot (\sigma_m^{eff} \nabla \phi_m) &= S_{H^+} \\ \nabla \cdot (\sigma_S^{eff} \nabla \phi_S) &= S_{e^-} \\ \nabla \cdot \left( n_d \frac{\sigma_m}{F} \nabla \phi_m + \frac{\rho_{dry}}{EW} D_\lambda \nabla \lambda \right) &= -S_\lambda \end{aligned} \right\} \quad (2.129)$$

where the effective parameters are different in the membrane, GDL and CL. Due to the solution methodology, all equations need to be solved in all the domains, i.e. GDL, CL and membrane. However, some equations are not necessary in some of the cell domains. This is addressed by making the transport parameters almost zero. In order to account for the impermeability of the membrane to water and oxygen

transport, the diffusion coefficient of the membrane to water and oxygen are set to  $10^{-10}$  and  $10^{-7}$ , respectively. The smaller value for oxygen is used because a larger value did not affect the solution and made the algorithm converge quickly. The anode diffusion coefficient to oxygen was also set to  $10^{-7}$ , because oxygen is not expected to be in the anode. To prevent proton transport into both anode and cathode GDLs, the proton conductivity in the GDL is set to  $10^{-8}$ . To prevent the transport of electrons through the membrane, the membrane electron conductivity is set to  $10^{-10}$ . Finally, in the GDLs the electro-osmotic drag coefficient is set to zero and the water diffusion in the membrane,  $D_\lambda$  is set to  $10^{-10}$ . It should be noted that even though this method gives appropriate results, a methodology to separate the domains is recommended for future work, because it could reduce the number of degrees of freedom of the system and therefore result in additional computational savings.

The source terms in the system of equations are given by

$$S_{O_2} = \begin{cases} 0 & \text{in anode CL, GDL and membrane} \\ \frac{1}{4F} \nabla \cdot \mathbf{i} & \text{in cathode CL} \end{cases} \quad (2.130)$$

$$S_w = \begin{cases} 0 & \text{in anode CL, GDL and membrane} \\ -\frac{1}{2F} \nabla \cdot \mathbf{i} & \text{in cathode CL} \end{cases} \quad (2.131)$$

$$S_{H^+} = \begin{cases} 0 & \text{in GDL and membrane} \\ \nabla \cdot \mathbf{i} & \text{in cathode CL} \\ -\nabla \cdot \mathbf{i} & \text{in anode CL} \end{cases} \quad (2.132)$$

$$S_{e^-} = \begin{cases} 0 & \text{in GDL and membrane} \\ -\nabla \cdot \mathbf{i} & \text{in cathode CL} \\ \nabla \cdot \mathbf{i} & \text{in anode CL} \end{cases} \quad (2.133)$$

and

$$S_\lambda = \begin{cases} 0 & \text{in GDL and membrane} \\ k_{EW}^{\rho_{dry}} (\lambda_{eq} - \lambda) & \text{in both CLs} \end{cases} \quad (2.134)$$

Finally, note that the transport equation for the hydrogen mole fraction in equation (2.119) is not included in the system of equations. This is because the anode contains a binary mixture. Since water transport is modeled in both anode and cathode, the hydrogen mole fraction is obtained in the anode electrode using

$$x_{H_2} = 1 - x_w \quad (2.135)$$

This guarantees that the sum of the mole fractions is unity and removes an additional equation from the system thereby increasing computational efficiency.

## 2.4.2 Computational domain and boundary conditions

The two-dimensional cross-section representation of the membrane electrode assembly should include both CLs and GDLs, and the membrane with appropriate boundary conditions for the gas channel-GDL and current collector-GDL interfaces. It is assumed here that the solution is continuous on the interfaces between layers. Taking advantage of geometric symmetry, the computational domain includes only half of the gas channel and half of the current collector, as shown in Figure 2.9. There are five types of boundaries

- Anode current collector at  $(x, y) = \{x = 0, y = [0, \frac{W_{cc}}{2}]\}$ .
- Anode gas channel at  $(x, y) = \{x = 0, y = [\frac{W_{cc}}{2}, \frac{W_{cc}}{2} + \frac{W_{ch}}{2}]\}$ .
- Symmetric boundaries at  $(x, y) = \{\forall x, y = 0 \text{ and } \frac{W_{cc}}{2} + \frac{W_{ch}}{2}\}$ .
- Cathode current collector at  $(x, y) = \{x = L_a^{gdl} + L_a^{cl} + L^m + L_c^{cl} + L_c^{gdl}, y = [0, \frac{W_{cc}}{2}]\}$ .
- Cathode gas channel at  $(x, y) = \{x = L_a^{gdl} + L_a^{cl} + L^m + L_c^{cl} + L_c^{gdl}, y = [\frac{W_{cc}}{2}, \frac{W_{cc}}{2} + \frac{W_{ch}}{2}]\}$ .

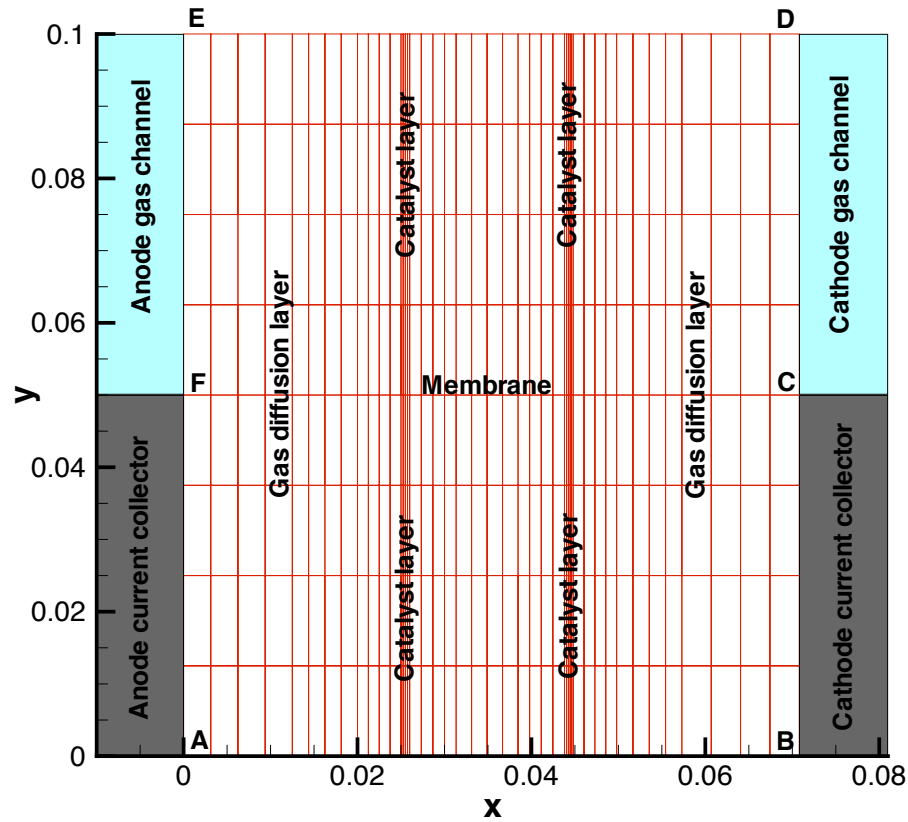


Figure 2.9: Computational domain and initial grid used to solve the equations of the MEA model

where  $L_a^{gdl}$ ,  $L_a^{cl}$ ,  $L^m$ ,  $L_c^{cl}$ ,  $L_c^{gdl}$  represent the anode GDL and CL, membrane and cathode CL and GDL thicknesses respectively.  $W_{cc}$  and  $W_{ch}$  represent the current collector and channel width.

The boundary conditions at the anode current collector (segment A-F in Figure 2.9) are set to

$$N_{O_2} = \mathbf{n} \cdot (c_{tot} \mathbf{D}^{eff} \nabla x_{o_2}) = 0 \quad (2.136)$$

$$N_w = \mathbf{n} \cdot (c_{tot} \mathbf{D}^{eff} \nabla x_w) = 0 \quad (2.137)$$

$$\phi_S = dV \quad (2.138)$$

$$N_{H^+} = \mathbf{n} \cdot (\sigma_m \nabla \phi_m) = 0 \quad (2.139)$$

$$\mathbf{n} \cdot \nabla \lambda = 0 \quad (2.140)$$

where  $\mathbf{n}$  is the surface normal and  $dV$ , is the potential across the cell.

The boundary conditions at the anode gas channel/electrode interface (segment F-E) are set to

$$N_{O_2} = \mathbf{n} \cdot (c_{tot} \mathbf{D}^{eff} \nabla x_{o_2}) = 0 \quad (2.141)$$

$$x_w = x_{w,a}^0 \quad (2.142)$$

$$N_{e^-} = \mathbf{n} \cdot (\sigma_S \nabla \phi_S) = 0 \quad (2.143)$$

$$N_{H^+} = \mathbf{n} \cdot (\sigma_m \nabla \phi_m) = 0 \quad (2.144)$$

$$\mathbf{n} \cdot \nabla \lambda = 0 \quad (2.145)$$

where the water mole fraction inside the pores at the GDL/gas channel interface is assumed to be equal to that of the mixture inside the gas channel.

The boundary conditions along the symmetry boundaries (segments A-B and D-E in Figure 2.9) are set to

$$N_{O_2} = \mathbf{n} \cdot (c_{tot} \mathbf{D}^{eff} \nabla x_{o_2}) = 0 \quad (2.146)$$

$$N_w = \mathbf{n} \cdot (c_{tot} \mathbf{D}^{eff} \nabla x_w) = 0 \quad (2.147)$$

$$N_{e^-} = \mathbf{n} \cdot (\sigma_S \nabla \phi_S) = 0 \quad (2.148)$$

$$N_{H^+} = \mathbf{n} \cdot (\sigma_m \nabla \phi_m) = 0 \quad (2.149)$$

$$\mathbf{n} \cdot \nabla \lambda = 0 \quad (2.150)$$

The boundary conditions at the cathode current collector/electrode interface (segment B-C) reflect the fact that the cathode is taken as the reference potential and are set to

$$N_{O_2} = \mathbf{n} \cdot (c_{tot} \mathbf{D}^{eff} \nabla x_{o_2}) = 0 \quad (2.151)$$

$$N_w = \mathbf{n} \cdot (c_{tot} \mathbf{D}^{eff} \nabla x_w) = 0 \quad (2.152)$$

$$\phi_S = 0 \quad (2.153)$$

$$N_{H^+} = \mathbf{n} \cdot (\sigma_m \nabla \phi_m) = 0 \quad (2.154)$$

$$\mathbf{n} \cdot \nabla \lambda = 0 \quad (2.155)$$

Finally, the boundary conditions at the cathode gas channel/electrode interface (segment C-D) are set to

$$x_{o_2} = x_{o_2}^0 \quad (2.156)$$

$$x_w = x_{w,c}^0 \quad (2.157)$$

$$N_{e^-} = \mathbf{n} \cdot (\sigma_S \nabla \phi_S) = 0 \quad (2.158)$$

$$N_{H^+} = \mathbf{n} \cdot (\sigma_m \nabla \phi_m) = 0 \quad (2.159)$$

$$\mathbf{n} \cdot \nabla \lambda = 0 \quad (2.160)$$

where the oxygen concentration inside the pores at the GDL/gas channel interface is taken as equal to the concentration of oxygen in the mixture inside the gas channel.

### 2.4.3 Input parameters

The input parameters to the membrane electrode assembly model are specified in Tables 2.2, 2.3, 2.4 and 2.5 for the operating conditions and geometry, anode electrode, membrane and cathode electrode respectively. The data presented here is obtained from the literature and the source of the data is specified next to the value. Furthermore, if no reference is given, the values were obtained as described in the previous sections by curve fitting to experiments.

The geometrical values in Table 2.2 are standard values for GDL and CL. The thickness of the membrane are given according to type of membrane. For Nafion<sup>TM</sup> membranes, the first two digits refer to the equivalent weight and the last one or two digits refer to the thickness of the membrane in mils or "milli-inches". For example, a Nafion<sup>TM</sup> 117 membrane has an equivalent weight of 1100 *g/mol* and a thickness of 7mils, i.e. 178 $\mu$ m. In this case, a Nafion<sup>TM</sup> 1135 membrane is used. The operating conditions are the same as for Bender et al. [144]. These operating conditions have been chosen in order to be able to readily validate the computational model with the results in [144] in section 2.5.2. Note that the relative humidity (RH) is chosen to be 75% because authors do not report RH, and only acknowledge that humidification levels are below 100%RH.

The physical, structural and electrochemical parameters for the anode electrode are given in Table 2.3. Again, these values are obtained from the literature. The diffusion coefficients and Henry's law constant are reported for the given operating conditions. When the operating conditions change, these values are computed for the new conditions. The values for conductivities are obtained as described in section 2.1. The structural parameters are given by the MEA information provided in reference

Table 2.2: Membrane electrode assembly geometry and operating conditions

<i>Geometry</i>	
Anode GDL thickness, $L_a^{gdl}$ , [cm]	$2.5 \times 10^{-2}$ , [15]
Anode CL thickness, $L_a^{cl}$ , [cm]	$1.0 \times 10^{-3}$ , [15]
Membrane thickness, $L^m$ , [cm]	$0.89 \times 10^{-2}$ , Nafion <sup>TM</sup> 1135
Cathode CL thickness, $L_c^{cl}$ , [cm]	$1.0 \times 10^{-3}$ , [15]
Cathode GDL thickness, $L_c^{gdl}$ , [cm]	$2.5 \times 10^{-2}$ , [15]
Channel width, [cm]	0.1, [15]
Current collector width, [cm]	0.1, [15]
<i>Cell operating conditions</i>	
$T$ [K]	353, [15]
<i>Anode operating conditions</i>	
$p$ , [atm]	3, [15]
$x_{H_2}$	0.88326 (75%RH)
$x_w$	0.11674 (75%RH)
<i>Cathode operating conditions</i>	
$p$ , [atm]	3, [15]
$x_{O_2}$	0.18549 (75%RH)
$x_{N_2}$	0.69777 (75%RH)
$x_w$	0.11674 (75%RH)

[144] or are obtained from other sources. Finally, the amount of electrolyte inside the agglomerate is used to obtain a reasonable volume fraction of each material in the CL and also as a fitting parameter. The structural parameters in Table 2.3 result in solid phase, electrolyte and porosity values of 0.409, 0.384 and 0.207 respectively. There is great uncertainty regarding the agglomerate radius and thin film surrounding the agglomerate. Experimental studies and TEM and SEM images suggest values ranging from 0.1 to 3  $\mu m$  and 0 to 80  $nm$  respectively [42, 43, 45, 46, 145]. In this case, values of 1 $\mu m$  and 80 $nm$  are used since they are inside the range of values reported in the literature and they provide a good fit to the experimental polarization curve in reference [144]. The two sets of electrochemical data are for the pseudo-homogeneous model using the Butler-Volmer equation, and for the agglomerate model using the recently published [132] dual-path kinetics.

The membrane properties are given in Table 2.4. Of these parameters, the constant  $k$  is the most important and it is used to couple the membrane water content to the water content in the catalyst layer. A large value is needed for this constant in order to guarantee that the sorption isotherm is followed closely.

The physical, structural and electrochemical parameters for the cathode electrode are given in Table 2.5. The diffusion coefficients are obtained either from other references or computed using the Chapman-Enskog theory at the given operating conditions. The structural parameters have been chosen to be the same as the anode electrode parameters because in most MEAs, both electrodes have the same structure. The electrochemical data is obtained from the data reported by Parthasarathy et al. [96, 97]. The kinetics for the oxygen reduction reaction reported in that article are divided between two regimes at high and low voltages. However, Neyerlin et al. suggest that the second regime was due to mass transport limitations [148]. Therefore, in this thesis, low voltage kinetics are used. For the low oxygen kinetics, Parthasarathy et al. suggest that the oxygen reaction is first order and the current

Table 2.3: Anode gas diffusion layer and catalyst layer physical and electrochemical properties

<i>Constants</i>	
$\rho_{Pt}$ , [ $g \cdot cm^{-3}$ ]	21.5, [20]
$\rho_c$ , [ $g \cdot cm^{-3}$ ]	2.0, [20]
$\rho_N$ , [ $g \cdot cm^{-3}$ ]	2.0, [20]
<i>Anode GDL and CL physical properties</i>	
$D_{H_2,w}$ , [ $cm^2 \cdot s^{-1}$ ]	0.34952, [146]
$H_{H_2,N}$ , [ $\frac{Pa \cdot cm^3}{mol}$ ]	$6.69 \times 10^{10}$ , [100]
$D_{H_2,N}$ , [ $cm^2 \cdot s^{-1}$ ]	$12.8 \times 10^{-6}$ , [100]
$\sigma_{S,XX}^{gdl}$ , [ $S \cdot cm^{-1}$ ]	16.03
$\sigma_{S,YY}^{gdl}$ , [ $S \cdot cm^{-1}$ ]	272.78
$\sigma_S^cl$ , [ $S \cdot cm^{-1}$ ]	88.84
<i>Anode GDL and CL structural properties</i>	
$\epsilon_V^{gdl}$	0.6
$m_{Pt}$ , [ $mg/cm^2$ ]	0.2, [144]
$Pt C$ , [-]	0.2, [144]
$r_{agg}$ , [ $\mu m$ ]	1.0, [15]
$\epsilon_{agg}$ , [-]	0.35, this work
$\delta_{agg}$ , [ $nm$ ]	80, [15]
<i>Anode CL electrochemical properties - Dual path kinetics, eq. (2.128)</i>	
$j_{OT}$ , [ $A \cdot cm^{-2}$ ]	0.47, [132]
$j_{OH}$ , [ $A \cdot cm^{-2}$ ]	0.01, [132]
$\gamma$ , [-]	1.2, [132]
$c_{H_2}^{ref}$ , [ $mol/cm^3$ ]	$0.59 \times 10^{-6}$ , [100, 147]
<i>Anode CL electrochemical properties - Butler-Volmer kinetics, eq. (2.124)</i>	
$\alpha_a$ , [-]	0.5, [32]
$\alpha_c$ , [-]	0.5, [32]
$\gamma$ , [-]	0.25, [32]
$c_{H_2}^{ref}$ , [ $mol/cm^3$ ]	$5.64 \times 10^{-5}$ , [32]
$i_0^{ref}$ , [ $A \cdot cm^{-2}$ ]	1 [32]

Table 2.4: Membrane physical and electrochemical properties

<i>Membrane properties</i>	
$EW$ , [g/mol]	1100, [54]
$\rho_{dry}$ , [g/cm <sup>3</sup> ]	2.0, [54]
$k$ , [1/s]	10000, this work

density and pressure are related by

$$\log_{10}(i_0) = \log_{10}(p_{O_2}) - 7.89685 \quad (2.161)$$

at 323K where  $i_0$  is in  $A/cm^2$ ,  $p_{O_2}$  is in *atm* and the value 7.89685 is given by interpolating the data in reference [97] to an oxygen partial pressure of 1atm. Using this equation, the exchange current density for dry air ( $p_{O_2}=0.21$ ) at 323K is  $i_0 = 2.663 \times 10^{-9} A/cm^2$ . Then, using the activation energy for the current density given in reference [96], 73269J/mol, the current density for the ORR at any temperature can be obtained using

$$i_0 = 10^{3.271 - 3826 \frac{1}{T}} \quad (2.162)$$

This expression can be used as the exchange current density with an oxygen reference concentration of  $0.725 \times 10^{-5} mol \cdot cm^{-3}$ . For dry air ( $p_{O_2}=0.21$ ) and 353K,  $i_0 = 2.707 \times 10^{-8} A/cm^2$ .

## 2.5 Validation of the numerical code

In the following section, the computational program developed in the thesis is validated both numerically and experimentally. Both numerical and experimental validations involve the comparison of polarization or I-V curves. Such curves plot the cell potential vs. the current density of the cell. In this thesis, the cell voltage is not specified; instead, a voltage across the MEA,  $dV$ , is used for the boundary conditions

Table 2.5: Cathode gas diffusion layer and catalyst layer physical and electrochemical properties

<i>Constants</i>	
$\rho_{Pt}$ , [ $g \cdot cm^{-3}$ ]	21.5, [20]
$\rho_c$ , [ $g \cdot cm^{-3}$ ]	2.0, [20]
$\rho_N$ , [ $g \cdot cm^{-3}$ ]	2.0, [20]
<i>Cathode GDL and CL physical properties</i>	
$D_{O_2, N_2}$ , [ $cm^2 \cdot s^{-1}$ ]	0.091368, [146]
$D_{w, N_2}$ , [ $cm^2 \cdot s^{-1}$ ]	0.098919, [146]
$H_{O_2, N}$ , [ $\frac{Pa \cdot cm^3}{mol}$ ]	$3.1664 \times 10^{10}$ , [15]
$D_{O_2, N}$ , [ $cm^2 \cdot s^{-1}$ ]	$8.45 \times 10^{-6}$ , [15]
$\sigma_{S, XX}^{gdl}$ , [ $S \cdot cm^{-1}$ ]	16.03
$\sigma_{S, YY}^{gdl}$ , [ $S \cdot cm^{-1}$ ]	272.78
$\sigma_S^{cl}$ , [ $S \cdot cm^{-1}$ ]	88.84
<i>Anode GDL and CL structural properties</i>	
$\epsilon_V^{gdl}$	0.6
$m_{Pt}$ , [ $mg/cm^2$ ]	0.2, [144]
$Pt C$ , [-]	0.2, [144]
$r_{agg}$ , [ $\mu m$ ]	1, [15]
$\epsilon_{agg}$ , [-]	0.35, [15]
$\delta_{agg}$ , [ $nm$ ]	80, [15, 145]
<i>Cathode CL electrochemical properties</i>	
$\alpha$	1, [96, 97, 148]
$n$	4, [15, 96, 97]
$\gamma$	1.0, [15, 96, 97]
$i_0^{ref}$ , [ $A \cdot cm^{-2}$ ]	$2.707 \times 10^{-8}$ , [96, 97]
$c_{O_2}^{ref}$ , [ $mol \cdot cm^{-3}$ ]	$0.725 \times 10^{-5}$ , [96, 97]

(2.151) and (2.136). Given the MEA voltage drop,  $dV$ , the cell potential is

$$V_{cell} = E_{th} - dV \quad (2.163)$$

where  $E_{th}$  is the theoretical cell voltage or potential in Volts and is given by [15]

$$E_{th} = 1.229 - 8.456 \times 10^{-4}(T - 298.15) + 4.31 \times 10^{-5}T(\ln(p_{H_2}) + \frac{1}{2}\ln(p_{O_2})) \quad (2.164)$$

In this case, assuming a pressure and relative humidity at both anode and cathode of 3 atm and 75%, the partial pressures for hydrogen and oxygen are  $p_{H_2} = 2.6498atm$  and  $p_{O_2} = 0.5565atm$ . Therefore,  $E_{th}$  is 1.2123V.

The current density is obtained during post-processing. The cell current density per unit area can be obtained by integrating the volumetric current density over the volume of either the anode or cathode CL,

$$f(\mathbf{u}, \mathbf{p}) = i(x_{o_2}, \phi_S, \phi_m; m_{Pt}, \epsilon_{agg}, Pt|C, \epsilon_V^{gdd}) = \frac{1}{H} \int_0^H \int_0^L \nabla \cdot \mathbf{i} dx dy \quad (2.165)$$

where  $\nabla \cdot \mathbf{i}$  is given in equation (2.33),  $H$  is the height of the domain and  $L$  is the width of the domain, i.e. the thickness of the CL.

### 2.5.1 Grid study

Before any simulations are performed, a grid study is conducted to establish the number of adaptive refinements that produce a grid independent solution. The current density produced by the MEA is used as the indicator of a grid independent solution. When the current density does not change significantly between grid levels, the grid will be assumed to produce solution independent results. Figures 2.10 and 2.11 show a grid study at medium and high current densities. In both cases, the evolution of

the current density is plotted against both a globally (dashed line) and an adaptively (solid line) refined grid. These figures show that after the first global refinement, the current density changes very slightly, i.e. less than 1%; therefore, a grid independent solution can be quickly achieved with approximately 8,000 degrees of freedom (DOF). Figures 2.10 and 2.11 show the advantage of using adaptive refinement. In both cases, the adaptively refined grid converges faster to a grid independent solution. This can be easily observed in Figure 2.11 where the adaptive grid with 28,000 DOFs gives the same solution as the globally refined grid with 115,000 DOFs. The reason for the faster convergence is that the adaptive grid takes into account the physics of the problem by means of an error estimator that indicates where the grid needs to be refined. For the remainder of this thesis, an adaptive grid with approximately 28,000 DOFs will be used.

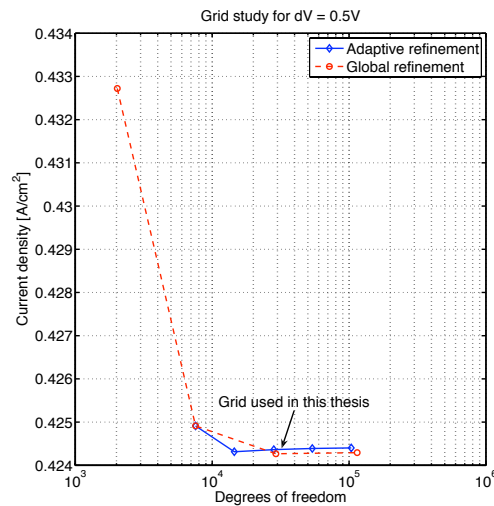


Figure 2.10: Grid study at medium current densities. The solid and dashed lines show the evolution of the current density as the grid is both adaptively and globally refined, respectively.

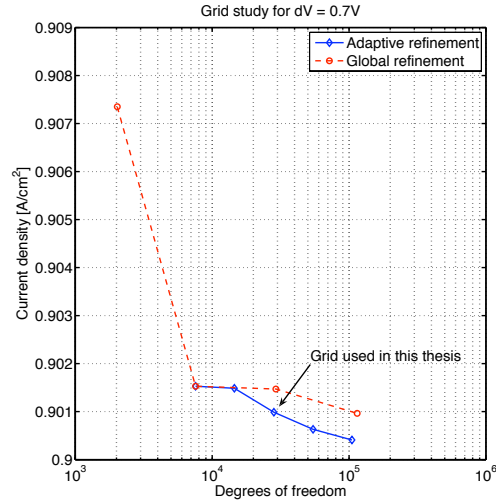


Figure 2.11: Grid study at high current densities. The solid and dashed lines show the evolution of the current density as the grid is both adaptively and globally refined, respectively.

## 2.5.2 Experimental validation

In order to validate the proposed two-dimensional MEA model, polarization curves obtained using the numerical code and obtained from experimental studies are compared using the same input parameters. In this thesis, a two-dimensional through-the-channel model has been developed. As a result, the numerical model does not account for the consumption of reactants as they travel through the gas channel inside the cell and it assumes a constant mole fraction of reactants in the MEA-channel interface. For this reason, only experiments performed at very high stoichiometric values for both oxygen and hydrogen can be used for validation. This means that commonly used data for validation such as the experimental polarization curves obtained at low stoichiometries for a complete cell such as that reported by Lin Wang et al. cannot be used [149, 150]. Because polarization curves at high stoichiometries are seldom published, data from a segmented cell study is used for validation in this thesis. Several research groups have developed segmented cells in the past few years [144, 151–157].

In this thesis, the data from Bender et al. [144] is used to perform the validation of our numerical model, because it provides the most detailed explanation of the MEA used, and also of the experimental set up. Tables 2.2, 2.3, 2.4 and 2.5, provide the input data for the simulations. All the data used for the validation is either from the experimental setup given in reference [144] or other sources as described in section 2.4.3.

Figure 2.12 shows the polarization curve reported by Bender et al. for the first segment of the cell, and the polarization curve obtained from the numerical code. The experimental curve is obtained for the first segment of the cell because it is in this segment alone that the oxygen and water vapour concentrations are known. Regarding water concentration, the humidifier temperature is equal to the cell temperature and therefore, the inlet air should to be fully saturated. However, Bender et al. report that, even in this case, it was observed that the air was not fully humidified. Therefore, polarization curves for 75% and 100% relative humidities are given. It can be observed that the experimental curve falls between the two curves obtained experimentally, demonstrating good agreement between numerical and experimental data in the whole range of operating conditions. Of special importance is the agreement at high current densities, which is only made possible by the use of the agglomerate model. The agglomerate radius used is  $1\mu m$ . This is quite a large radius when compared with those reported by catalyst layer analyses using SEM and TEM imaging, but it is of the same order as those reported by fitting polarization curves to experimental data. This suggests that the agglomerate radius might be used as a numerical tool to account for transport losses due to the structure of the catalyst layer, and that it could be interpreted as the mean path that the oxygen needs to travel inside the electrolyte phase before it can react. This value might not be easy to quantify experimentally.

A more thorough experimental validation of the computational model is not presented here due to the lack of experimental data at high stoichiometric values and

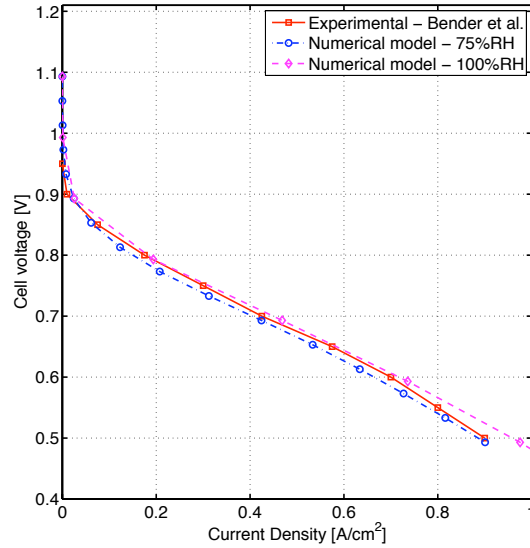


Figure 2.12: Polarization curves from experimental data and numerical data at 75% and 100% RH

for different MEAs. In order to perform a more thorough validation, polarization curves of several fuel cells with different MEAs operating at high stoichiometric values should be obtained and compared to the results from the numerical program. Also, local current distributions should be obtained since it is well known that cells under different regimes can produce similar polarization curves [37].

### 2.5.3 Numerical validation and performance evaluation

The model presented has been developed entirely by the author in C++ using the deal.ii finite element libraries [116]. Therefore, in addition to the previous experimental validation, it is also desirable to validate the code numerically. Such validation serves a dual purpose: a) to guarantee that the developed program is free of any programming errors; and b) to compare its computational speed with respect to another commercial software. In this case, the test case solved above is solved using both

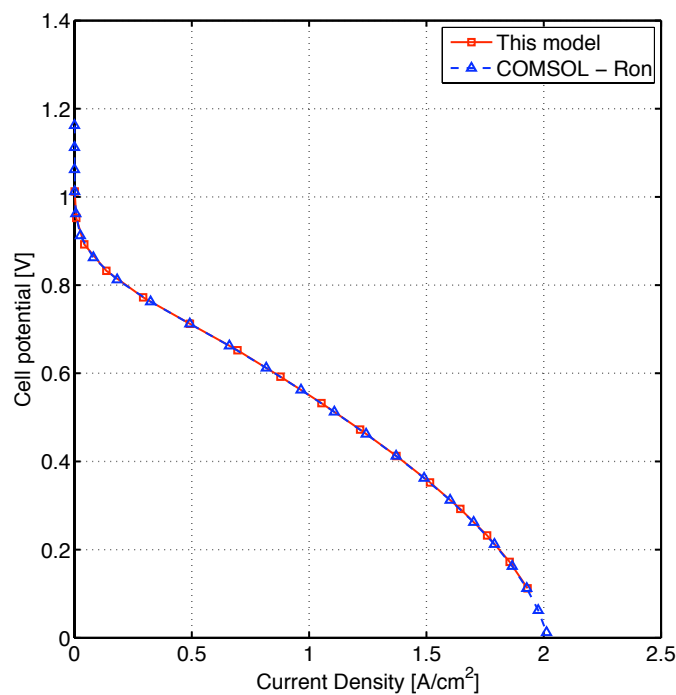


Figure 2.13: Polarization curves obtained with the code developed (FCST) in this thesis and COMSOL

the developed code (FCST) and the commercial code COMSOL [158]. The linear solver used is the same for both programs, namely UMFPACK. The final grid in both cases has approximately 25,000 DOF. The COMSOL model contains the same equations and input parameters as the model presented in this thesis, except that uses a pseudo-homogeneous anode model because the dual-path kinetics model did not converge. In order to validate the results, both codes are run with a pseudo-homogeneous anode model. The COMSOL model was developed by Ron Songprakorp [159]. The polarization curves are shown in Figure 2.13.

Figure 2.13 shows that identical results are achieved using both software programs. In a comparison of computational speed when solving a single point on the polarization curve, COMSOL was approximately 3 to 4 times slower than FCST. Because the

same linear solver was used, this slow-down was most likely caused by a combination of the Newton loop and by the matrix assembly procedure.

## 2.6 Numerical results and parametric studies

In this section, the numerical code developed and validated in previous sections is used to study the transport processes occurring inside the fuel cell and the effects of GDL and CL structure.

### 2.6.1 Transport processes inside the MEA

The transport processes occurring inside the fuel cell are studied in detail here for the base case. In particular, the anode and cathode transport processes and reactions and water transport inside the MEA are investigated for low, medium and high current densities.

#### MEA operation at low current densities

Figures 2.14, 2.15 and 2.16 show the transport processes occurring inside the anode and cathode of the fuel cell and the water transport inside the membrane and CL when a 0.4V voltage is imposed across the MEA. The corresponding current density is  $0.1627A/cm^2$ .

Figure 2.14 shows the hydrogen mole fraction, electrolyte phase water content, overpotential, and volumetric current density in the anode catalyst layer. The hydrogen mole fraction varies only slightly inside the CL, and it is higher than the gas channel mole fraction, 0.8833, in the area under the gas channel, and lower in the area under the current collector. The increase in hydrogen mole fraction in the area under the gas channel may appear counter-intuitive when considering that hydrogen

is being consumed in the CL. However, this phenomenon can readily be explained by examining the water vapor mole fraction or, since they are coupled, the electrolyte water content in Figure 2.14. In the area under the channel, membrane water content, and, therefore, water mole fraction in the anode mixture, is low because water is transported from anode to cathode via electro-osmotic drag. Since the anode mixture is a binary mixture, this reduction in water vapor results in an increase of the hydrogen mole fraction. On the other hand, the water content in the CL is highest under the land area. In this region, water is being transported from cathode to anode by back-diffusion and the water vapor mole fraction increases. As a result, the hydrogen mole fraction has to decrease. Water transport is the dominant transport process in the anode that while only a half mole of hydrogen is necessary in the electrochemical reaction to produce a proton, each proton is able to drag up to one water molecule, as shown in equation (2.91). This means that water is evacuated from the anode very rapidly. This causes that the hydrogen mole fraction increases inside the anode CL (2.135). This suggests that in order to account for the reduction in the hydrogen concentration due to its consumption in the electrochemical reaction, the assumption of a constant concentration of the mixture of hydrogen and water needs to be revisited. However, given that the hydrogen mole fraction changes by less than 2%, even at high current densities, we follow the practice adopted in previous work and neglect convection in the anode [23, 54, 126, 130, 133–137].

Figure 2.14 also shows the overpotential and the volumetric current density generated in the anode. Both volumetric density and overpotential are almost zero in most of the catalyst layer. They then increase near the CL-membrane interface, but even there, the overpotential remains very small given the extremely fast hydrogen kinetics.

Figure 2.15 shows the oxygen mole fraction, electrolyte phase water content, overpotential and volumetric current density in the cathode CL. Oxygen is well distributed throughout the catalyst layer with slightly higher concentrations under the gas chan-

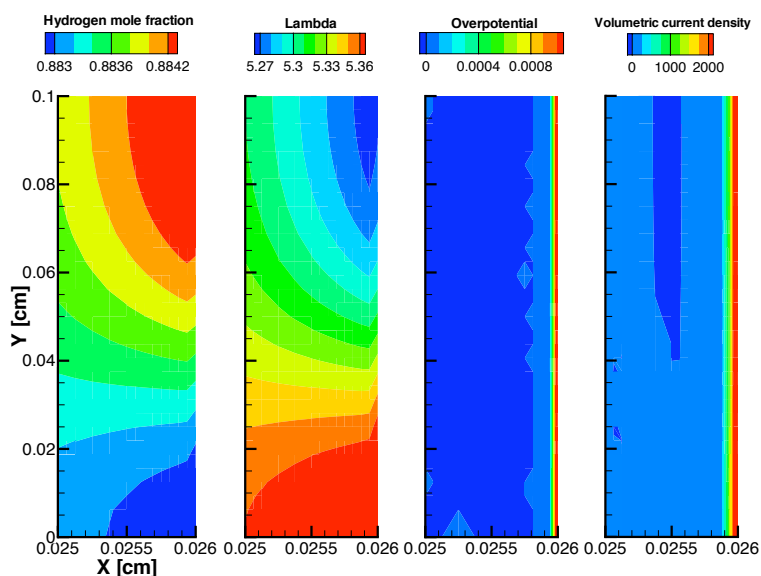


Figure 2.14: Contour plots of the hydrogen mole fraction, electrolyte phase water content, overpotential and volumetric current density in the anode catalyst layer at a voltage across the MEA of 0.4V

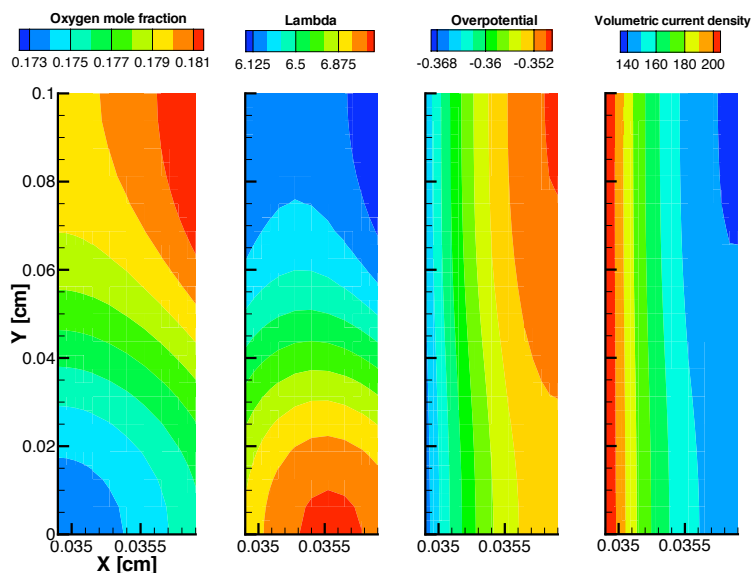


Figure 2.15: Contour plots of the oxygen mole fraction, electrolyte phase water content, overpotential and volumetric current density in the cathode catalyst layer at a voltage across the MEA of 0.4V

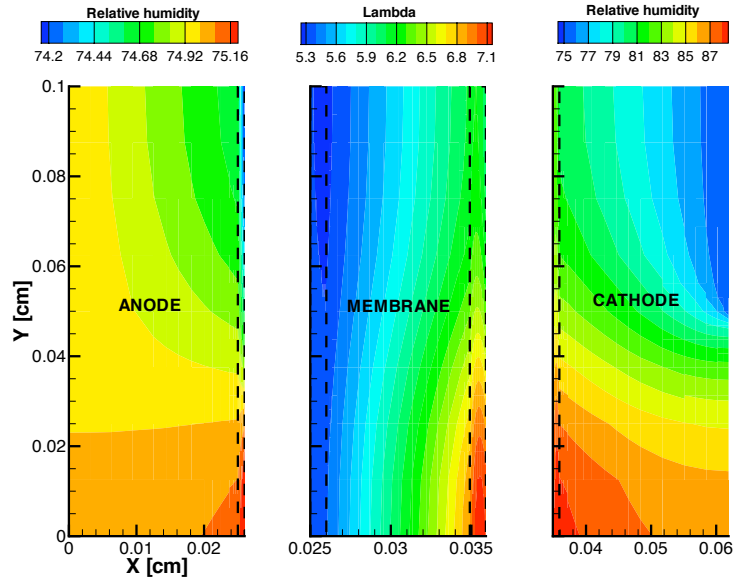


Figure 2.16: Contour plots of the relative humidity in the anode and cathode GDL and CL, and membrane and CL electrolyte water content at a voltage across the MEA of 0.4V

nel at the GDL-CL interface. The electrolyte water content is quite uniform with higher values in the middle of the CL, under the land area. The electrolyte water content distribution highlights the different mechanisms for water transport. Near the membrane, water is diffusing back to the anode due to membrane water content concentration gradients. Near the CL-GDL interface, water is also diffusing toward the gas channel since the water mole fraction in the channel is lower. The net result is that higher water concentrations are observed inside the CL where the water that is produced by the reaction is able to remain. Similarly, water content is higher under the land area because diffusion of water to the gas channels is more difficult. The distribution of the overpotential and volumetric current density is quasi one-dimensional through most of the cathode, with higher values near the CL-membrane interface. The overpotential is of the order of 0.36, i.e. 90% of the voltage drop across the MEA is due to the ORR kinetics.

Finally, Figure 2.16 shows the water transport inside the MEA. In the anode, under the channel water is dragged to the cathode, and under the land, water is transported by back diffusion. The membrane water content,  $\lambda$ , is between 5 and 7, with higher water content on the cathode side. Finally, the cathode relative humidity reaches 88% under the land due to water produced by the ORR.

### MEA operation at medium current densities

Figures 2.17, 2.18 and 2.19 show the transport processes inside the MEA at a voltage across the MEA of 0.6V, i.e. a cell voltage of 0.593V. At this cell voltage, the cell's current density is  $0.6810A/cm^2$ .

Figure 2.17 shows the hydrogen mole fraction, electrolyte phase water content, overpotential and volumetric current density in the anode catalyst layer. The contour plots exhibit similar features to the ones at low current density in Figure 2.14. Again, due to water transport from anode to cathode the hydrogen mole fraction increases with respect to the channel mole fraction; however, this increase is less than 2%. In this case, the hydrogen mole fraction increases everywhere in the CL indicating that water is being removed everywhere in the anode by electro-osmotic drag. The reaction kinetics are again concentrated at the CL-membrane interface.

Figure 2.18 shows the contour plot of the different species in the cathode CL and the ORR. The figure shows that the oxygen mole fraction is significantly reduced at the CL-membrane interface near the land area. This causes the ORR to become less uniform and the reaction under the land area starts to be slightly lower. In Figure 2.15 the volumetric current density contour lines are almost vertical. This is not the case in Figure 2.18, where the contour lines exhibit a more pronounced arching, indicating a reduction of the reaction under the land area. The catalyst layer electrolyte water content is essentially uniform with  $\lambda \approx 9.2$ . This value of  $\lambda$  corresponds to a membrane equilibrated with fully saturated air. The value of 9.2

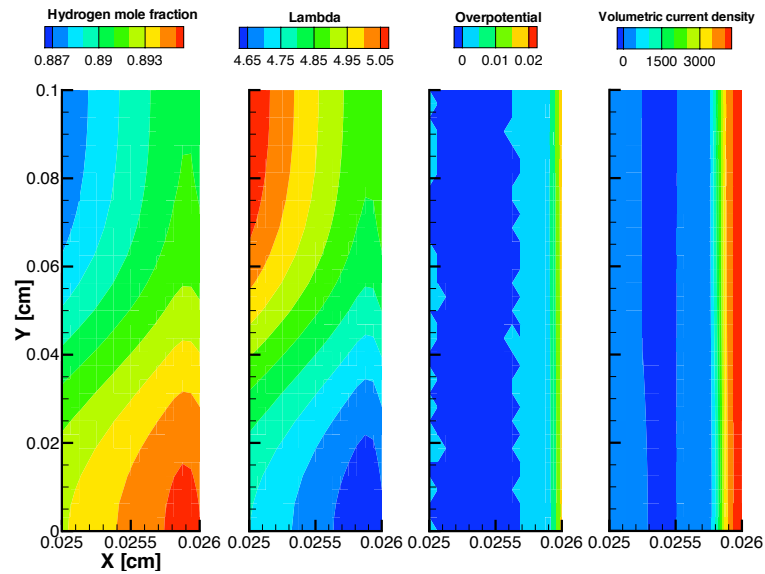


Figure 2.17: Contour plots of the hydrogen mole fraction, electrolyte phase water content, overpotential and volumetric current density in the anode catalyst layer at a voltage across the MEA of 0.6V

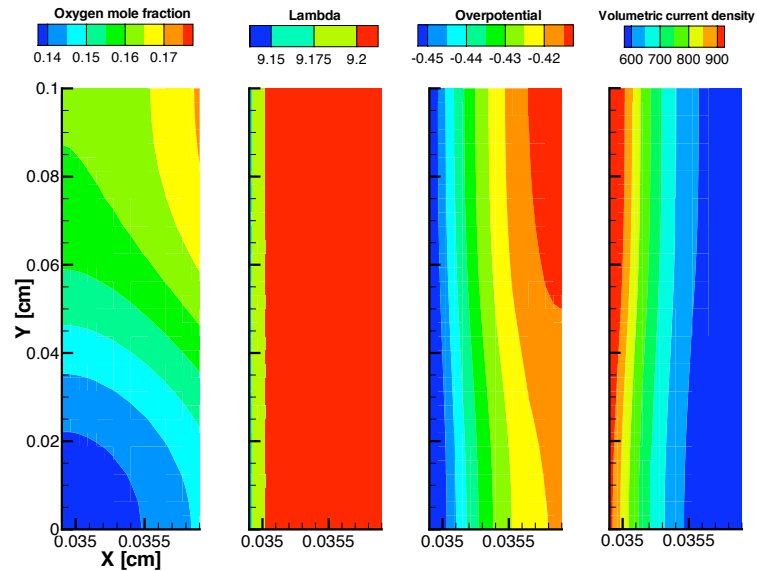


Figure 2.18: Contour plots of the oxygen mole fraction, electrolyte phase water content, overpotential and volumetric current density in the cathode catalyst layer at a voltage across the MEA of 0.6V

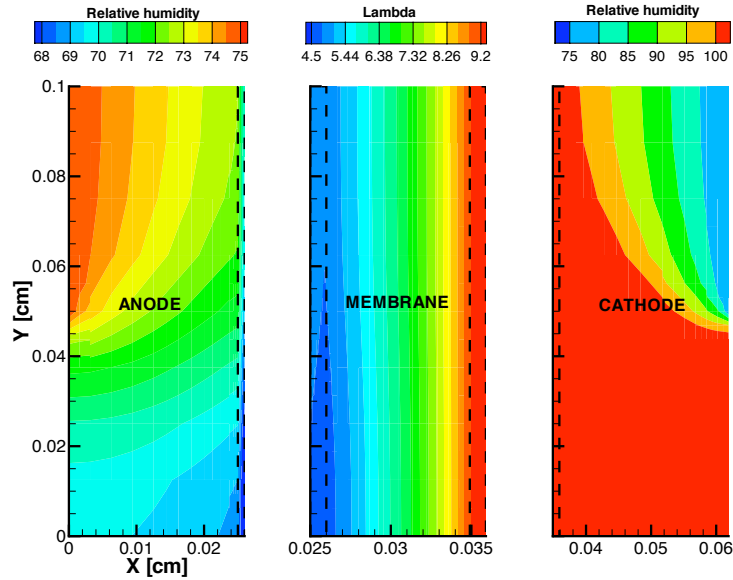


Figure 2.19: Contour plots of the relative humidity in the anode and cathode GDL and CL, and membrane and CL electrolyte water content at a voltage across the MEA of 0.6V

is the maximum allowed because the model is single-phase and therefore, only water vapor is accounted for. Finally, the overpotential in the cathode is in the order of 0.425V, this is less than 75% of the total MEA losses. This shows that ohmic losses in the membrane become proportionally larger with increasing current density.

Water content in the anode GDL and CL, membrane and cathode CL and GDL is shown in Figure 2.19. The relative humidity in the anode GDL and CL is shown in the left figure with the CL represented by the dashed rectangle. The relative humidity in the anode decreases near the membrane. This is due to the dominant effect of the electro-osmotic drag compared to back-diffusion. This can also be observed by examining the membrane water content which varies significantly from anode to cathode reaching a maximum value of 9.2 at the cathode CL. The relative humidity in the cathode is close to 100%, thereby demonstrating that the air in the cathode is fully saturated. Since the model is single-phase, the water condensation that might occur

in the CL and GDL is not accounted for. The results of the model are therefore only valid when saturation of the media by liquid water is small and the effect of liquid water on reactant transport is negligible. This assumption is justified by the results published by You et al. [160] and Berning et al. [34] showing that even at high current densities, e.g.  $1.2 A/cm^2$ , saturation of the porous media is less than 10%. Several recent results disagree with the previous data showing high values of saturation in both CL and GDL [130, 136, 137]. Two-phase water transport is still a very active area of research and new data is necessary in order to understand: a) the phases of the water produced in the cathode; b) the water condensation and evaporation rates; c) the water transport mechanisms in GDL and CL. Two-phase flow is outside the scope of this thesis and will not be discussed further. In this thesis, it is assumed that water is only transported as water vapor. Notice also that this assumption does not affect oxygen concentration because oxygen and water transport are only dependent on their respective gradient in the context of Fick's law.

### **MEA operation at high current densities**

Figures 2.20, 2.21 and 2.22 show the transport processes inside the MEA at a voltage across the MEA of 0.8V, i.e. a cell voltage of 0.393V. The corresponding cell current density is  $1.0962 A/cm^2$ .

Figure 2.20 shows the hydrogen mole fraction, electrolyte phase water content, overpotential and volumetric current density in the anode catalyst layer. The contour plots are similar to the ones at low and medium current densities in Figures 2.14 and 2.17. Comparing the volumetric current density contour plot to those at low and medium current densities, it can be observed that a larger section of the catalyst layer is utilized in this case. Also, the effect of electro-osmotic drag becomes more important as the current density increases. In this case, lambda values of less than 4 are observed under the land area, leading to an increase in ohmic losses in the anode CL.

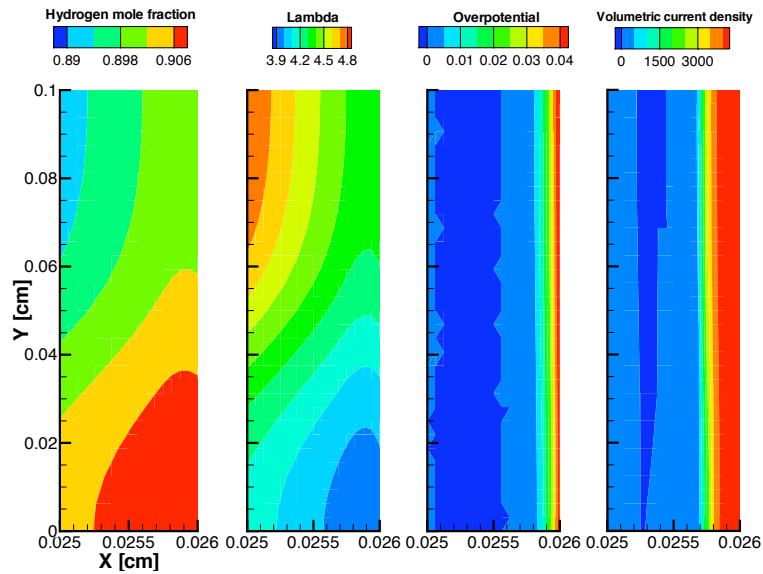


Figure 2.20: Contour plots of the hydrogen mole fraction, electrolyte phase water content, overpotential and volumetric current density in the anode catalyst layer at a voltage across the MEA of 0.8V

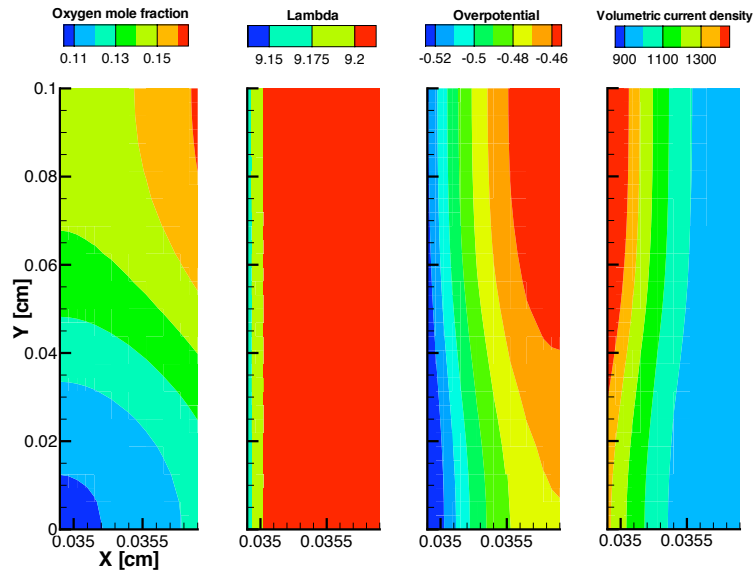


Figure 2.21: Contour plots of the oxygen mole fraction, electrolyte phase water content, overpotential and volumetric current density in the cathode catalyst layer at a voltage across the MEA of 0.8V

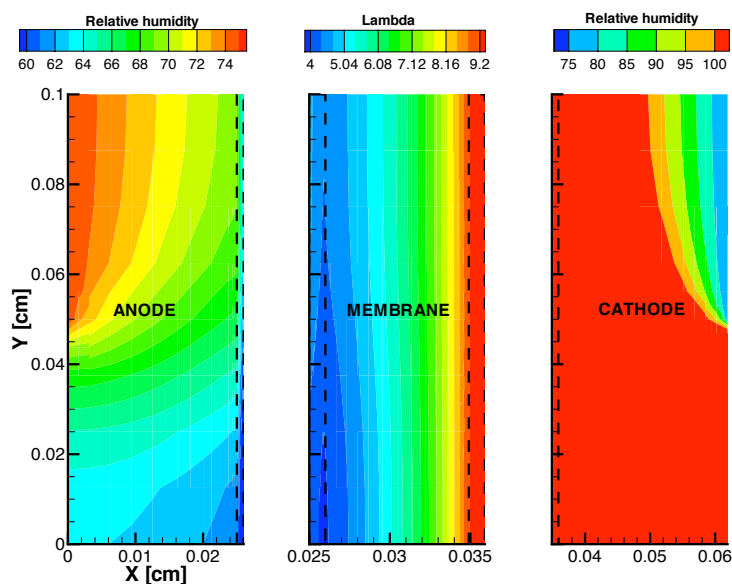


Figure 2.22: Contour plots of the relative humidity in the anode and cathode GDL and CL, and membrane and CL electrolyte water content at a voltage across the MEA of 0.8V

Figure 2.21 shows the contour plot of the various species, overpotential and the ORR in the cathode CL. A significant reduction of the oxygen mole fraction can be observed at the CL-membrane interface near the land area compared to the contour plots for low and medium current density conditions. This results in a non-uniform volumetric current density with highest currents under the gas channel, near the membrane. The overpotential in this case is around 0.49V, similar to the value at medium current densities. Given that the anode overpotential is at most 40mV and that GDL ohmic losses are less than 10mV, the ohmic losses due to the membrane are of the order of 0.3V. The different potential losses in the GDL and the membrane are shown in Figure 2.23. The ohmic losses at the membrane for a current density of  $\approx 1A/cm^2$  represent a substantial contribution to the cell voltage losses. The highest gradient in the electrolyte potential is observed near the anode consistent with the lower water content due to dry-out via electro-osmotic drag.

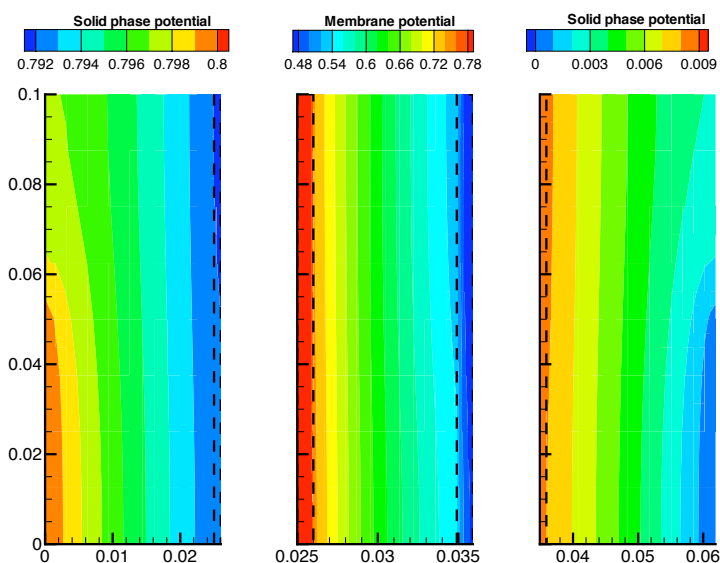


Figure 2.23: Contour plots of the solid phase potential in the anode and cathode GDL and CL, the CL and membrane electrolyte phase potential at a voltage across the MEA of 0.8V

Water content in the anode GDL and CL, membrane, and cathode CL and GDL are shown in Figure 2.22. These contours are very similar to those at medium current densities; however, the anode's relative humidity is lower. This effect results in slightly lower membrane conductivity near the anode electrode, and therefore, in increased ohmic losses. Again, the cathode CL and GDL are saturated and the results of the single-phase model need therefore to be interpreted with caution.

## 2.6.2 Effect of catalyst layer structure: agglomerate vs. pseudo-homogeneous models

Two models have been presented to represent the processes occurring inside the fuel cell electrodes. In this section, the pseudo-homogeneous and agglomerate models are compared. Since the anode kinetics model used by the pseudo-homogeneous and agglomerate models are different, in this section we will compare the following MEA

models:

- Case 1: Anode and cathode modeled using the pseudo-homogeneous model.
- Case 2: Anode modeled using the pseudo-homogeneous and cathode using the agglomerate models.

This permits to assess the models predictive capabilities of mass transport limitations at the cathode without accounting for the different anode kinetics and hydrogen mass transport. The agglomerate model depends on two parameters that define the structure of the catalyst layer, namely, the radius of the agglomerate,  $r_{agg}$ , and the thickness of the electrolyte thin film surrounding the agglomerates,  $\delta_{agg}$ . Four catalyst layer structures are compared to the pseudo-homogeneous models:

- $r_{agg} = 1\mu m$  and  $\delta_{agg} = 80nm$ .
- $r_{agg} = 0.5\mu m$  and  $\delta_{agg} = 40nm$ .
- $r_{agg} = 0.25\mu m$  and  $\delta_{agg} = 20nm$ .
- $r_{agg} = 0.125\mu m$  and  $\delta_{agg} = 10nm$

These structural parameters are chosen in order to keep the volume fraction of solid, electrolyte and void space the same for all cases, namely, 0.409, 0.384 and 0.207 respectively. To solve the pseudo-homogenous model, these volume fractions are also used and the structural parameters are ignored. The input data for both agglomerate and pseudo-homogenous models are given in the Tables in section 2.4.3.

Figure 2.24 shows the polarization curves for the pseudo-homogeneous (Case 1) and the agglomerate (Case 2) models, illustrating the effect of the agglomerate structure on the fuel cell performance. When the agglomerate structural parameters are large, i.e.  $r_{agg} = 1\mu m$  and  $\delta_{agg} = 80nm$ , the polarization curve obtained using the

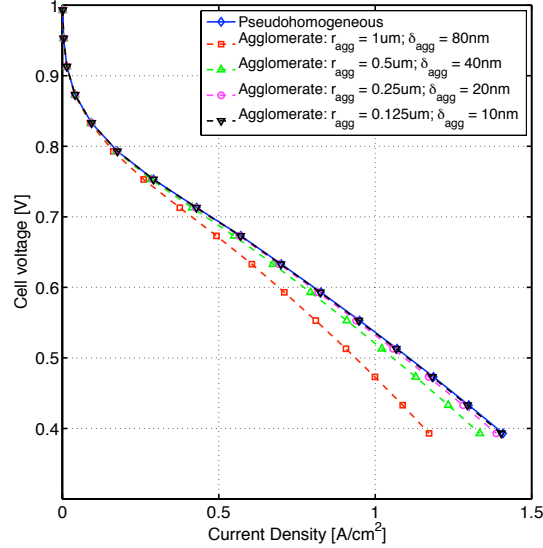


Figure 2.24: Polarization curves obtained using a pseudo-homogeneous (Case1) model and an agglomerate model (Case 2)

agglomerate model shows substantial mass transport limitations and differs significantly from the curve obtained using the pseudo-homogeneous model. A steeper slope is observed in the agglomerate model polarization curves due to a combination of proton and oxygen transport losses.

As the agglomerate structural parameters are reduced, the polarization curves obtained from the two models become almost identical. This occurs for structural parameters  $r_{agg} \leq 0.25\mu m$  and  $\delta_{agg} \leq 20nm$ . These results suggest that even though the catalyst layer is known to be heterogeneous, if the agglomerates are small the catalyst layer can be considered homogeneous and modeled using the pseudo-homogeneous model.

Interestingly, most fuel cell performance curves show mass transport limitations that are not well captured by the pseudo-homogeneous models. On the other hand, values of the order of  $r_{agg} \leq 0.25\mu m$  and  $\delta_{agg} \leq 20nm$  have been reported in the liter-

ature as good estimates of the agglomerate sizes by BET and TEM observation [46]. These apparently conflicting data suggest that the agglomerate's size is not representative of the actual CL structure, but it should instead be interpreted as representing the mean path that dissolved oxygen must travel before reaching a reaction site. The larger size of the agglomerates with respect to the physical CL structure might be due to the flooding of small hydrophilic pores inside the CL. Given that flooding of the CL is likely to occur at medium and high currents as shown in Figures 2.19 and 2.22, and that the mass transport limitations due to the agglomerate structure are only important at the same current densities, the author believes that this might be a reasonable interpretation.

### 2.6.3 Effect of the gas diffusion layer anisotropy

The gas diffusion layer anisotropy affects both gas and electron transport. In this section, anode and cathode GDLs are modeled as isotropic media and the results are compared to the anisotropic predictions. To account for the isotropy of the medium, Bruggeman's equation, eq. (2.56), is used to model both gas and electron transport. To compute the effective diffusion coefficients, the diffusion coefficients in Tables 2.3 and 2.5 are used. To compute the effective conductivity, the average of the in-plane and through-plane conductivities is used, i.e.  $144.41S/cm$ .

Figure 2.25 shows the polarization curve for the isotropic and anisotropic GDL. In this case, both diffusivity and electron conductivities are assumed to be either isotropic or anisotropic. The figure presents negligible differences between the two curves. In order to better understand the effects of diffusivity and electron conductivity, Figures 2.26 and 2.27 show the polarization curves for the cases when either diffusivity or conductivity are made isotropic. The latter two figures show reasonable differences between the isotropic and anisotropic polarization curves. In particular, when the effective diffusion in the GDL is considered anisotropic, the current density predicted

by the model is higher. The reverse effect is observed for the conductivity. As a result, when anisotropic properties in the GDL, conductivity and diffusivity, are all taken into account, their effects cancel each other out and the result is a similar performance curve to the isotropic case.

Anisotropy does have an effect on fuel cell performance; however, conductivity and diffusivity demonstrate opposite effects, which globally cancel each other out. Even though the effect of anisotropy cannot be seen by comparing the polarization curves, differences can be observed in the spacial distribution of the current. Comparing the reactant and volumetric current density distributions in the base case and in the isotropic case in Figure 2.28, it can be observed that the hydrogen mole fraction in the anode is higher in the isotropic case, resulting in lower anode water content and therefore, a drier membrane. The anode volumetric current density distribution is similar in both cases. In the cathode, the volumetric current density distribution in the isotropic case shows a more non-uniform, U-shaped, distribution with the highest current densities occurring between the gas channel and the current collector instead of under the gas channel, as in the anisotropic case. Oxygen in the cathode is also better and more evenly distributed in the isotropic case. This comparison highlights once more the need to perform model assessment and validation based on detailed spatial distribution data as opposed to global polarization curves only [18, 161].

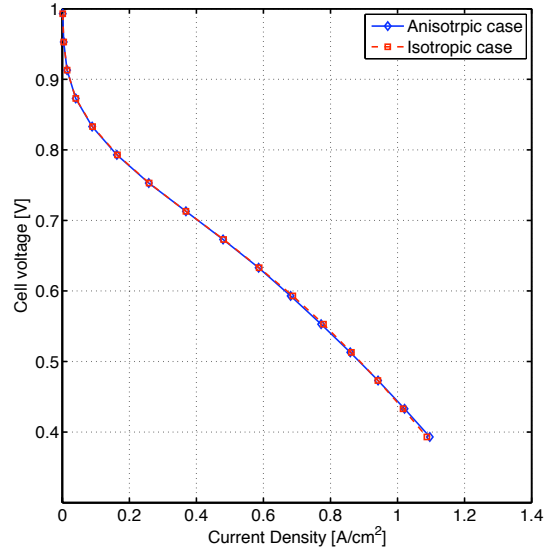


Figure 2.25: Polarization curves for the base case model with anisotropic and isotropic GDL

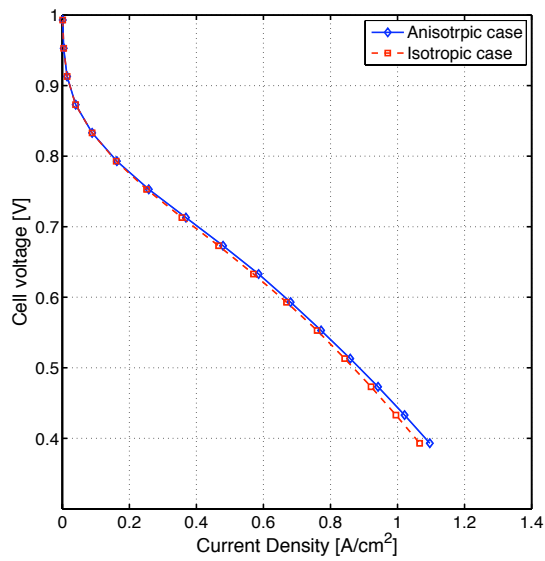


Figure 2.26: Polarization curves for the base case model with anisotropic and isotropic GDL diffusivities

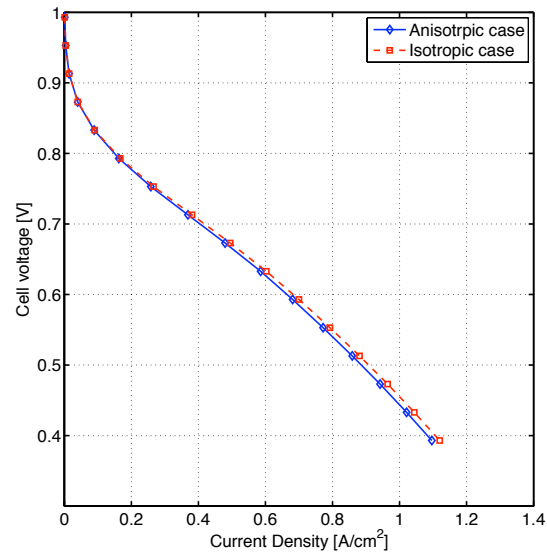


Figure 2.27: Polarization curves for the base case model with an anisotropic and isotropic GDL conductivities

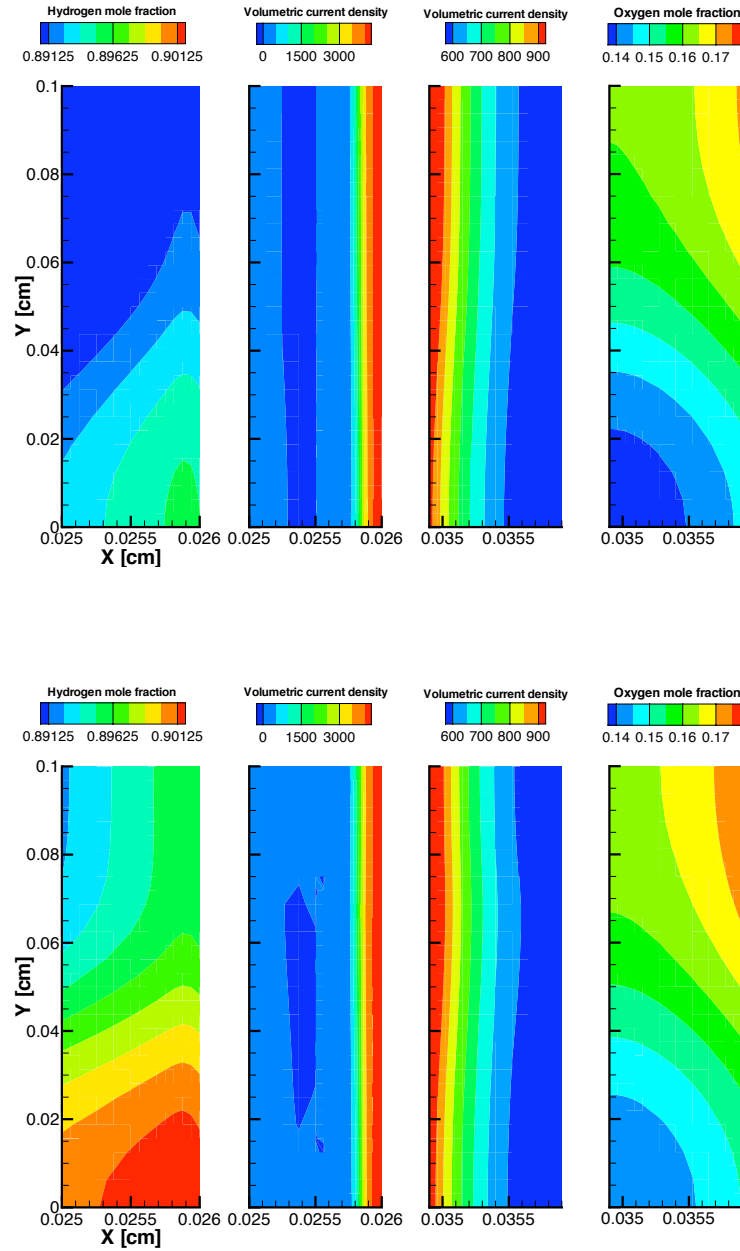


Figure 2.28: Reactant concentrations and volumetric current densities in anode (left) and cathode (right) when the GDL is considered anisotropic (top) and isotropic (bottom).

## Chapter 3

# Membrane electrode assembly optimization

### 3.1 Problem formulation

Improvements in performance, reliability and durability as well as reductions in production costs, remain critical prerequisites for the commercialization of polymer electrolyte membrane fuel cells. Past investigations of electrode design for optimal performance [46,162–165] and low platinum loading [166–168] have been primarily based on trial-and-error or parametric studies. When the number of design variables becomes large, the need for a more systematic and rational approach to optimization of the electrode structure and composition becomes apparent. One such case is the design of a complete membrane electrode assembly (MEA). In this section, a mathematical programming formulation is presented to optimize either MEA performance or MEA performance and cost simultaneously.

### 3.1.1 Objective function

In order to optimize either performance or cost, a measure for these objectives is necessary. This is called the objective function. The objective function is a mathematical representation of the design targets.

The initial design target is to improve performance. Fuel cell performance is commonly described in terms of its polarization behavior, i.e. voltage versus current density. Performance can be improved either at a single operating voltage (single-point optimization) or for a specific range of operating conditions (multi-point or robust optimization). If the goal is to optimize the performance of current MEA designs at a given operating point, e.g. at a fixed cell voltage, the objective function can be expressed simply as the current density at the given voltage. On the other hand, if the goal is to maximize performance for a given operating range, the design objective is more difficult to express mathematically. Possible representations of the objective would be either the optimization of a weighted sum of current densities at several points in the operating range or the optimization of the integral of the polarization curve in the given range. Multi-point optimization is an active area of research and there are several issues regarding the choice of the objective [169,170]. This work deals with single-point optimization problems where the objective function that quantifies performance is given by the current density at the desired voltage. Future work could include multi-point optimization of the MEA.

Cost reduction is the second objective of the optimization. A recent study by General Motors researchers identifies polymer electrolyte membrane and platinum (Pt) costs as the key barriers to achieving the US\$30/kW target for large scale commercialization [171,172]. Whereas the cost of the platinum is not expected to decrease, the cost of the polymer electrolyte could potentially be reduced by a factor of ten, according to electrolyte manufacturers such as DuPont and Asahi Chemical [173]. Consequently, in this thesis it is assumed that platinum loading is a good indicator of

a PEMFC cost and; therefore, the total platinum loading will be used as the objective function representing cost. More sophisticated cost estimators could also be used that take into account other materials and manufacturing; however, this is left for future work.

### 3.1.2 Design variables

In terms of design variables, in the model described in Chapter 2, the anode and cathode catalyst layer compositions are given by five parameters: the platinum loading,  $m_{Pt}$ ; the mass percentage of platinum catalyst on the support carbon black,  $Pt|C$ ; the agglomerate radius,  $r_{agg}$ ; the agglomerate thin film thickness,  $\delta_{agg}$ , and; the electrolyte volume fraction inside the agglomerate,  $\epsilon_{agg}$ . Three of these parameters are used as design variables because it is assumed that they can be controlled: the platinum loading, the mass percentage of platinum catalyst on the support carbon black and, the electrolyte volume fraction inside the agglomerate. The GDL porosity is also included as a design variable.

The platinum loading can be controlled by controlling the amount of catalyst in the ink used to create the CL. By increasing the platinum per unit weight of catalyst ink, the platinum loading can easily be increased. The platinum to carbon ratio can also be controlled by selecting the appropriate catalytic particles. Manufacturers usually provide customers with a selection of catalytic particles with different platinum to carbon ratios ranging from 0.05%wt. platinum on carbon to platinum black [38, 174]. The ionomer film and the amount of ionomer inside the agglomerate provide the total amount of electrolyte in the catalyst layer. It is difficult to discern how much of the electrolyte will become part of the agglomerate and how much it will be used to create an electrolyte film. A study performed by Lee et al. [145] suggests that the thickness of the electrolyte film surrounding the agglomerate increases rapidly when the electrolyte content in the catalyst layer increases from zero to 10%wt.; then it remains almost

constant. Following Lee et al., in this work it is assumed that the electrolyte film surrounding the agglomerate is constant and equal to  $80nm$ . This film value should be adjusted depending on the method of preparation of the catalyst layer. The radius of the agglomerate is also considered constant, even though Song et al. [51] suggest that this value can also be controlled by using different manufacturing processes and ink preparations. The effect of the agglomerate radius and the thin film was already discussed in the previous chapter. The effect of the agglomerate radius and the thickness of the film surrounding the agglomerate on the optimum catalyst layer design was studied by the author and his co-workers in reference [91]. In their work, it is shown that these two parameters should not be included as design variables in the optimization problem because they do not offer any trade-offs. These parameters only represent mass transport resistances due to current CL manufacturing methods and, therefore, its trivial optimal value is zero.

### 3.1.3 Optimization of the MEA performance

In this thesis, two optimization problems are formulated and solved. The first case is to optimize the MEA for maximum performance without taking into account cost constraints. The second case is to optimize the MEA for maximum performance and minimum cost. In the first case, the optimization problem can be specified as

$$\begin{aligned}
 &\text{maximize} && i(\phi_0 = dV) \\
 &\text{w.r.t.:} && m_{Pt,c}, \epsilon_{agg,c}, Pt|C_c, \epsilon_{V,c}^{gd}, \\
 &&& m_{Pt,a}, \epsilon_{agg,a}, Pt|C_a, \epsilon_{V,a}^{gd} \\
 &\text{subject to:} && 0 < \epsilon_{V,c}^{cl} \leq 1; \quad 0 < \epsilon_{S,c}^{cl} \leq 1; \quad 0 < \epsilon_{N,c}^{cl} \leq 1 \\
 &&& 0 < \epsilon_{V,a}^{cl} \leq 1; \quad 0 < \epsilon_{S,a}^{cl} \leq 1; \quad 0 < \epsilon_{N,a}^{cl} < 1
 \end{aligned} \tag{3.1}$$

The total number of design variables is eight. The constraints guarantee that the volume fraction of each one of the three phases of the anode and cathode CL are not

Table 3.1: Initial upper and lower bounds for the design parameters used to optimize the MEA

Design variable	Upper bound	Lower bound
$m_{Pt}, [mg/cm^2]$	1.0	0.0
$\epsilon_{agg}, [-]$	0.9	0.1
$Pt C[-]$	1.0	0.05
$\epsilon_V^{gd}, [-]$	0.9	0.1

negative or larger than one which would be unphysical. In addition to the constraints shown above, the design variables are also constrained to be inside a given range, i.e. bounded. The bounds for each one of the design variables are shown in Table 3.1. The most important bound is the upper bound for the platinum loading, which can be viewed as a cost constrained. In this case, this value is set to  $1.0mg/cm^2$  which is more than twice that of currently used platinum loadings [175]. The lower bound for the platinum to carbon ratio is set to 0.05 because this is the lowest amount of platinum per catalyst that exists commercially [174].

### 3.1.4 Optimization of the MEA cost and performance

The second problem that is solved in this thesis is that of maximizing performance while minimizing cost. In this case, the optimization problem has two objectives that need to be minimized/maximized simultaneously. When there are multiple objectives to be considered, the optimization problem is known as multiobjective. For multiobjective problems, methods to optimize scalar objectives cannot be used directly.

Multiobjective or multicriteria optimization has its roots in late-nineteenth-century welfare economics in the works of Edgeworth and Pareto [176, 177]. A mathematical

formulation of such problem is given by

$$\begin{aligned}
 &\text{minimize} && \mathbf{F}(\mathbf{x}) = [J_1 J_2 \cdots J_n]^T \\
 &\text{w.r.t.} && \mathbf{x} \\
 &\text{subject to:} && \mathbf{G}(\mathbf{x}) \leq 0 \\
 &&& \mathbf{M}(\mathbf{x}) = 0 \\
 &&& \mathbf{x}_L \leq \mathbf{x} \leq \mathbf{x}_U
 \end{aligned} \tag{3.2}$$

where  $J_i$  is one of the objectives to be minimized,  $\mathbf{F}(\mathbf{x})$  is the vector of objectives,  $\mathbf{G}(\mathbf{x})$  and  $\mathbf{M}(\mathbf{x})$  are the vector of inequality and equality constraints respectively and, the last inequality represents the bounds for each design variable.

The scalar concept of optimality does not apply directly to the multiobjective problem because there are more than one optimal solutions depending on the importance of each objective. A useful notion is that of the *Pareto optimality*. A design,  $\mathbf{x}$ , is a *Pareto optimal solution* for the problem (3.2), if all other feasible designs have a higher value for at least one of the objective functions  $J_i$ , or else have the same value for all objectives [178]. Stadler applied the notion of Pareto optimality to the fields of engineering and science in the 1970s [176, 179].

Given the definition of Pareto optimality, Pareto optimality solutions,  $\mathbf{x}^*$ , are nonunique. The *Pareto optimal set* is defined as the set that contains all Pareto optimal solutions. Furthermore, the *Pareto front* is the set that contains the objectives of all optimal solutions. Since all Pareto optimal solutions are good solutions, the most appropriate solution will depend only upon the trade-offs between objectives; therefore, it is the responsibility of the designer to choose the most appropriate solution. It is sometimes desirable to obtain the complete set of Pareto optimal solutions, from which the designer may then choose the most appropriate design.

There is a large array of methods for solving multiobjective problems and for obtaining the set of Pareto optimal solutions [176–178, 180–182]. One of the most

widely used methods for multiobjective optimization is the weighted sum method [180]. In this method, the multiple objectives are transformed into a single objective function by multiplying each objective by a weighting factor and summing up all contributions such that the final objective is:

$$J_{weighted \quad sum} = w_1 J_1 + w_2 J_2 + \dots + w_n J_n \quad (3.3)$$

where  $w_i$  are the weighting factors. If the sum of all weights is equal to one, then the weighted sum is said to be a convex combination of objectives; if all objectives are convex, the weighted sum objective will also be convex. Each single set of weights determines one particular Pareto optimal solution. Then, a Pareto front can be obtained by systematically changing the weights and solving the given optimization problem. The weighted sum method is easy to implement and it can easily be understood; however it has two drawbacks: 1) a uniform spread of weight parameters rarely produces a uniform spread of points on the Pareto set; 2) non-convex parts of the Pareto set cannot be obtained [183].

In this thesis, the weighted sum method is used because we are primarily interested in a small number of solutions in the Pareto set, and the physical meaning of the weights is easily interpreted. Furthermore, the method has been shown to provide good results for most engineering applications, and it is readily implemented in DAKOTA [69], the OpenSource optimization program used in this thesis.

The MEA multiobjective optimization problem is formulated using a simple weighted sum method as

$$\begin{aligned}
 &\text{minimize} && -w_1 i(\phi_0 = dV) + w_2(m_{Pt,c} + m_{Pt,a}) \\
 &\text{w.r.t.:} && m_{Pt,c}, \epsilon_{agg,c}, Pt|C_c, \epsilon_{V,c}^{gd} \\
 &&& m_{Pt,a}, \epsilon_{agg,a}, Pt|C_a, \epsilon_{V,a}^{gd} \\
 &\text{subject to:} && 0 < \epsilon_{V,c}^{cl} \leq 1; \quad 0 < \epsilon_{S,c}^{cl} \leq 1; \quad 0 < \epsilon_{N,c}^{cl} \leq 1 \\
 &&& 0 < \epsilon_{V,a}^{cl} \leq 1; \quad 0 < \epsilon_{S,a}^{cl} \leq 1; \quad 0 < \epsilon_{N,a}^{cl} < 1
 \end{aligned} \quad (3.4)$$

where  $w_1 + w_2 = 1$  and where a negative sign has been added in front of the performance objective, i.e. the current density, in order for the two objectives to be made into minimization problems. In order for the weighted sum method to search the Pareto set effectively, objectives need to be scaled to similar values [5]. In this case, both current density and total platinum loading are of the same order of magnitude and therefore scaling is not required.

## 3.2 Sensitivity analysis

In the optimization problems in the previous section, one of the objective functions is the fuel cell current density at a given MEA voltage. Current density is obtained during postprocessing. The current density per unit area of a fuel cell can be obtained by integrating the volumetric current density over the volume of either the anode or the cathode CL,

$$\begin{aligned} f(\mathbf{u}, \mathbf{p}) &= i(x_{O_2}, \phi_S, \phi_m; m_{Pt,c}, \epsilon_{agg,c}, Pt|C_c, \epsilon_{V,c}^{gd}, m_{Pt,a}, \epsilon_{agg,a}, Pt|C_a, \epsilon_{V,a}^{gd}) \\ &= \frac{1}{H} \int_0^H \int_0^L \nabla \cdot \mathbf{i} dx dy \quad (3.5) \end{aligned}$$

where  $\nabla \cdot \mathbf{i}$  is given in equation (2.33),  $H$  is the height of the domain and  $L$  is the width of the domain, i.e. the thickness of the CL. The second objective, i.e. the total platinum loading, is given by the design variables. The constraint equations in the optimization problem in (3.4) are given directly by the analysis model. Hence, no extra computations are required in order to determine the second objective and the constraints.

The analytic sensitivities of the objective function  $f$ , with respect to any of the

design variables  $p_i$ , can be obtained using functional analysis as

$$\begin{aligned} \frac{df(\mathbf{u}, \mathbf{p})}{dp_i} &= \frac{\partial f(\mathbf{u}, \mathbf{p})}{\partial u_j} \frac{\partial u_j}{\partial p_i} + \frac{\partial f(\mathbf{u}, \mathbf{p})}{\partial p_i} \\ &= \frac{1}{H} \int_0^H \int_0^L \left( \frac{\partial(\nabla \cdot \mathbf{i})}{\partial u_j} \frac{\partial u_j}{\partial p_i} + \frac{\partial(\nabla \cdot \mathbf{i})}{\partial p_i} \right) dx dy \quad (3.6) \end{aligned}$$

where  $\mathbf{u}$  is the vector of unknowns solved for by the analysis program,  $\mathbf{p}$  is the vector of design parameters,  $i = 1, \dots, 8$ ,  $j = 1, \dots, 5$ ,  $\frac{\partial(\nabla \cdot \mathbf{i})}{\partial u_j}$  and  $\frac{\partial(\nabla \cdot \mathbf{i})}{\partial p_i}$  are obtained by analytical differentiation of either equation (2.33) or equation (2.44) with respect to the solution vector and the design variables respectively and, finally, the term  $\frac{\partial u_j}{\partial p_i}$  is unknown and represents the change of the solution vector with respect to the design variables. This vector can be obtained by noticing that any perturbation in the parameters of the system should result in no variation of the residual if the governing equation is to continue to be satisfied. Therefore, at the solution, the total derivative of the residual has to be zero. Then,  $\frac{\partial u_j}{\partial p_i}$  is computed by solving the system of partial differential equations given by

$$\frac{\partial R(\mathbf{u}, \mathbf{p})}{\partial u_j} \frac{\partial u_j}{\partial p_i} = - \frac{\partial R(\mathbf{u}, \mathbf{p})}{\partial p_i} \quad (3.7)$$

where  $\frac{\partial R(\mathbf{u}, \mathbf{p})}{\partial u_j}$  and  $\frac{\partial R(\mathbf{u}, \mathbf{p})}{\partial p_i}$  represent the derivatives of the governing equations in (2.129) with respect to the solution vector and the design variables respectively. These are obtained using functional analysis. Note that  $\frac{\partial R(\mathbf{u}, \mathbf{p})}{\partial u_j} \frac{\partial u_j}{\partial p_i}$  is a directional derivative and therefore results in a differential equation with the vector  $\frac{\partial u_j}{\partial p_i}$  as the unknown [118, 119]. For example, for design variable  $p_i$ , from the first term of equation (2.29),

$$\frac{\partial R_1(\mathbf{u}, \mathbf{p})}{\partial u_j} \frac{\partial u_j}{\partial p_i} = \nabla \cdot \left( c_g D_{O_2} \nabla \left( \frac{\partial x_{O_2}}{\partial p_i} \right) \right) - \frac{1}{4F} \frac{\partial(\nabla \cdot \mathbf{i})}{\partial u_j} \Big|_{u=u^n} \frac{\partial u_j}{\partial p_i} \quad (3.8)$$

where  $R_1(\mathbf{u}, \mathbf{p}) = \nabla \cdot (c_g D_{O_2} \nabla x_{O_2}) - S_{O_2} = 0$ . Once an analytic expression for these terms is obtained, the system of PDEs is discretized using the finite element method

and the *deal.ii* finite element libraries [116] with appropriate boundary conditions. In this case, the boundary conditions for the unknown vector  $\frac{\partial u_j}{\partial p_i}$  are Neumann boundary conditions with the value set to zero. After discretization and application of the boundary conditions, the resulting linear system is solved using UMFPACK [121,122], an efficient direct solver for nonsymmetric linear systems. The terms  $\frac{\partial R(\mathbf{u},\mathbf{p})}{\partial u_j}$  and  $\frac{\partial R(\mathbf{u},\mathbf{p})}{\partial p_i}$  depend on the solution of the governing equations; therefore, this system of equations can only be solved after solving the governing equations as shown in Figure 3.1. Finally, note that this system is of the same size as the original linearized system of governing equations, and that it must be solved for each design variable  $p_i$ .

This method of obtaining the analytic sensitivities is called the direct formulation. It was chosen here instead of the adjoint formulation because of its ease of implementation. A similar approach for computing sensitivities was also used in reference [134] when solving a least squares problem to estimate fuel cell model parameters from experimental data. As the number of design variables increases, the adjoint formulation is proven to be more efficient [184].

Once the analytic sensitivities were implemented in the code, they were validated by comparing them to the numerical sensitivities computed using forward differences. Table 3.2 shows the results from the validations, performed using the data for the base case analyzed in Chapter 2 and with  $dV = 0.6V$ . Table 3.2 shows good agreement between analytic and numeric sensitivities.

### 3.3 Design and optimization numerical framework

The MEA finite element model together with the analytic sensitivities of the objective function and constraints are coupled to the optimization package DAKOTA [69], as shown in Figure 3.1. In this figure, the three main iterative loops can be identified. The inner or analysis loop, is used to solve the nonlinear governing equations. The middle or adaptive refinement loop, is used to check the accuracy of the solution and

Table 3.2: Analytic vs. numeric sensitivities of the current density with respect to the different design variables

Design variable	Analytic	Numeric ( $\delta h = 10^{-3}$ )	Numeric ( $\delta h = 10^{-6}$ )	Numeric ( $\delta h = 10^{-9}$ )
$m_{Pt,c}$	-0.142372	-0.0687236	-0.142464	-0.142537
$\epsilon_{agg,c}$	-0.402701	-0.395109	-0.403485	-0.403496
$Pt C_c$	-0.133119	0.0199059	-0.13348	-0.133586
$\epsilon_{V,c}^{gd}$	-0.0372749	-0.0370176	-0.0373775	-0.0373783
$m_{Pt,a}$	0.22157	0.243804	0.217927	0.217901
$\epsilon_{agg,a}$	-0.116418	-0.1146	-0.117929	-0.117933
$Pt C_a$	-0.288358	-0.246353	-0.283881	-0.283923
$\epsilon_{V,a}^{gd}$	0.0199154	0.2042	0.0202678	0.0202678

to adapt the computational mesh as necessary using an *a posteriori* error estimator. The outer, or, optimization loop, is used to change the design parameters in order to obtain an improved design.

The analysis loops solves the nonlinear system of PDEs using Newton's method in conjunction with a line search for added robustness, see section 2.1.2 for details. The adaptive loop is used in order to refine the mesh automatically during the solution process, where the largest numerical errors are predicted using an error estimator, see also section 2.1.2. This allows the solver to provide a grid independent solution even though the design parameters and, as a consequence, the transport and electrochemical parameters of the problem are constantly changing during the design process.

During the optimization loop, after the objective function, constraints and their analytic sensitivities have been computed, these values are passed on to an interior-point quasi-Newton algorithm implemented in DAKOTA [69]. This optimization algorithm is based on the interior-point method, which is a gradient-based optimization algorithm as discussed in the literature review in Chapter 1. DAKOTA is an Open-Source optimization software developed at Sandia National Labs. The optimization

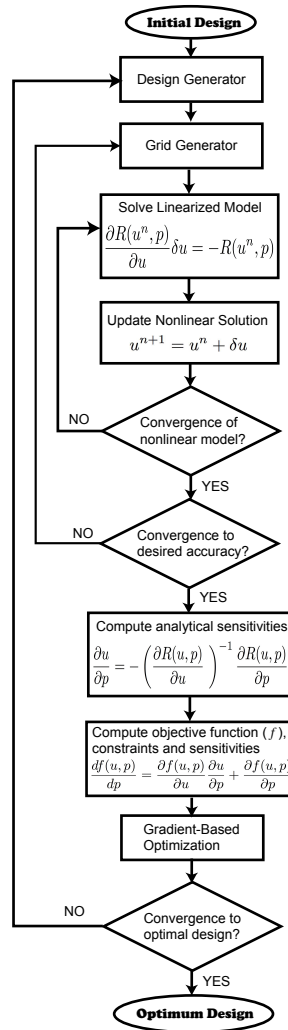


Figure 3.1: Implementation of the multivariable optimization framework with adaptive refinement and analytic sensitivities.

algorithm uses the objective function, constraints and their gradients or sensitivities to change the design parameters in order to achieve a new design with better performance. These parameters are then passed back to the model and the process is repeated starting at the analysis loop. Convergence of the optimization algorithm is achieved when

$$\frac{f(\mathbf{u}, \mathbf{p}_{k+1}) - f(\mathbf{u}, \mathbf{p}_k)}{f(\mathbf{u}, \mathbf{p}_k)} \leq 10^{-3} \quad (3.9)$$

or the  $L_2$  norm of the gradient of the objective function is less than  $10^{-3}$ .

## 3.4 Optimization results

In this section, the membrane electrode assembly model developed in Chapter 2 is used to obtain the optimal MEA composition for

- Maximum performance
- Maximum possible performance at a reasonable cost

### 3.4.1 Optimization of the MEA performance

The MEA performance optimization problem formulated in section 3.1.3 will be solved under three different operating conditions: 0.4, 0.6 and 0.8V across the MEA and for the geometry and operating conditions in Table 2.2. These three operating points represent the cell operating at low, medium and high current densities. At low current densities, the MEA losses are mainly due to the cathode overpotential. At medium current densities, the MEA losses are due to both cathode overpotential and membrane resistance. At high current densities, membrane resistance and cathode mass transport losses are the main contributors to the loss in performance.

### Optimization of the MEA performance at low current densities ( $dV = 0.4V$ )

The initial design described in Chapter 2 provides a current density of  $0.1627A/cm^2$  at an MEA voltage of  $0.4V$ , i.e. a cell voltage of  $0.793V$ . Starting with this electrode design, the optimization problem outlined in equation (3.1) is solved using the quasi-Newton interior-point method in DAKOTA [69]. After 24 iterations and approximately 30 minutes on a 2 GHz Power Mac G5, the optimization algorithm converged to a new design that provides a current density of  $0.2789A/cm^2$ . Figure 3.2 shows the evolution of the objective function and design variables during the optimization process. During the optimization process, all design variables are changed simultaneously. The optimal design variables are  $\{m_{Pt,c}, \epsilon_{agg,c}, Pt|C_c, \epsilon_{V,c}^{gdl}, m_{Pt,a}, \epsilon_{agg,a}, Pt|C_a, \epsilon_{V,a}^{gdl}\} = \{1.0, 0.5430, 0.6719, 0.4036, 0.6558, 0.6839, 0.6358, 0.1003\}$ . For these values, the volume fractions of void, electrolyte and solid phase are 0.1986, 0.5106, 0.2907 and 0.1296, 0.6520, 0.2184 for cathode and anode respectively. Note that the platinum loading reaches its maximum value. This is not always the case and depends on the activity of the catalytic particles. For example, using previous E-TEK catalytic data, the optimal platinum loading had two optimal values one of which was not its upper bound [185].

Figure 3.3 shows the performance of the optimized MEA with respect to the base design. Performance is clearly enhanced at low current densities; however, at medium and high current densities, the performance improvements are less significant. Through comparison of the optimal and base designs, these results could have been expected. Due to the substantial increase in platinum loading in the cathode and anode, the overpotential losses are reduced, thereby considerably moving the polarization curve upwards. Both anode and cathode GDL and CL porosities are reduced substantially during the optimization. The reduced porosity reduces ohmic losses, which, at low current densities, represent a larger contribution to the MEA

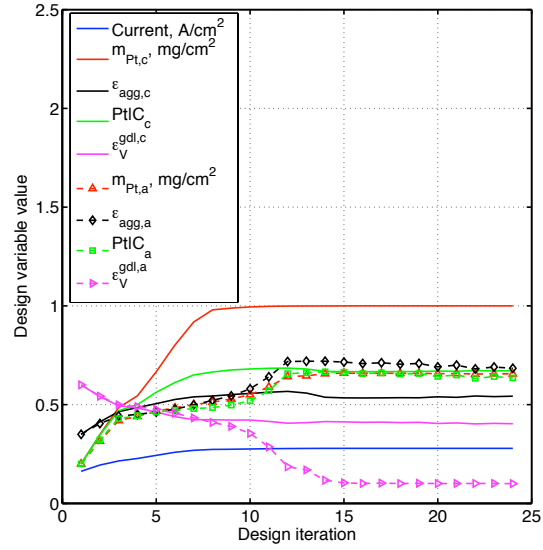


Figure 3.2: Evolution of the objective function and design variables during the optimization process for a voltage across the electrode of 0.4V, i.e. a cell voltage of 0.793 V.

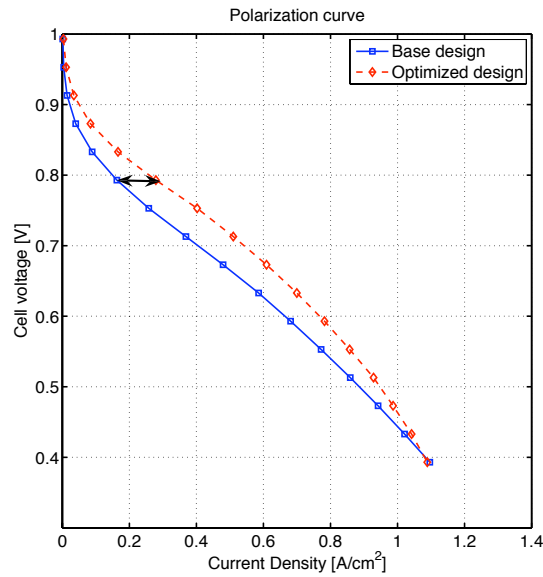


Figure 3.3: Polarization curve for the base case and for the optimal design for a voltage across the electrode of 0.4V, i.e. a cell voltage of 0.793 V.

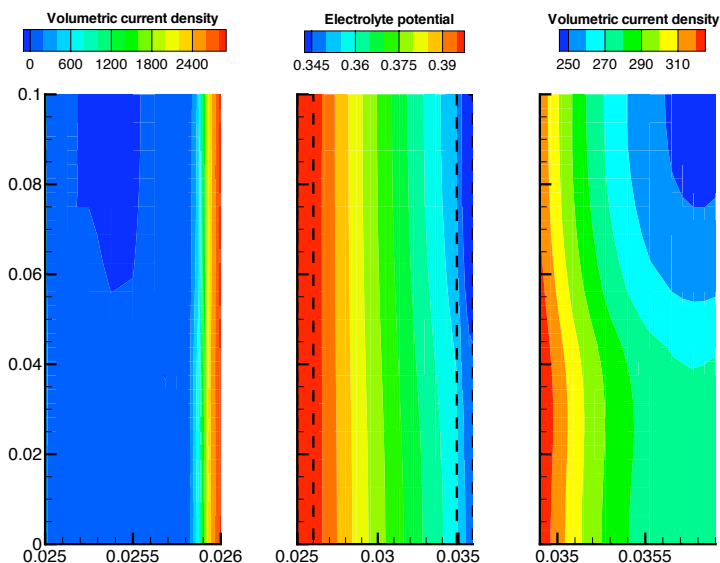


Figure 3.4: Contour lines for the optimized electrode design at  $dV = 0.4V$  of of anode CL volumetric current density [ $A/cm^3$ ] (left), CL and membrane potential in the electrolyte [V] (center) and cathode CL volumetric current density [ $A/cm^3$ ] (right).

losses than mass transport limitations. The low porosity also helps the cathode to retain the water that is produced during the reaction. Therefore, the low porosity results in improvements in performance at low current densities. Unfortunately, low porosity becomes a drawback at high currents and hence the similar performance of the optimal design even with higher platinum loading.

Figure 3.4 shows the volumetric current density in the anode and cathode CL as well as the electrolyte potential in the membrane and the CLs. Comparing the volumetric current densities for this design and the base design in Figures 2.14 and 2.15, the contour plot in the anode remains the same. In the cathode however, the volumetric current density distribution is very different. The highest values of volumetric current density are now located under the current collector area, near the membrane, instead of uniformly distributed near the membrane. This phenomenon is most likely due to the higher electrolyte conductivity in the cathode under the current

collector. Due to the higher conductivity in this area, the membrane potential and, thereby the overpotential, are higher causing the electrochemical reaction to occur more rapidly.

### Optimization of the MEA performance at medium current densities (dV = 0.6V)

The initial design described in Chapter 2 provides a current density of  $0.6810A/cm^2$  at an MEA voltage of 0.6V, i.e. a cell voltage of 0.593V. The optimization problem is solved using this MEA as a starting point. After 14 iterations and approximately 19 minutes on a 2 GHz Power Mac G5, the optimization algorithm converged to a new design that provides a current density of  $0.8852A/cm^2$ . Figure 3.2 shows the evolution of the objective function and design variables during the optimization process. The design variables at this new design are  $\{m_{Pt,c}, \epsilon_{agg,c}, Pt|C_c, \epsilon_{V,c}^{gdl}, m_{Pt,a}, \epsilon_{agg,a}, Pt|C_a, \epsilon_{V,a}^{gdl}\} = \{0.9998, 0.6866, 0.7766, 0.6461, 0.5764, 0.6858, 0.6461, 0.5856\}$ . For these values, the volume fractions of void, electrolyte and solid phase are 0.2406, 0.5691, 0.1846 and 0.2596, 0.5557, 0.1902 for cathode and anode respectively.

Figure 3.6 shows the performance of the optimized MEA with respect to the base design. Performance is clearly enhanced at low, medium and high current densities. The increase in performance in this case is due to the substantial increase in platinum loading in the cathode and anode and an increase in the electrolyte volume fraction. Furthermore, in this case, since the objective was to optimize performance at medium current densities, both anode and cathode GDL and CL porosities are increased with respect to the design at low current densities and are also slightly higher than the base design. Therefore, the current design minimizes ohmic losses in the electrolyte by increasing its volume fraction in the CL and at the same time reduces mass transport limitation by increasing the porosities of GDL and CL.

Figure 3.7 shows the volumetric current density in the anode and cathode CL as

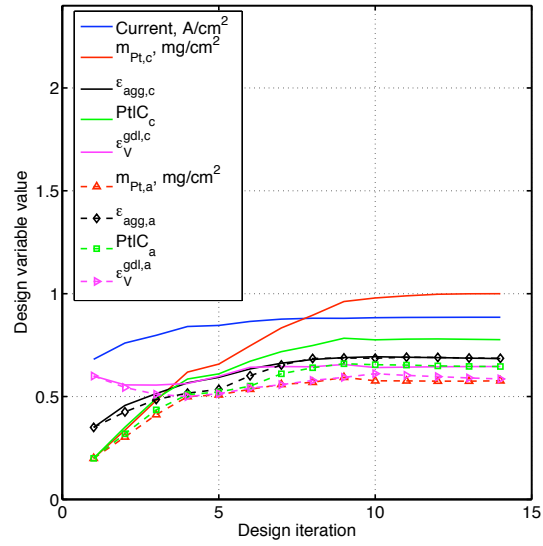


Figure 3.5: Evolution of the objective function and design variables during the optimization process for a voltage across the electrode of 0.6V, i.e. a cell voltage of 0.593 V.

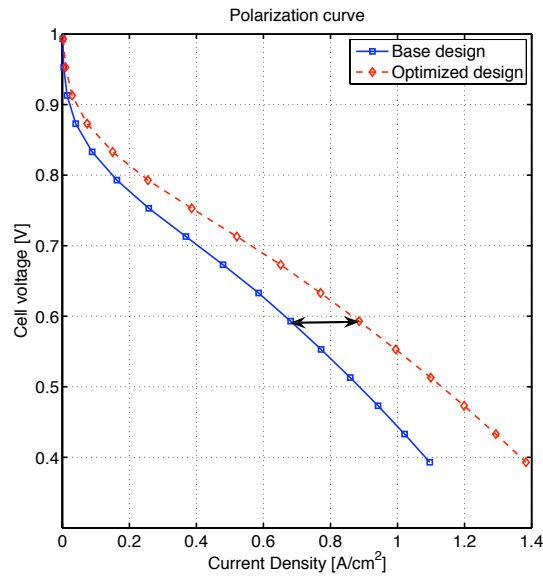


Figure 3.6: Polarization curve for the base case and for the optimal design for a voltage across the electrode of 0.6V, i.e. a cell voltage of 0.593 V.

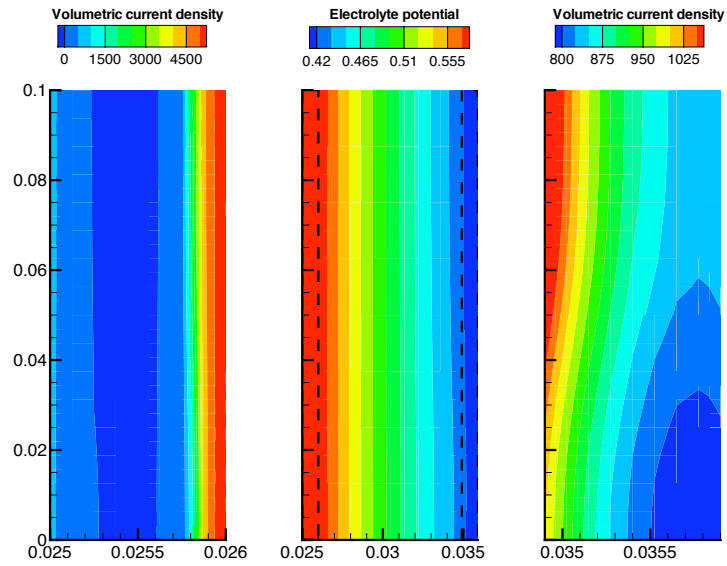


Figure 3.7: Contour lines for the optimized electrode design at  $dV = 0.6V$  of of anode CL volumetric current density [ $A/cm^3$ ] (left), CL and membrane potential in the electrolyte [V] (center) and cathode CL volumetric current density [ $A/cm^3$ ] (right).

well as the electrolyte potential in the membrane and the CLs for the optimum design at  $dV = 0.6V$ . Comparing the volumetric current densities for this design and the base design in Figures 2.17 and 2.18, the contour plot in the anode remains quite similar even though the current produced is increased. In the cathode, it can be observed that the reaction increases everywhere in the CL. The highest increases occur under the gas channel. In comparison with the design at low current densities, Figure 3.4, the area with the highest reaction rates have shifted from the area under the current collector to the area under the gas channel. This shows that, at this current density, mass transport limitations are relatively more important than membrane conductivity. Furthermore, in this case, enough water is generated in the cathode to have a fully humidified electrolyte everywhere in the CL. This effect can be observed by the uniformity of the electrolyte membrane potential that only changes in the x-direction.

### **Optimization of the MEA performance at high current densities ( $dV = 0.8V$ )**

The initial design described in Chapter 2 provides a current density of  $1.0962A/cm^2$  at an MEA voltage of  $0.8V$ , i.e. a cell voltage of  $0.393V$ . After 28 iterations and approximately 35 minutes on a 2 GHz Power Mac G5, the optimization algorithm converged to a new design that provides a current density of  $1.3996A/cm^2$ . The design variables at this new design are  $\{m_{Pt,c}, \epsilon_{agg,c}, Pt|C_c, \epsilon_{V,c}^{gd}, m_{Pt,a}, \epsilon_{agg,a}, Pt|C_a, \epsilon_{V,a}^{gd}\} = \{1.0, 0.7104, 0.8063, 0.6919, 0.4589, 0.7003, 0.6039, 0.6774\}$ . For these values, the volume fractions of void, electrolyte and solid phase are  $0.2752, 0.5581, 0.1718$  and  $0.2777, 0.5505, 0.1666$  for cathode and anode respectively.

Figure 3.8 shows the performance of the optimized MEA with respect to the base design and the design at medium current densities. The designs at medium and high current densities show very similar performance. Comparing the value of the design parameters between these two designs, it is easy to observe that only small changes

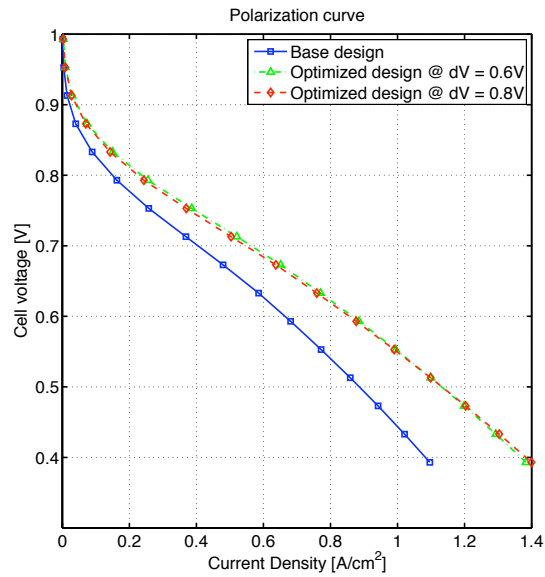


Figure 3.8: Polarization curve for the base case and for the optimal design for a voltage across the electrode of 0.6V and 0.8V, i.e. a cell voltage of 0.593 and 0.393 V.

in the design variables exist. The main changes are slight increases in GDL and CL porosities and in the amount of electrolyte in the CL. These increases are possible due to a reduction in the amount of carbon in the CL. These small changes result in decreased performance at low current densities due to higher electric ohmic losses, and an increase in performance at high current densities due to a reduction in the effective electrolyte conductivity as well as further reductions in the mass transport limitations.

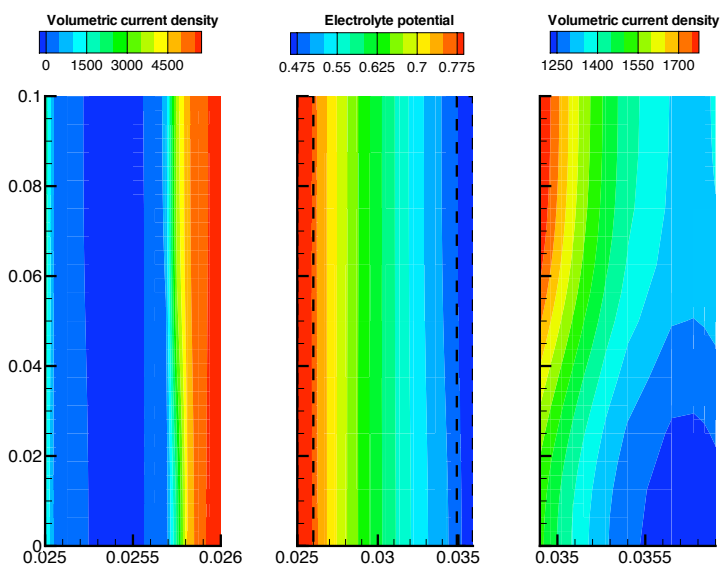


Figure 3.9: Contour lines for the optimized electrode design at  $dV = 0.8V$  of anode CL volumetric current density [ $A/cm^3$ ] (left), CL and membrane potential in the electrolyte [V] (center) and cathode CL volumetric current density [ $A/cm^3$ ] (right).

Figure 3.9 shows the volumetric current density in the anode and cathode CL as well as the electrolyte potential in the membrane and the CLs for the optimum design at  $dV = 0.8V$ . Both anode and cathode volumetric current density distributions are almost identical to the ones shown in Figure 3.7, therefore showing that even at high current density, mass transport limitations are not dominant factors. Compared to the anode volumetric current density distribution in the base design in Figure

2.20, a larger part of the CL is being utilized for the reaction, and the values of the volumetric current density are also higher. In the cathode, the volumetric current density distribution is also higher everywhere in the CL, and the distribution is slightly more non-uniform compared with the base case in 2.21.

### Globality of the solution

Table 3.3: Base and optimal design at different voltages

Design variables	Case 1	Case 2	Case 3	Case 4
$m_{Pt,c}$	0.5	0.2	0.2	0.5
$\epsilon_{agg,c}$	0.35	0.1	0.35	0.35
$Pt C_c$	0.5	0.2	0.2	0.5
$\epsilon_{V,c}^{gdl}$	0.6	0.6	0.2	0.2
$m_{Pt,a}$	0.5	0.2	0.2	0.2
$\epsilon_{agg,a}$	0.35	0.1	0.35	0.35
$Pt C_a$	0.5	0.2	0.2	0.2
$\epsilon_{V,a}^{gdl}$	0.6	0.6	0.6	0.6

In order to obtain an optimal solution in a reasonable amount of time, the optimization algorithm used is a gradient-based method. Gradient-based methods can only guarantee that the solution obtained is a local optimum unless the objective function and constraints are convex. In order to check that the solution is indeed a global one, in this section the optimization problem of optimizing performance at an MEA voltage of 0.6V is solved from four different starting points and the results are compared. The initial starting points are shown in Table 3.3. In Case 1, the effect of the initial value of the platinum loading and the platinum to carbon ratio in both anode and cathode is analyzed by increasing their values from 0.2 to 0.5. In Case 2, the effect of the initial value of the electrolyte volume fraction inside the agglomerate in both anode and cathode is analyzed by reducing its value from 0.35 to 0.1. In Case 3, the effect of the GDL porosity is analyzed by decreasing its value to 0.2. In Case

4, the effect of starting with a different design for anode and cathode is analyzed. If all initial designs reach the same solution, then it is likely that the solution is global one. Furthermore, it is also reasonable to assume that the optimization problem is convex.

The optimization problem in equation (3.1) was successfully solved with each one of the initial designs. For some initial designs such as Case 1 and Case 4, the optimization algorithm took several additional iterations; however, it eventually converged to the solution. Table 3.4 shows the optimal design obtained starting from the various initial designs in Table 3.3 as well as the design obtained in the previous section (Case 0). The table also shows the maximum current density obtained for each design. Comparing the value of the objective function,  $i$ , this value is almost identical for all designs. In particular, taking into account that the convergence criteria is  $\frac{(f-f_0)}{f} \leq 10^{-3}$ , the difference between the five designs is less than the convergence criteria and; therefore, the value of the objective can be considered to be the same. The designs are also very similar. The cathode design parameters are almost identical for all five cases. The anode parameters for the various designs are slightly different. The agglomerate electrolyte volume fraction and GDL porosity in the anode are, again, almost identical. However, the platinum to carbon ratio and the platinum loading in the anode are different by as much as 15% between cases 1 and 4. Electrode kinetics in the anode are extremely fast; therefore, the sensitivity of the current density to these design parameters is negligible. Because all designs yield the same value for the objective function, and all designs yield a similar design, it is assumed that the solution obtained is a global solution. Notice that if the convergence criteria was more stringent, the optimal design would be even more similar because the small sensitivities of the objective function to changes in the anode platinum loading would also be taken into account. Since a global solution is achieved using a gradient-based method, it is assumed that the objective function and the constraint set are convex.

Table 3.4: Base and optimal design starting from different initial designs

Design	Case 0	Case 1	Case 2	Case 3	Case 4
$i$	0.8852	0.8849	0.8851	0.8850	0.8852
$m_{Pt,c}$	0.9998	1.0	0.9999	1.0	0.9999
$\epsilon_{agg,c}$	0.6866	0.6835	0.6840	0.6824	0.6841
$Pt C_c$	0.7766	0.7760	0.7764	0.7752	0.7763
$\epsilon_{V,c}^{gdl}$	0.6461	0.6460	0.6448	0.6478	0.6488
$m_{Pt,a}$	0.5764	0.4916	0.5523	0.5430	0.5817
$\epsilon_{agg,a}$	0.6858	0.6860	0.6865	0.6856	0.6864
$Pt C_a$	0.6461	0.6033	0.6352	0.6298	0.6492
$\epsilon_{V,a}^{gdl}$	0.5856	0.5846	0.5891	0.5882	0.5840

### Final remarks and experimental comparison

Table 3.5 shows the design variables for the base design and the three optimal designs discussed in the previous sections. The base design has the same structure for both anode and cathode. Each optimal design results in a different design for the anode and cathode electrodes thereby highlighting the varying relative importance of the physical phenomena that affect the reaction on the anode and the cathode. In all cases, the cathode CL reaches the maximum platinum loading allowed. The amount of electrolyte inside the agglomerate increases when the current density increases. The platinum to carbon ratio of the catalyst also increases. Because carbon has a lower density than platinum, this results in a CL with a reduced solid phase volume fraction, as shown in Table 3.6. The GDL porosity also increases with increasing operating current density. At low currents, mass transport limitations are negligible and porosity is low. As the required current density increases, the GDL porosity increases in both cathode and anode. In the anode, the platinum loading does not reach its upper bound as a result of the fast HOR kinetics. The agglomerate electrolyte content is similar in all designs to a value of around 0.7. Platinum to carbon ratio is reduced as current density requirements increase.

Table 3.6 shows the void, electrolyte and solid phase volume fractions in the cathode and anode CL for the base design and the previously discussed optimal designs. This table clearly shows the effect of optimizing at higher voltages across the MEA, i.e. at higher currents. As the optimization operating conditions move right on the polarization curve, the porosity of the CL is increased, showing the increased importance of mass transport. In the anode, the maximum electrolyte volume fraction occurs at low current densities; this could possibly occur because proton transport is the limiting mechanism in this regime, since most of the reaction occurs near the membrane-CL interface. In the cathode, the maximum electrolyte volume fraction occurs at medium current densities where ohmic losses are the most important. At low currents, kinetic limitations are more important; at high currents, mass transport becomes the dominant effect. Finally, solid phase volume fraction decreases monotonically along with design operating conditions. In the table, it is easy to see the interplay between the void and the solid phase volume fractions. As void fraction increases, solid phase volume fraction decreases leaving space for the pores to be formed.

Table 3.5: Base and optimal design at different voltages

Design variable	Base	Optimal design @ dV = 0.4V	Optimal design @ dV = 0.6 V	Optimal design @ dV = 0.8V
$m_{Pt,c}$	0.2	1.0 (upper bd.)	0.9998 ( $\approx$ upper bd.)	1.0 (upper bd.)
$\epsilon_{agg,c}$	0.35	0.5430	0.6866	0.7104
$Pt C_c$	0.2	0.6719	0.7766	0.8063
$\epsilon_{V,c}^{gdl}$	0.6	0.4036	0.6461	0.6919
$m_{Pt,a}$	0.2	0.6558	0.5764	0.4589
$\epsilon_{agg,a}$	0.35	0.6839	0.6858	0.7003
$Pt C_a$	0.2	0.6358	0.6461	0.6039
$\epsilon_{V,a}^{gdl}$	0.6	0.1003 (lower bd.)	0.5856	0.6774

To conclude this discussion, the results obtained in this thesis are compared with experimental data. In the past decade, several studies have been performed to opti-

Table 3.6: Catalyst layer volume fractions for base and optimal design. Obtained from equations (2.50), (2.51), (2.52); and, (2.55)

Volume Fraction	Base	Optimal design @ dV = 0.4V	Optimal design @ dV = 0.6 V	Optimal design @ dV = 0.8V
$\epsilon_{V,c}$	0.2067	0.1986	0.2406	0.2752
$\epsilon_{N,c}$	0.4093	0.5106	0.5691	0.5581
$\epsilon_{S,c}$	0.3839	0.2907	0.1846	0.1718
$\epsilon_{V,a}$	0.2067	0.1296	0.2596	0.2777
$\epsilon_{N,a}$	0.4093	0.6520	0.5557	0.5505
$\epsilon_{S,a}$	0.3839	0.2184	0.1902	0.1666

mize the cathode electrode [46, 145, 163–165, 186, 187]. These studies have suggested that an ionomer content in the the range of 30 to 40%wt. in the catalyst layer provides the best polarization curves for oxygen as well as air fed fuel cells over a large range of operating conditions. Transforming the optimal ionomer volume fraction in Table 3.6 to a weight fraction using the equations in reference [188], the optimal ionomer weight fractions in the cathode catalyst layer are 40.69%wt., 46.92% wt. and 47.37 % wt. respectively.

These results are slightly higher than those obtained experimentally. However, the author believes that this difference is due to the optimization algorithm being able to search the design space more effectively. In the experimental studies presented in the literature [46, 145, 163–165, 186, 187], to obtain the maximum electrolyte volume fraction the electrolyte volume fraction is changed while maintaining the platinum content and the platinum to carbon ratio constant. Assuming that the catalyst layer thickness is fixed, the solid volume fraction also remains constant, as shown by equation (2.51). Gode et al. [46] reported minimal changes in catalyst layer thickness with changes in ionomer content. Gode et al. [46] and Xie et al. [165] both reported the solid phase volume fraction for catalyst layer with different ionomer contents. The solid volume fraction in these cases is almost constant with values in the range of 35 to 50%. As a result of the constant solid phase, increasing the ionomer content results

in a reduction in porosity. This is not the case in the optimization process since both platinum loading and platinum to carbon ratio are able to change and therefore, an increase in electrolyte does not necessarily reduce porosity. For this reason, electrolyte volume fraction can be further increased by the optimization algorithm.

To validate this assumption, two optimization problems are solved where the platinum loading and the platinum to carbon ratio are maintained constant at: a) 0.2 and 0.2 ( $\epsilon_S = 0.38$ ); and, b) 0.25 and 0.2 respectively ( $\epsilon_S = 0.51$ ). In this manner, only the electrolyte content inside the agglomerate in the CL and; the GDL porosity in both anode and cathode, are allowed to change. The optimizations are performed at 0.6V. For the first case, the optimal solution is obtained after 11 iterations and 15 minutes. The new design provides a current density of  $0.6877A/cm^2$ , the design variables are  $\{\epsilon_{agg,c}, \epsilon_{V,c}^{gdl}, \epsilon_{agg,a}, \epsilon_{V,a}^{gdl}\} = \{0.3661, 0.6599, 0.3678, 0.5001\}$  and the optimal ionomer content for a CL is 44.67%wt. and 44.82%wt. for the cathode and anode respectively. In the second case, the optimal solution is obtained after 13 iterations and 18 minutes. The new design provides a current density of  $0.5782A/cm^2$ , the design variables are  $\{\epsilon_{agg,c}, \epsilon_{V,c}^{gdl}, \epsilon_{agg,a}, \epsilon_{V,a}^{gdl}\} = \{0.2236, 0.5806, 0.2323, 0.4714\}$  and the optimal ionomer content for a CL is 33.76%wt. and 34.41%wt. for the cathode and anode respectively.

The optimization results show that, as the solid phase volume fraction is reduced, the electrolyte volume fraction is also reduced. Furthermore, for a solid phase volume fraction in the range of 35% to 50%, the electrolyte volume fractions are in the range of 35 to 45%wt., close to the experimental range. By looking at the current densities of the optimal designs, it is interesting to note that the second design with the higher platinum loading results in lower performance. This highlights the importance of taking into account the solid phase volume fraction in the design process and therefore, the importance of taking into account all four parameters at once.

Revisiting Table 3.6, in the numerical optimization procedure, the solid phase is not constrained to remain constant and is in fact reduced from about 40% (similar

to those in experimental studies) in the initial design to values of around 20% for the optimum designs. This reduction in solid phase creates additional space in the catalyst layer which is then used to increase both the ionomer content and the overall catalyst layer porosity. Therefore, the apparent discrepancies between experimental results and the optimization results are due to the differences in solid phase volume fractions.

These results are also consistent with data presented by Sasinkumar et al. [162] who reported that the optimum Nafion<sup>TM</sup> content increases with decreasing platinum loading, which, assuming the catalyst layer thickness to be constant, results in a reduction of the solid phase volume fraction. Furthermore, upon examination of the polarization curves reported by Sasinkumar et al., we observed that there is better fuel cell performance at high current densities with platinum loadings of  $0.1\text{mg}/\text{cm}^2$  (optimal ionomer content of 50% wt) and  $0.25\text{mg}/\text{cm}^2$  (optimal ionomer content of 40% wt) than at platinum loadings of  $0.5\text{mg}/\text{cm}^2$  where mass-transport limitations are evident. This again confirms our findings.

The results from this study and the above discussion suggest that the optimal ionomer content is dependent upon the solid phase volume fraction. It would thus be most useful in future experimental studies to simultaneously document the thickness of the catalyst layer and the volume fractions of solid, ionomer and void space. The present findings also suggest that the experimentally identified optimal ionomer content of 30-40%wt. is only optimal for a given solid phase volume fraction of 30 to 50%. Future experimental studies should be performed in order to investigate the effect of reducing the solid phase volume fraction and increasing the ionomer content to confirm if further increase in ionomer content would indeed result in further improvements in performance at high current densities, as suggested by the agglomerate model predictions. Remarkably, if such performance gains are realized, they would have no associated cost penalty. Instead, they would most likely reduce the amount of platinum required in the catalyst layer.

Table 3.7: Weights used to obtain Pareto optimal solutions

	$w_1$	$w_2$
Set 1	1.0	0.0
Set 2	0.9	0.1
Set 3	0.75	0.25
Set 4	0.5	0.5
Set 5	0.25	0.75
Set 6	0.1	0.9

### 3.4.2 Optimization of the MEA performance and cost

The previous section has shown how, in order to increase performance, platinum loading, i.e. cost, also increases. This increase is most noticeable in the cathode where platinum loading reaches its upper bound at all operating conditions. These results show that there is a trade-off between cost and performance. Therefore, these two values should both belong to the objective of the optimization problem as discussed in section 3.1.

In this section, Pareto optimal solutions are obtained for six sets of weights. Table 3.7 shows the values for the weights.  $w_1$  is the current density weight and  $w_2$  is the cost weight. The weights are selected to assign differing importance to each objective. Set 1 is equivalent to solving the performance optimization problem in the preceding section. Sets 2 and 3 give higher importance to performance; however they also penalize cost. Set 4 gives similar importance to performance and cost. Note however, that equal weights does not signify exactly equal levels of importance because these will also depend upon the values of both objectives. Set 5 and 6 give more importance to cost than to performance. Notice that a set with  $w_2$  equal to one is not included because it would result in a trivial solution. If we only minimize cost, the optimum amount of catalyst is zero. In this case there would be no reaction, and therefore, the optimum solution would yield zero cost and produce zero current density.

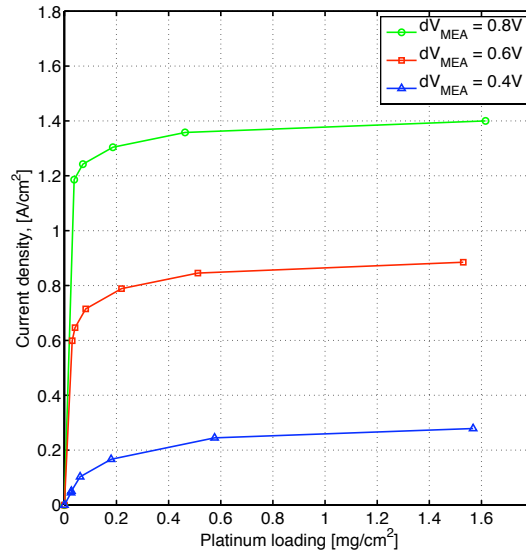


Figure 3.10: Pareto front at three different operating conditions.

Figure 3.10 shows an approximation of the Pareto fronts obtained for optimal cells operating at the three operating voltages studied in the previous section. The three Pareto fronts are obtained by solving the optimization problem in equation (3.4) with the weights in Table 3.7 at the three operating voltages. Note that each Pareto front represent the set of optimal designs at each operating voltage. All optimization problems converged, except for set 6 at high current densities. Figure 3.11 shows the evolution of the two objectives and the combined objective (left) and the evolution of the design variables for Set 3 at 0.6V voltage across the MEA. The lack of convergence for set 6 at  $dV = 0.8V$  was due to convergence problems in the analysis code at high currents and low platinum contents. The results obtained using the varying weights are well-spaced and produce a good approximation of the Pareto front. Only when cost is weighted heavily does the weight sum method start to cause cluster points in the Pareto front. At those values however, performance is already too low for any application. Therefore, in this case the sum weighted residuals is an appropriate

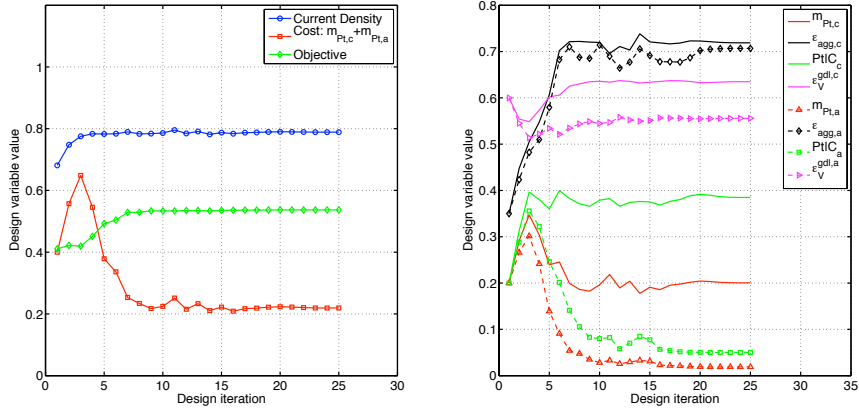


Figure 3.11: Evolution of the objectives (left) and the design variables (right) during the multiobjective optimization problem with  $w_1 = 0.75$  and  $w_2 = 0.25$  at an operating voltage of  $dV = 0.6V$ .

method to obtain the Pareto.

To further demonstrate the validity of the weight sum method in this study, Figure 3.12 shows a well-populated Pareto front and the weights used to obtain the Pareto front for a voltage across the MEA of 0.6V. The figure also shows the convexity of the Pareto front, and no discontinuities are observed. The front is well populated everywhere except at very high performance. The latter is due to the large impact of introducing cost as an objective. The blue points in Figure 3.12 are selected to show that a well distributed set of weights results in a well distributed Pareto front. Comparing the Pareto fronts in Figures 3.10 and 3.12, the Pareto front if Figure 3.10 seems a good approximation of the true Pareto front.

In Figure 3.10, the points that are on the right of each Pareto front, for each operating voltage, represent the designs obtained from solving the multiobjective optimization problem with the weight set 1, i.e. maximum performance regardless of cost. This point is obtained on each Pareto front by solving the same optimization problem for three operating voltages. As the points move towards the left, the design

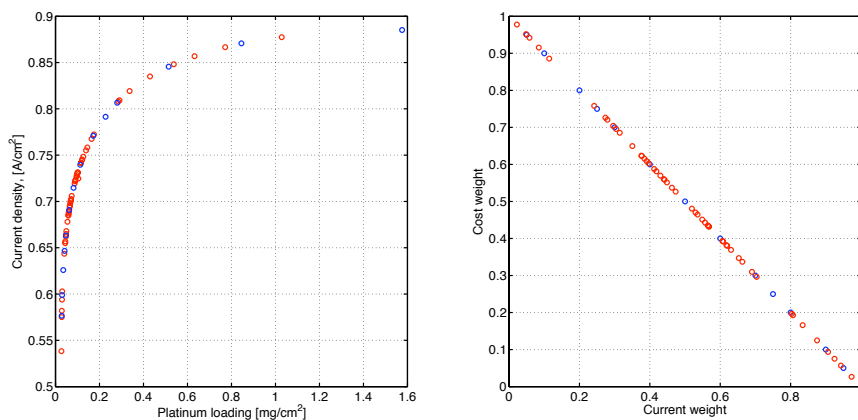


Figure 3.12: Pareto front (left) and the set of weights used to obtain the Pareto front (right) at operating condition of  $dV = 0.6V$ .

obtained from solving the optimization problem with weight sets 2 to 6 are shown. Again, by solving the optimization problem at three operating conditions, the three Pareto fronts are created. The trivial solution of zero current density for zero catalyst is also shown. By looking at the Pareto fronts, the trade-off between performance and cost can be clearly observed. The highest values of current density at any operating voltage are obtained when the platinum loadings are high, in the order of  $2mg/cm^2$ . Once cost is included as an objective, the platinum loading is reduced at the expense of performance following a similar trend at all operating voltages.

Figure 3.10 shows three very distinct areas. At the far right, the slope of the Pareto fronts is small. This means that a large increase in cost is necessary for a small increase in performance. Similarly, at the far left, the slope is very steep. In this area, a small reduction in cost produces a very large drop in performance. In the middle of the graph, with platinum loadings between  $0.1$  and  $0.6mg/cm^2$ , is where the most suitable designs can be achieved. Looking at the Pareto fronts, it is clear that the designs obtained in the previous section shown on the right of Figure 3.10 are not good designs because they offer a very poor trade-off between cost and performance.

These designs are extremely expensive when compared with the design obtained from weight set 2 which provides current densities well above  $0.8A/cm^2$  at  $0.6V$  across the MEA, at one third of the price. This result highlights the advantages of using multiobjective optimization. Inside the range of platinum loadings between  $0.1$  and  $0.6mg/cm^2$ , all designs offer some advantages and it is up to the designer to select the most appropriate design depending on the application. For example, if the fuel cell is to be used for a mass-produced automobile, maybe a design with a platinum loading of  $0.2mg/cm^2$  provides the necessary performance. However, for a one-of-a-kind high performance automobile, a design with higher platinum loadings of around  $0.6mg/cm^2$  might be more appropriate. Platinum loadings above  $0.6mg/cm^2$  are likely not to be used since the performance increase achieved by increasing platinum loading do not justify the extra cost.

Figures 3.13 and 3.14 show the values of the cathode design variables and the CL volume fraction for all designs in the Pareto curve at different operating conditions. Looking at the figures from right to left, they show the evolution of the design variables and the volume fraction as cost is given greater importance. The most interesting parameters from these curves are the platinum loading and the platinum to carbon ratio. For all operating conditions, for the optimal Pareto design with set 1, platinum loading reaches its upper bound of  $1mg/cm^2$ . As the cost objective is increased in importance, both the platinum loading and platinum to carbon ratio start to decrease. Furthermore, both curves follow a very similar trend. The reason for the similar trends can be observed by looking at the evolution of the solid phase volume fraction in Figure 3.14. Even though the platinum loading drops sharply, the solid phase volume fraction remains quite similar with a slight decrease as cost becomes more and more important. The slight decrease is mainly due to the decrease in current density that needs to be transported for the latter designs and therefore a decrease for the need for electrical conductive material in the CL. From these figures, it is clear that there is a strong connection between these two parameters so that electrical

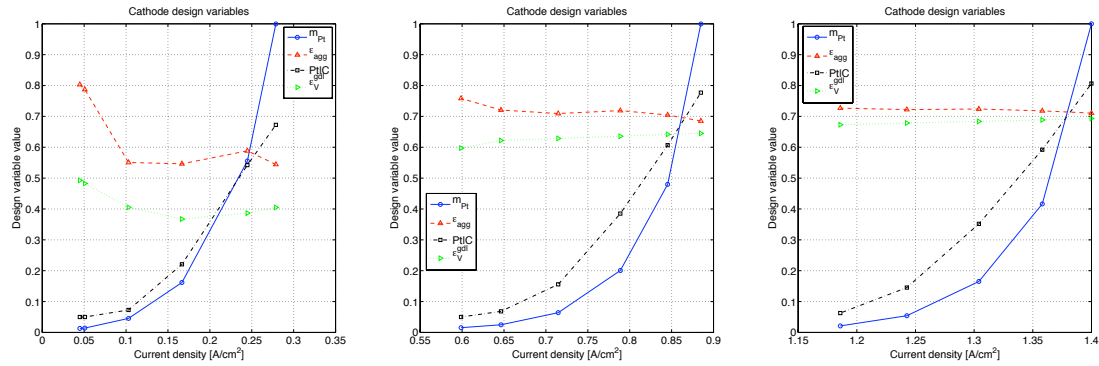


Figure 3.13: Cathode design variable values for the design given by weight sets 1 to 4 at operating conditions of  $dV = 0.4, 0.6$  and  $0.8V$ .

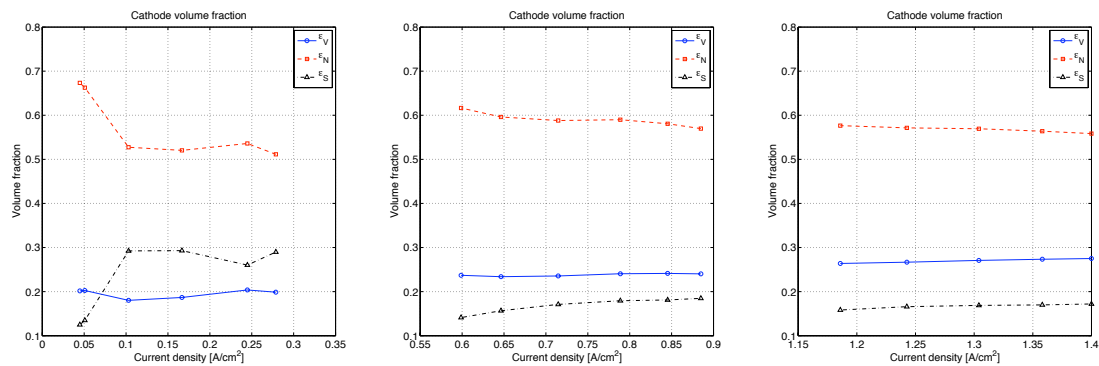


Figure 3.14: Cathode CL solid, void and electrolyte phase volume fractions for the design given by weight sets 1 to 4 at operating conditions of  $dV = 0.4, 0.6$  and  $0.8V$ .

conductivity in the CL is maintained. The electrolyte volume fraction inside the agglomerate and the GDL porosity remain almost constant regardless of the Pareto optimal solution. At medium and high currents, a slight increase in electrolyte volume fraction is observed as the cost objective weights are increased. On the other hand, GDL porosity decreases steadily as cost reduction becomes the main objective. The latter might simply be due to a decrease in current density and therefore, a reduction in the oxygen consumption. When examining the effects of operating voltage on the different designs, similar trends to the ones observed for the optimal performance case are noted, i.e. as the voltage across the MEA increases there is an increase in electrolyte volume fraction and GDL and CL porosity.

Figures 3.15 and 3.16 show the value of the anode design variables and the CL volume fraction for all designs in the Pareto curve at different operating conditions. Looking at Figure 3.15, the platinum loading is reduced by almost one order of magnitude almost immediately after cost is added to the objective. For set 1 (maximum performance at any cost) the platinum loading was of the order of  $0.5\text{mg}/\text{cm}^2$ . This value drops to almost  $0.05\text{mg}/\text{cm}^2$  in set 2 and then remains almost constant for sets 3 to 6. In a manner similar to the cathode, the platinum to carbon ratio follows the platinum loading behaviour due to their close coupling. The large reduction in platinum loading from set 1 to set 2 comes at a small expense to performance. This result is in agreement with the results in the previous section when discussing the results from the multistart strategy to test the globality of the solution. When optimizing for maximum performance, the sensitivity of the current density to anode platinum loading is very small compared to the other sensitivities; therefore, unless the convergence criteria for the optimization algorithm is very strict, the algorithm stops before reaching its optimum values which is most likely  $1.0\text{mg}/\text{cm}^2$ . The results are also in agreement with those published recently by Karan [100] and Secanell et al. [92] where an anode model was used to minimize platinum loading at a given current density. It was also shown by the authors that reducing the anode CL thickness could result

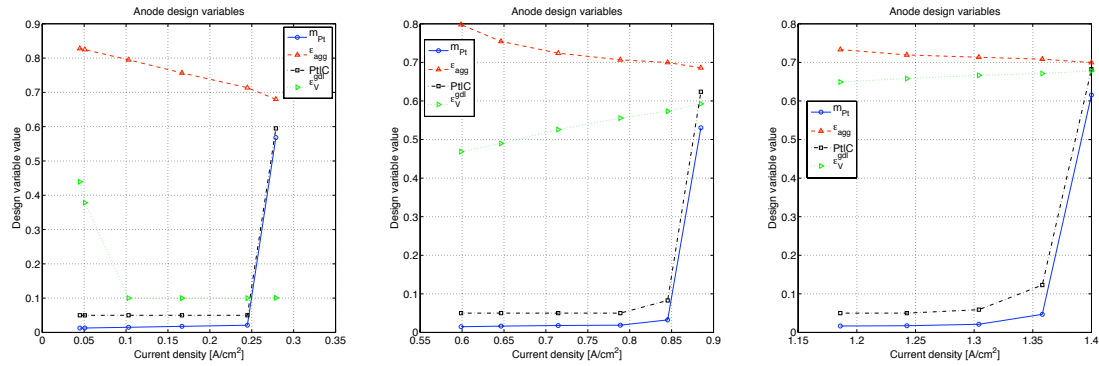


Figure 3.15: Anode design variable values for the design given by weight sets 1 to 4 at operating conditions of  $dV = 0.4, 0.6$  and  $0.8V$ .

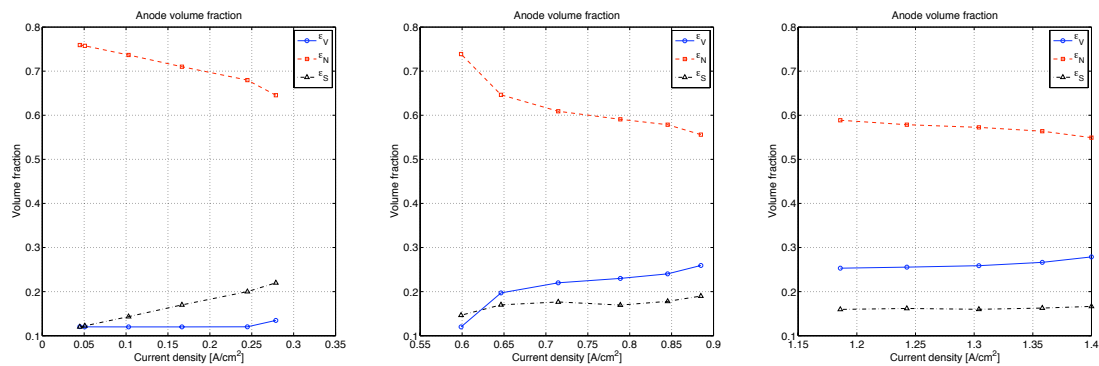


Figure 3.16: Anode CL solid, void and electrolyte phase volume fractions for the design given by weight sets 1 to 4 at operating conditions of  $dV = 0.4, 0.6$  and  $0.8V$ .

in further platinum loading reductions. Compared to the cathode, the electrolyte volume fraction inside the agglomerate and the GDL porosity also vary substantially depending on the set of weights. In particular, at medium and high current densities, as the cost weights increase, electrolyte volume fraction increases and GDL porosity decreases.

### **Final remarks**

Optimization results from the multiobjective optimization problem show that the anode and the cathode must be designed differently. Using the same composition for both the cathode and the anode will most likely yield a very expensive anode or a cathode with bad performance. These results further reinforce the importance of using optimization for fuel cell design.

Comparing the results obtained from the previous optimization formulation and the multiobjective optimization formulation, it is clear that cost must be included in the optimization objective. Otherwise, the optimal design is unnecessarily expensive and it is only optimal from a performance stand point. These results highlight the importance of a well-posed optimization problem formulation in order to obtain a good design. In this case, two optimization formulations are studied. Other possible formulations are possible such as the minimization of cost under a performance constraint [92]. The optimal design will be as good as the problem that is formulated to solve it.

Finally, it is important to note that multiobjective optimization problems provide a range of optimum designs from which to choose. This means that even though optimization can help automate a large part of the design process, design engineers will still be necessary in order to select the most appropriate design for any given application.

# Chapter 4

## Conclusions and outlook

### 4.1 Conclusions

A fuel cell analysis and design tool has been presented, namely the Fuel Cell Simulation Toolbox (FCST). This analysis and design tool is composed of a two-dimensional, through-the-channel, single-phase, isobaric and isothermal fuel cell model and a gradient-based optimization algorithm. The design tool developed has four main features: a) it uses manufacturing and structural parameters as input parameters; b) it features state-of-the-art anode and cathode electrode models; c) it is coupled to a gradient-based optimization algorithm through analytical sensitivities, and; d) it is developed using the most appropriate algorithms to reduce computational costs. This design tool has been used to obtain the optimal MEA composition for maximum performance and to study the trade-offs between performance and cost. The solution of the two optimization problems has shown the importance of designing fuel cells using a holistic approach where all design parameters are modified simultaneously.

Solving the MEA composition problem for optimal performance, it has been shown that not only the electrolyte volume fraction but also the solid phase volume fraction in the CL are paramount parameters when optimizing the CL composition. In the

past, most experimental parameters kept the solid phase volume fraction fixed. This made the designs incapable of achieving optimum performance. Once all design parameters were included in the design problem, the interdependence of the electrolyte and solid phase volume fraction could be clearly observed. Given these results, the author suggests a reduction in the solid phase volume fraction in order to achieve better CL performance. The optimization results were also compared with experimental data presented in the literature by solving a new optimization algorithm with fixed solid phase volume fraction. The optimal electrolyte content in these cases was very similar to the ones reported in the literature, thereby further validating the results.

A multiobjective optimization problem has been formulated and solved to show the trade-offs between cost and performance. These studies suggest that platinum reductions in the anode to values of less than  $0.05\text{mg}/\text{cm}^2$  would result in very small reductions in performance. Furthermore, competitive performances at any operating condition can be obtained with total platinum loadings in the order of 0.2 to 0.1  $\text{mg}/\text{cm}^2$ . Looking at Figure 3.10, for a cell voltage of 0.593V, a current density of 0.7 and 0.8  $\text{A}/\text{cm}^2$  can be achieved with platinum loadings of 0.1 and 0.2  $\text{mg}/\text{cm}^2$ . These values represent a Pt-specific power density of the cell with an optimized MEA of 0.482 and 0.422  $\text{g}_{\text{Pt}}/\text{kW}$  respectively. These values are extremely close to the target of 0.4  $\text{g}_{\text{Pt}}/\text{kW}$  for large-scale implementation [172]. Therefore, the results show that, by optimizing current PEMFC cells, targets can be met for future fuel cell commercialization. These results are even more encouraging taking into account that the optimization done in this thesis did not include optimization of geometrical or operating conditions parameters which could improve Pt utilization even further.

This thesis presented, for the first time, a design framework for fuel cells that has the potential to solve large-scale problems, i.e. three-dimensional models with thousands of design variables. In order to develop such a design framework, the algorithms in both the analysis and programs were carefully selected. Analysis and design programs were developed in-house in order to have full control of the solution

process. To speed up convergence of the analysis module Newton's algorithm is used to solve the nonlinear governing equations. This approach resulted in a reduction of computational time of almost four times with respect to other commercial software such as COMSOL. To increase computational speed and, at the same time, increase the accuracy of the results, the fuel cell governing equations are solved using adaptive finite elements. The use of adaptive finite elements provides the design tool with the ability to adapt the computational mesh to the physics of the design during the optimization program and guarantees a grid independent solution.

To decrease the computational time to solve the optimization problem a gradient-based optimization algorithm is used. Such algorithms require the gradients of the objective function and constraints with respect to the design variables. To date, in the fuel cell community, gradients were usually obtained using forward differences. This method required the solution of the analysis program as many times as design variables. In this thesis, this would have meant solving the analysis program nine times. In order to reduce computational demands, the current analysis program is modified to be able to obtain the sensitivities of the design objective and constraints using analytical sensitivities. In this way, all analytical sensitivities can be computed in less than half the time it takes to solve the analysis problem.

The combination of all computational improvements results in more than a one order of magnitude reduction in computational time when solving an optimization program with respect to the most efficient method used in the literature thus far. The most common method used in the literature is to use COMSOL as a black box together with one of MATLAB's gradient-based optimization algorithms and to obtain the sensitivities using forward differences. To analyze the difference in computational time, let us look at the performance optimization problem at an MEA voltage of 0.6V. Using the design framework presented, the optimization problem is solved in approximately 30 min and 21 iterations. Had this problem been solved using COMSOL and numerical sensitivities, it would have taken approximately 8h

$24\text{min} = 21 \cdot (8 + 1) \cdot (40 \cdot 4)$ , i.e. almost than half a day. In the last equation, 21 is the number of optimization iterations performed;  $(8 + 1)$  accounts for the number of analyses necessary to compute the numerical gradients of all design variables; and,  $40 \cdot 4$  accounts for each analysis run where 40 sec is an estimate of the time it takes to solve the problem using the code developed (an optimistic one), and 4 accounts for the increase in speed using this program. Therefore, the optimization program developed here is approximately 17 times faster than coupling an analysis program and a gradient-based optimization algorithm using a black box approach. Taking into account that a full three-dimensional simulation might take several hours, optimization for such systems is only feasible by using an approach similar to the one shown in this thesis.

In summary, this thesis presents a first of its kind, in-depth study of the potential of using numerical optimization for fuel cell design and optimization. The results are encouraging and show that numerical optimization can help designers to achieve designs that could meet current targets for commercialization. However, much work remains to be done in the areas of fuel cell analysis and design before numerical tools can achieve their full potential.

## 4.2 Outlook

This thesis has focused only on the optimization of the MEA composition under single phase conditions, with a high pressure hydrogen feed and at high stoichiometric ratios so that reactant depletion in the channel had a negligible effect. However, optimization can be applied to any range of operating conditions and for any set of design parameters. With this in mind, the outlook of this work is vast and full of challenges and opportunities in the areas of fuel cell analysis and fuel cell design.

In order to increase the range of applicability of the design process, more accurate fuel cell models need to be developed. In this work, a set of equations has been

introduced to relate ink composition parameters to the catalyst layer structure and composition. These have then been related to the CL effective properties. The relations developed do not take into account the manufacturing process and are mainly based on geometric arguments. These relations should be further developed in order to also be able to optimize the manufacturing process.

The physics governing the model could also be improved in order to increase the range of applicability of the model. The single-phase assumption should be removed in order to account for the flooding effects in the CL and for the GDL transport. To do so, a two-phase flow model needs to be developed. It has been shown in this thesis that, due to electro-osmotic drag, both hydrogen and water are being consumed in the anode, resulting in a net flux of the mixture driven by a pressure gradient. Therefore, at low pressures, anode transport is dominated by convection, and this phenomenon should be accounted for. Finally, degradation and start-up effects cannot be accounted for in this model. A transient model needs to be developed to study these phenomena.

Computational fuel cell models such as the one presented in this thesis have to be thoroughly validated against experimental data. In this thesis, the MEA model was only validated against one experimental polarization curve due to the lack of experimental data. Future work should involve the design of a straight channel fuel cell that minimizes edge effects. Using this cell operating at high stoichiometric values the cell performance for several MEAs could be obtained. The experimental data would then be compared with the computationally predicted MEA performances in order to validate the model presented in this thesis. Finally, MEAs with the proposed optimal electrode compositions should be manufactured and tested in order to validate the optimization results.

In terms of computational complexity, the model used in this thesis is two-dimensional and through-the-channel. In order to account for the channel effects and depletion of reactants as they travel along the channel a three-dimensional model

is necessary. This can be achieved using the deal.ii templates. The computational framework currently solves all governing equations with different transport coefficients in all the fuel cell domains. However, when solving the complete MEA, this leads to numerical instabilities at regions where transport properties should be zero, such as the proton conductivity in the GDL or the oxygen or water vapor diffusion coefficient in the membrane. This should be improved upon by developing a methodology to solve the domains separately and by transferring information at the boundaries as is done to solve fluid-structure interaction problems [189]. Finally, in order to solve three-dimensional problems in a reasonable amount of computational time, parallelization of the analysis program is desirable.

A summary of possible avenues of research in fuel cell analysis and computational mechanics include

- Development of relationships that relate the manufacturing process parameters to the CL structure and composition.
- Introduction of a two-phase model to the current modeling and design framework.
- Introduction of convection to model anode transport.
- Extension of the current two-dimensional model to three-dimensions.
- Transient modeling.
- Experimental validation.
- Solution of the fuel cell in different domains and efficient information transfer between domains.
- Parallelization of the program.

In terms of computational design of fuel cells, the number of possible avenues of research is even larger than those of fuel cell modeling. In this work, two optimization formulations have been presented. However, new formulations are necessary to solve multi-point optimization problems, i.e. optimizing fuel cell performance for a whole range of operating voltages. Similarly, in order to optimize the cell for degradation or start-up requirements, new optimization formulations need to be presented. The objective function for the optimization problem is not clear in this case. Furthermore, minimization of degradation or improvement of start-up capabilities would represent two *additional* objectives in addition to performance and cost, resulting in a total of four conflicting objectives, two of which require transient data. Certainly, a formulation for this problem would be a challenge.

The CL and GDL thickness are not introduced as design variables in this work. Obtaining analytical sensitivities of shape design variables represents another challenge [190]. To obtain such derivatives, several methods exist such as a semi-analytical approach, non-dimensionalization of the governing equations or a complete analytical approach which requires a mesh-deformation algorithm. Similarly, operating parameters such as oxygen partial pressure in the channel are not included in the optimization in this thesis because obtaining the analytical sensitivities of such parameters required further investigation.

In this thesis, it is assumed that design parameters such as the platinum loading are constant throughout the CL and GDL. Topology optimization allows transport parameters in each cell of the computational mesh to be treated as design variables [191]. Using this method, an optimal platinum loading distribution map could be obtained. This could be extremely interesting when performing optimization in three-dimensions. Will the largest amount of platinum be placed at the beginning of the channels where more oxygen is available? Or, will it be placed at the end in order to increase oxygen kinetics where oxygen partial pressures are lower? The answer is not clear, and it is most likely dependent upon the optimization objective and

formulation.

The manifold and the fuel cell channel layout are key components to the effective distribution of the gases. Shape and topology optimization could be applied to the design of these components in order to achieve better reactant distribution and smaller pressure drops which reduce the demands on auxiliary systems.

Finally, the optimization problems solved in this thesis did not account for the uncertainties associated with either the design parameters or the model. This could be accounted for in both the analysis and the design.

A summary of possible avenues of research in design and optimization of fuel cells include

- Multi-point optimization.
- Optimization formulations for transient objectives such as degradation minimization.
- Sensitivity analysis of geometric and operating parameters.
- Topology optimization of the electrodes.
- Topology and shape optimization of the channel layout.
- Reliability-based design optimization.

## References

- [1] T. A. Zang and L. L. Green. Multidisciplinary design and optimization techniques: Implications and opportunities for fluid dynamics research. In *30th AIAA Fluid Dynamics Conference*, Norfolk, VA, June 28 - July 1 1999.
- [2] J.R.R.A. Martins. *A Coupled-Adjoint Method for High-Fidelity Aero-structural Optimization*. PhD thesis, Stanford University, November 2002.
- [3] A. Gomes and A. Suleman. Optimization of aircraft aeroelastic response using level set methods. In *46th AIAA/ASME/ASCE/AHS/ASC Structures, Structural Dynamics and Materials Conference*, Austin, TX, April 2005.
- [4] M. Secanell and A. Suleman. Numerical evaluation of optimization algorithms for low-reynolds-number aerodynamics shape optimization. *AIAA Journal*, 43(10):2262–2267, October 2005.
- [5] G.N. Vanderplaats. *Numerical Optimization Techniques for Engineering Design with Applications*. McGraw-Hill, 1984.
- [6] A. Suleman and R. Sedaghati. Benchmark case studies in nonlinear structural optimization. *Structural and Multidisciplinary Optimization*, 29:1–24, 2005.
- [7] K. Haraldsson and K. Wipke. Evaluating PEM fuel cell system models. *Journal of Power Sources*, 126:88–97, 2004.

- [8] D. Cheddie and N. Munroe. Review and comparison of approaches to proton exchange membrane fuel cell modeling. *Journal of Power Sources*, 147(1-2):72–84, September 2005.
- [9] J.C. Amphlett, R.M. Baumert, R.F. Mann, B.A. Peppley, and P.R. Roberge. Performance modeling of the ballard mark iv solid polymer electrolyte fuel cell. i. mechanistic model development. *Journal of the Electrochemical Society*, 142(1):1–8, January 1995.
- [10] R.F. Mann, J.C. Amphlett, M.A.I Hooper, H.M. Jensen, B.A. Peppley, and P. R. Roberge. Development and application of a generalised steady state electrochemical model for a pem fuel cell. *Journal of Power Sources*, 86:173–180, 2000.
- [11] A. Z. Weber and J. Newman. Modeling transport in polymer-electrolyte fuel cells. *Chemical Reviews*, 104(10):4679–4726, October 2004.
- [12] C.-Y. Wang. Fundamental models for fuel cell engineering. *Chemical Reviews*, 104:4727–4766, 2004.
- [13] A. Biyikoğlu. Review of proton exchange membrane fuel cell models. *International Journal of Hydrogen Energy*, 30:1181–1212, 2005.
- [14] X. Li and I. Sabir. Review of bipolar plates in pem fuel cells: Flow-field designs. *International Journal of Hygrogen Energy*, 30:359–371, 2005.
- [15] W. Sun, B. A. Peppley, and K. Karan. An improved two-dimensional agglomerate cathode model to study the influence of catalyst layer structural parameters. *Electrochimica Acta*, 50(16-17):3347–3358, 2005.
- [16] A.A. Kulikovskiy, J. Divisek, and A.A. Kornyshev. Modeling the cathode compartment of polymer electrolyte fuel cells: Dead and active reaction zones. *Journal of the Electrochemical Society*, 146(11):3981–3991, November 1999.

- [17] T. Zhou and H. Liu. Effects of the electrical resistances of the gdl in a pem fuel cell. *Journal of Power Sources*, 161(1):444–453, October 2006.
- [18] J.G. Pharoah, K. Karan, and W. Sun. On effective transport coefficients in pem fuel cell electrodes: Anisotropy of the porous transport layers. *Journal of Power Sources*, 161(1):301–313, October 2006.
- [19] S. Litster and N. Djilali. Two-phase transport in porous gas diffusion electrodes. In M. Faghri and B. Sundén, editors, *Transport Phenomena in Fuel Cells*. WIT Press, 2005.
- [20] D. Song, Q. Wang, Z. Liu, T. Navessin, M. Eikerling, and S. Holdcroft. Numerical optimization study of the catalyst layer of pem fuel cell cathode. *Journal of Power Sources*, 126(1-2):104–111, 2004.
- [21] L. You and H. Liu. A parametric study of the cathode catalyst layer of PEM fuel cells using a pseudo-homogeneous model. *International Journal of Hydrogen Energy*, 26(9):991–999, September 2001.
- [22] A.C. West and T.F. Fuller. Influence of rib spacing in proton-exchange membrane electrode assemblies. *Journal of Applied Electrochemistry*, 26:557–565, 1996.
- [23] B. Hum and X. Li. Two-dimensional analysis of PEM fuel cells. *Journal of Applied Electrochemistry*, 34:205–215, 2004.
- [24] N.P. Siegel, M.W. Ellis, D.J. Nelson, and M.R. Von Spakovsky. Single domain PEMFC model based on agglomerate catalyst geometry. *Journal of Power Sources*, 115(1):81–89, March 2003.
- [25] V. Gurau, H. Liu, and S. Kakaç. Two-dimensional model for proton exchange membrane fuel cells. *AIChE Journal*, 44(11):2410–2422, 1998.

- [26] T. Berning, D.M. Lu, and N. Djilali. Three-dimensional computational analysis of transport phenomena in a pem fuel cell. *Journal of Power Sources*, 106(1-2):284–294, 2002.
- [27] G. Hu, J. Fan, S. Chen, Y. Liu, and K. Cen. Three-dimensional numerical analysis of proton exchange membrane fuel cells (PEMFCs) with conventional and interdigitated flow fields. *Journal of Power Sources*, 136(1):1–9, September 2004.
- [28] N. Djilali and D.M. Lu. Influence of heat transfer on gas and water transport in fuel cells. *Int. J. Thermal Science*, 41(1):29–40, January 2002.
- [29] D. Song, Q. Wang, Z. Liu, M. Eikerling, Z. Xie, T. Navessin, and S. Holdcroft. A method for optimizing distributions of Nafion and Pt in cathode catalyst layers of PEM fuel cells. *Electrochimica Acta*, 50(16-17):3359–3374, 2005.
- [30] J.J. Baschuk and Xianguo Li. Modelling of polymer electrolyte membrane fuel cells with variable degrees of water flooding. *Journal of Power Sources*, 86:181–196, 2000.
- [31] D.M. Bernardi and M.W. Verbrugge. Mathematical model of a gas diffusion electrode bonded to a polymer electrolyte. *AIChE Journal*, 37(8):1151–1163, August 1991.
- [32] D. M. Bernardi and M. W. Verbrugge. Mathematical model of the solid-polymer-electrolyte fuel cell. *Journal of the Electrochemical Society*, 139(9):2477–2491, September 1992.
- [33] Jeffrey T. Gostick, Michael W. Fowler, Marios A. Ioannidis, Mark D. Pritzker, Y.M. Volfkovich, and A. Sakars. Capillary pressure and hydrophilic porosity in gas diffusion layers for polymer electrolyte fuel cells. *Journal of Power Sources*, 156(2):375–3887, June 2006.

- [34] T. Berning and N. Djilali. A 3d, multiphase, multicomponent model of the cathode and anode of a PEM fuel cell. *Journal of the Electrochemical Society*, 150(12):A1589–A1598, December 2003.
- [35] Z.H. Wang, C.Y. Wang, and K.S. Chen. Two-phase flow and transport in the air cathode of proton exchange membrane fuel cells. *Journal of Power Sources*, 94(1):40–50, February 2001.
- [36] T. Berning and N. Djilali. Three-dimensional computational analysis of transport phenomena in a pem fuel cell - a parametric study. *Journal of Power Sources*, 124(2):440–452, 2003.
- [37] B.R. Sivertsen and N. Djilali. Cfd based modelling of proton exchange membrane fuel cells. *Journal of Power Sources*, 141(1):65–78, February 2005.
- [38] C. Marr and X. Li. Composition and performance modelling of catalyst layer in a proton exchange membrane fuel cell. *Journal of Power Sources*, 77(1):17–27, January 1999.
- [39] M. Eikerling and A.A. Kornyshev. Modelling the performance of the cathode catalyst layer of polymer electrolyte fuel cells. *Journal of Electroanalytical Chemistry*, 453(1-2):89–106, August 1998.
- [40] D. Bevers, M. Wöhr, K. Yasuda, and K. Oguro. Simulation of a polymer electrolyte fuel cell electrode. *Journal of Applied Electrochemistry*, 27(11):1254–1264, November 1997.
- [41] Y.W. Rho, S. Srinivasan, and Y.T. Kho. Mass transport phenomena in proton exchange membrane fuel cells using O<sub>2</sub>/He, O<sub>2</sub>/Ar, and O<sub>2</sub>/N<sub>2</sub> mixtures. II. theoretical analysis. *Journal of the Electrochemical Society*, 141(8):2089–2096, August 1994.

- [42] K. Broka and P. Ekdunge. Modelling the PEM fuel cell cathode. *Journal of Applied Electrochemistry*, 27(3):281–289, March 1997.
- [43] Frédéric Jaouen, Göran Lindbergh, and Göran Sundholm. Investigation of mass-transport limitations in the solid polymer fuel cell cathode - I. Mathematical model. *Journal of the Electrochemical Society*, 149(4):A437–A447, 2002.
- [44] J. Ihonen, F. Jaouen, G. Lindbergh, A. Lundblad, and G. Sundholm. Investigation of mass-transport limitations in the solid polymer fuel cell cathode - ii. experimental. *Journal of the Electrochemical Society*, 149(4):A448–A454, 2002.
- [45] K.L. More, R. Borup, and K.S. Reeves. Identifying contributing degradation phenomena in pem fuel cell membrane electrode assemblies via electron microscopy. *ECS Transactions*, 3(1):717–733, 2006.
- [46] Peter Gode, Frédéric Jaouen, Göran Lindbergh, Anders Lundblad, and Göran Sundholm. Influence of the composition on the structure and electrochemical characteristics of the pemfc cathode. *Electrochimica Acta*, 48:4175–4187, 2003.
- [47] M. Eikerling. Water management in cathode catalyst layers of pem fuel cells. *Journal of the Electrochemical Society*, 153(3):E58–E70, 2006.
- [48] Qianpu Wang, Michael Eikerling, Datong Song, and Zhongsheng Liu. Structure and performance of different types of agglomerates in cathode catalyst layers in PEM fuel cells. *Journal of Electroanalytical Chemistry*, 573:61–69, 2004.
- [49] R. B. Bird, W. E. Stewart, and E.N. Lightfoot. *Transport Phenomena*. J. Wiley and Sons, 2nd edition, 2002.
- [50] S.J. Ridge, R.E. White, Y. Tsou, R.N. Beaver, and G.A. Eisman. Oxygen reduction in a proton exchange membrane test cell. *Journal of the Electrochemical Society*, 136(7):1902–1909, July 1989.

- [51] D. Song, Q. Wang, Z. Liu, T. Navessin, and S. Holdcroft. Numerical study of pem fuel cell cathode with non-uniform catalyst layer. *Electrochimica Acta*, 50:731–737, 2004.
- [52] P.-C. Sui, L.-D. Chen, James P. Seaba, and Yoshinori Wariishi. Modeling and optimization of a PEMFC catalyst layer. In *SAE SP-1425, Fuel Cell for Transportation*. SAE, 1999. 1999-01-0539.
- [53] A. Z. Weber and J. Newman. Transport in polymer-electrolyte membranes: Ii. mathematical model. *Journal of the Electrochemical Society*, 151(2):A311–A325, 2004.
- [54] T.E. Springer, T.A. Zawodzinski, and S. Gottesfeld. Polymer electrolyte fuel cell model. *Journal of the Electrochemical Society*, 138(8):2334–2342, August 1991.
- [55] M. Eikerling, Yu. I. Kharkats, A. A. Kornyshev, and Yu. M. Volkovich. Phenomenological theory of electro-osmotic effect and water management in polymer electrolyte proton-conducting membranes. *Journal of the Electrochemical Society*, 145(8):2684–2699, August 1998.
- [56] J. Fimrite, H. Struchtrup, and N. Djilali. Transport phenomena in polymer electrolyte membranes. part i: Modeling framework. *Journal of the Electrochemical Society*, 152(9):A1804–A1814, 2005.
- [57] J. Fimrite, H. Struchtrup, and N. Djilali. Transport phenomena in polymer electrolyte membranes. part ii: Binary friction membrane model. *Journal of the Electrochemical Society*, 152(9):A1815–A1823, 2005.
- [58] J.S. Arora. *Introduction to Optimum Design*. McGraw-Hill, 1989.
- [59] A. Antoniou and W.-S. Lu. *Optimization: Methods, Algorithms, and Applications*. Kluwer Academic, 2003.

- [60] P.E. Gill, W. Murray, and M.H. Wright. *Practical Optimization*. Academic Press, 1981.
- [61] D.P. Bertsekas. *Constrained Optimization and Lagrange Multiplier Methods*. Academic Press, 1982.
- [62] L. Lamberti and C. Pappalettere. Comparison of the numerical efficiency of different sequential linear programming based algorithms for structural optimization problems. *Computers and Structures*, 76(6):713–728, July 2000.
- [63] P.T. Boggs and J.W. Tolle. Sequential quadratic programming. *Acta Numerica*, 4:1–51, 1995.
- [64] A. El-Barky, R. Tapia, T. Tshchiya, and Y. Zhang. On the formulation and theory of the newton interior point method for nonlinear programming. *Journal of Optimization Theory and Applications*, 89(3):507–541, 1996.
- [65] G.G. Wang, Z. Dong, and P. Aitchison. Adaptive response surface method - a global optimization scheme for approximation-based design problems. *Engineering Optimization*, 33:707–733, 2001.
- [66] J.F. Rodríguez, J.E. Renaud, B.A. Wujek, and R.V. Tappeta. Trust region management is multidisciplinary design optimization. *Journal of Computational and Applied Mathematics*, 124:139–154, 2000.
- [67] T.-Y. Chen. Calculation of the move limits for the sequential linear programming method. *International Journal for Numerical Methods in Engineering*, 36:2661–2679, 1993.
- [68] J.C. Meza, R.A. Oliva, P.D. Hough, and P.J. Williams. OPT++: An object-oriented toolkit for nonlinear optimization. *ACM Transactions on Mathematical Software*, 33(2):1–27, June 2007.

- [69] M.S. Eldred, A.A. Giunta, B.G. van Bloemen Waanders, Jr. S.F. Wojtkiewicz, W.E. Hart, and M.P. Alleva. Dakota, a multilevel parallel object-oriented framework for design optimization, parameter estimation, uncertainty quantification, and sensitivity analysis. version 3.0 users manual. Technical Report 2001-3796, Sandia National Laboratory, 2003.
- [70] F.Schoen. Stochastic techniques for global optimization: A survey on recent advances. *Journal of Global Optimization*, 1(3):207–228, 1991.
- [71] L. He and E. Polak. Multistart method with estimation scheme for global satisfying problems. *Journal of Global Optimization*, 3:139–156, 1993.
- [72] M. Dorigo, V. Maniezzo, and A. Coloni. The ant system: Optimization by colony of cooperating agents. *IEEE Transactions on Systems, Man and Cybernetics, Part B*, 1996.
- [73] R.P. Ge and Y.F. Qin. A class of filled functions for finding global minimizers of a function of several variables. *Journal of Optimization Theory and Applications*, 54(2):241–252, 1987.
- [74] E.R. Hansen. *Global Optimization Using Interval Analysis*. Dekker, 1992.
- [75] D.E. Golberg. *Genetic Algorithms in Search, Optimization, and Machine Learning*. Addison-Wesley, 1989.
- [76] Z. Michalewicz. *Genetic Algorithms + Data Structure = Evolution Programs*. Springer-Verlag, 1994.
- [77] E. Aarts and J. Korst. *Simulated Annealing and Boltzman Machines*. J. Wiley and Sons, 1989.
- [78] J.R.R.A. Martins, I.M. Kroo, and J.J. Alonso. An automated method for sensitivity analysis using complex variables. In *38th Aerospace Sciences Meeting and Exhibit*, Reno, NV, January 10-13 2000.

- [79] W. K. Anderson, J. C. Newman, D. L. Whitfield, and E. J. Nielsen. Sensitivity analysis for Navier-Stokes equations in unstructured meshes using complex variables. *AIAA Journal*, 39(1):56–63, January 2001.
- [80] J. R. R. A. Martins, P. Sturdza, and J. J. Alonso. The complex-step derivative approximation. *ACM Transactions on Mathematical Software*, 29(3):245–262, September 2003.
- [81] J. R. R. A. Martins, P. Sturdza, and J. J. Alonso. The connection between the complex-step derivative approximation and algorithmic differentiation. In *Proceedings of the 39th Aerospace Sciences Meeting, Reno, NV*, number AIAA Paper 2001-0921, 2001.
- [82] C. Bischof, A. Carle, G. Corliss, A. Griewank, and P. Hovland. ADIFOR - Generating derivative codes from fortran programs. *Scientific Programming*, 1(1):1–29, 1992.
- [83] L. L. Sherman, A. C. Taylor III, L. L. Green, P. A. Newman, G. W. Hou, and V. M. Korivi. First- and second-order aerodynamic sensitivity derivatives via automatic differentiation with incremental iterative methods. *Journal of Computational Physics*, 129:30–331, 1996.
- [84] A. Jameson. Aerodynamic design via control theory. *Journal of Scientific Computing*, 3(3):233–260, 1988.
- [85] M. Grujicic and K.M. Chittajallu. Design and optimization of polymer electrolyte membrane (PEM) fuel cells. *Applied surface science*, 227:56–72, 2004.
- [86] M. Grujicic and K.M. Chittajallu. Optimization of the cathode geometry in the polymer electrolyte membrane (PEM) fuel cells. *Chemical Engineering Science*, 59:5883–5895, 2004.

- [87] M. Grujicic, C.L. Zhao, K.M. Chittajallu, and J.M. Ochterbeck. Cathode and interdigitated air distributor geometry optimization in polymer electrolyte membrane (PEM) fuel cells. *Materials Science and Engineering B*, 108:241–252, 2004.
- [88] A. Mawardi, F. Yang, and R. Pitchumani. Optimization of the operating parameters of a proton exchange membrane fuel cell for maximum power density. *Journal of Fuel Cell Science and Technology*, 2(2):121–135, May 2005.
- [89] M. Secanell, B. Carnes, A. Suleman, and N. Djilali. A PEM fuel cell cathode model for gradient-based optimization. In *III European Conference on Computational Mechanics*. ECCOMAS, June 3 -5 2006.
- [90] M. Secanell, B. Carnes, A. Suleman, and N. Djilali. Numerical optimization of proton exchange membrane fuel cell cathodes. *Electrochimica Acta*, 52(7):2668–2682, 2007.
- [91] M. Secanell, K. Karan, A. Suleman, and N. Djilali. Multi-variable optimization of PEMFC cathodes using an agglomerate model. *Electrochimica Acta*, 52(22):6318–6337, June 2007.
- [92] M. Secanell, K. Karan, A. Suleman, and N. Djilali. Optimal design of ultra-low platinum pemfc anode electrodes. *Journal of the Electrochemical Society*, Submitted June 15th, 2007.
- [93] The MathWorks Inc, Natick, MA. *MATLAB - The language of technical computing*, 6th edition, 2000.
- [94] John Newman and Karen E. Thomas-Alyea. *Electrochemical systems*. John Wiley & Sons, third edition edition, 2004.
- [95] R. Taylor and R. Krishna. *Multicomponent Mass Transfer*. Series in Chemical Engineering. John Wiley & Sons, New York, 1st edition, 1993.

- [96] Arvind Parthasarathy, Supramaniam Srinivasan, A. John Appleby, and Charles R. Martin. Pressure dependence of the oxygen reduction reaction at the platinum microelectrode/naion interface: Electrode kinetics and mass transport. *Journal of the Electrochemical Society*, 139(9):2530–2537, 1992.
- [97] Arvind Parthasarathy, Supramaniam Srinivasan, A. John Appleby, and Charles R. Martin. Temperature dependence of the electrode kinetics of oxygen reduction at the platinum/naion interface—a microelectrode investigation. *Journal of the Electrochemical Society*, 139(10):2856–2862, 1992.
- [98] E-TEK. Specifications for c-1: Hp platinum on Vulcan XC-72. *www.etek-inc.com*, Data accessed on February 2, 2007.
- [99] J.G.Pharaoh, D. Harvey, and K. Karan. Comparison of catalyst treatments for PEM fuel cell modelling. In *4th ASME Conference on Fuel Cell Science, Engineering and Technology*, Irvine, California, June 19-21 2006.
- [100] K. Karan. Assessment of transport-limited catalyst utilization for engineering of ultra-low pt loading polymer electrolyte fuel cell anodes. *Electrochemistry Communications*, 9(4):747–753, April 2007.
- [101] D. A. G. Bruggeman. Calculation of the various physical constants of heterogeneous substances. I: Dielectric constants and conductivities of mixtures of isotropic substances. *Ann. Physik.*, 25:636–664, 1935.
- [102] A.S. Ioselevich and A.A. Kornyshev. Approximate symmetry laws for percolation in complex systems: Percolation in polydisperse composites. *Physical Review E (Statistical, Nonlinear, and Soft Matter Physics)*, 65(2):021301/1–11, February 2002.
- [103] Dietrich Stauffer and Amnon Aharony. *Introduction to Percolation Theory*. Taylor & Francis, London, 2nd edition, 1992.

- [104] Manolis M. Tomadakis and Stratis V. Sotirchos. Ordinary and transition regime diffusion in random fiber structures. *AIChE Journal*, 39(3):397–412, 1993.
- [105] J.H.Nam and M.Kaviany. Effective diffusivity and water-saturation distribution in single- and two-layer PEMFC diffusion medium. *International Journal of Heat and Mass Transfer*, 46:4595–4611, 2003.
- [106] Frano Barbir. *PEM Fuel Cells: Theory and Practice*. Elsevier Academic Press, 2005.
- [107] Wolf Vielstich, Arnold Lamm, and Hubert Gasteiger. *Handbook of Fuel Cells: Fundamentals, Technology, Applications*. Wiley, 2003.
- [108] M. Eikerling, A.S. Ioselevich, and A.A. Kornyshev. How good are the electrodes we use in pefc? (understanding structure vs. performance of membrane-electrode assemblies). *Fuel Cells*, 4(3):131–140, August 2004.
- [109] A. Ioselevich, A.A. Kornyshev, and W. Lehnert. Degradation of solid oxide fuel cell anodes due to sintering of metal particles. correlated percolation model. *Journal of the Electrochemical Society*, 144(9):3010–3019, Sep 1997.
- [110] M.B. Isichenko. Percolation, statistical topography, and transport in random media. *Review of Modern Physics*, 64(4):961–1043, 1992.
- [111] J. Abel, A.A. Kornyshev, and W. Lehnert. Correlated resistor network study of porous solid oxide fuel cell anodes. *Journal of the Electrochemical Society*, 144(12):4253–4259, Dec 1997.
- [112] A. Ioselevich, A.A. Kornyshev, and W. Lehnert. Statistical geometry of reaction space in porous cermet anodes based on ion-conducting electrolytes patterns of degradation. *Solid State Ionics*, 124(3):221–237, September 1999.

- [113] I.E. Baranov, S.A. Grigoriev, D.Ylitalo, V.N. Fateev, and I.I. Nikolaev. Transfer processes in pem fuel cells: Influence of electrode structure. *International Journal of Hydrogen Energy*, 31:203–210, 2006.
- [114] Z.Ball, H.M.Phillips, D.L. Callahan, and R. Sauerbrey. Percolative metal-insulator transition in excimer laser irradiated polyimide. *Physical Review Letters*, 73(15):2099–2103, October 1994.
- [115] D. Pantea, H. Darmstadt, S. Kaliaguine, and C. Roy. Electrical conductivity of conductive carbon blacks: influence of surface chemistry and topology. *Applied Surface Science*, 217(1-4):181–193, 2003.
- [116] W. Bangerth, R. Hartmann, and G. Kanschat. deal.II *Differential Equations Analysis Library, Technical Reference*.
- [117] W. H. Press, S. A. Teukolsky, W.T. Vetterling, and B.P. Flannery. *Numerical Recipes in C++: The Art of Scientific Computing*. Cambridge University Press, Cambridge, 2nd edition, 2002.
- [118] K. Yosida. *Functional analysis*. Springer-Verlag, Berlin, 1965.
- [119] David G. Luenberger. *Optimization by vector space methods*. John Wiley & Sons, New York, 1969.
- [120] R. Barrett, M. Berry, T. F. Chan, J. Demmel, J. Donato, J. Dongarra, V. Eijkhout, R. Pozo, C. Romine, and H. Van der Vorst. *Templates for the Solution of Linear Systems: Building Blocks for Iterative Methods*. SIAM, Philadelphia, PA, 2nd edition, 1994.
- [121] T. A. Davis. A column pre-ordering strategy for the unsymmetric-pattern multifrontal method. *ACM Transactions on Mathematical Software*, 30(2):165–195, 2004.

- [122] T. A. Davis. Algorithm 832: Umfpack, an unsymmetric-pattern multifrontal method. *ACM Transactions on Mathematical Software*, 30(2):196–199, June 2004.
- [123] D. W. Kelly, J. P. de S. R. Gago, O. C. Zienkiewicz, and I. Babuska. A posteriori error analysis and adaptive processes in the finite element method: Part i - error analysis. *International Journal for Numerical Methods in Engineering*, 19(11):1593–1619, November 1983.
- [124] Tony Thampan, Sanjiv Malhotra, Hao Tang, and Ravindra Datta. Modeling of conductive transport in proton-exchange membranes for fuel cells. *Journal of the Electrochemical Society*, 147(9):3242–3250, 2000.
- [125] Adam Z. Weber and John Newman. Transport in polymer-electrolyte membranes: I. physical model. *Journal of the Electrochemical Society*, 150(7):A1008–A1015, 2003.
- [126] Adam Z. Weber and John Newman. Transport in polymer-electrolyte membranes: Iii. model validation in a simple fuel-cell model. *Journal of the Electrochemical Society*, 151(2):A326–A339, 2004.
- [127] Sathya Motupally, Aaron J. Becker, and john W. Weidner. Diffusion of water in Nafion 115 membranes. *Journal of the Electrochemical Society*, 147(9):3171–3177, 2000.
- [128] James T. Hinatsu, Minoru Mizuhata, and Hiroyasu Takenaka. Water uptake of perfluorosulfonic acid membranes for liquid water and water vapour. *Journal of the Electrochemical Society*, 141(6):1493–1498, June 1994.
- [129] Peter Berg, Keith Promislow, Jean St. Pierre, Jürgen Stumper, and Brian Wetton. Water management in PEM fuel cells. *Journal of the Electrochemical Society*, 151(3):A341–A353, 2004.

- [130] A. A. Shah, G. S. Kim, W. Gervais, A. Young, K. Promislow, J. Li, and S. Ye. The effects of water and microstructure on the performance of polymer electrolyte fuel cells. *Journal of Power Sources*, 160:1251–1268, 2006.
- [131] K. C. Neyerlin, Wenbin Gu, Jacob Jorne, and Hubert A. Gasteiger. Study of the exchange current density for the hydrogen oxidation and evolution reactions. *Journal of the Electrochemical Society*, 154(7):B631–B635, 2007.
- [132] Jia X. Wang, Thomas E. Springer, and Radoslav R. Adzic. Dual-pathway kinetic equation for the hydrogen oxidation reaction on pt electrodes. *Journal of the Electrochemical Society*, 153(9):A1732–A1740, 2006.
- [133] A. A. Kulikovskiy, T. Wüster, A. Egmen, and D. Stolten. Analytical and numerical analysis of PEM fuel cell performance curves. *Journal of the Electrochemical Society*, 152(6):A1290–A1300, 2005.
- [134] B. Carnes and N. Djilali. Systematic parameter estimation for PEM fuel cell models. *Journal of Power Sources*, 144(1):83–93, June 2005.
- [135] B. Carnes and N. Djilali. Analysis of coupled proton and water transport in a PEM fuel cell using the binary friction membrane model. *Electrochimica Acta*, 52:1038–1052, 2006.
- [136] Guangyu Lin, Wensheng He, and Trung Van Nguyen. Modeling liquid water effects in the gas diffusion and catalyst layers of the cathode of a PEM fuel cell. *Journal of the Electrochemical Society*, 151(12):A1999–A2006, 2004.
- [137] Guangyu Lin and Trung Van Nguyen. A two-dimensional two-phase model of a PEM fuel cell. *Journal of the Electrochemical Society*, 153(2):A372–A382, 2006.
- [138] K. Broka and P. Ekdunge. Oxygen and hydrogen permeation properties and water uptake of nafion 117 membrane and recast film for PEM fuel cell. *Journal of Applied Electrochemistry*, 27:117–123, 1997.

- [139] Tetsuo Sakai, Hiroyasu Takenaka, Noboru Wakabayashi, Yoji Kawami, and Eiichi Torikai. Gas permeation properties of solid polymer electrolyte (SPE) membranes. *Journal of the Electrochemical Society*, 132(6):1328–1332, 1985.
- [140] Tetsuo Sakai, Hiroyasu Takenaka, and Eiichi Torikai. Gas diffusion in the dried and hydrated nafions. *Journal of the Electrochemical Society*, 133(1):88–92, 1986.
- [141] Yu-Min Tsou, M.C. Kimble, and R. E. White. Hydrogen diffusion, solubility and water uptake in dow’s short-side-chain perfluorocarbon membranes. *Journal of the Electrochemical Society*, 139(7):1913–1917, 1992.
- [142] Peter Gode, Göran Lindbergh, and Göran Sundholm. In-situ measurements of gas permeability in fuel cell membranes using a cylindrical microelectrode. *Journal of Electroanalytical Chemistry*, 518:115–122, 2002.
- [143] R. F. Mann, J.C. Amphlett, B. A. Peppley, and C.P. Thurgood. Henry’s law and the solubilities of reactant gases in the modeling of PEM fuel cells. *Journal of Power Sources*, 161:768–774, 2006.
- [144] Guido Bender, Mahlon S. Wilson, and Thomas A. Zawodzinski. Further refinements in the segmented cell approach to diagnosing performance in polymer electrolyte fuel cells. *Journal of Power Sources*, 123(2):163–171, September 2003.
- [145] S.J. Lee, S. Mukerjee, J. McBreen, Y.W. Rho, Y.T. Kho, and T.H.Lee. Effects of nafion impregnation on performances of pemfc electrodes. *Electrochimica Acta*, 43(24):3693–3701, 1998.
- [146] E. L. Cussler. *Diffusion : Mass Transfer in Fluid Systems*. Cambridge University Press, 2nd edition, 1997.

- [147] S. Chen and A.Kucernak. Electrocatalysis under conditions of high mass transport rate: Oxygen reduction on single submicrometer-sized pt particles supported on carbon. *Journal of Physical Chemistry B*, 108(10):3262–3276, 2004.
- [148] K. C. Neyerlin, Wenbin Gu, Jacob Jorne, and Hubert A. Gasteiger. Determination of catalyst unique parameters for the oxygen reduction reaction in a PEMFC. *Journal of the Electrochemical Society*, 154(10):A1955–A1963, 2006.
- [149] Lin Wang, Attila Husar, Tianhong Zhou, and Hongtan Liu. A parametric study of pem fuel cell performances. *International Journal of Hydrogen Energy*, 28(11):1263–1272, November 2003.
- [150] Lin Wang and Hongtan Liu. Performance studies of pem fuel cells with interdigitated flow fields. *Journal of Power Sources*, 134(2):185–196, August 2004.
- [151] Jürgen Stumper, Stephen A. Campbell, David P. Wilkinson, Mark C. Johnson, and Mike Davis. In-situ methods for the determination of current distributions in pem fuel cells. *Electrochimica Acta*, 43(24):3773–3783, 1998.
- [152] A. Hakenjos, K. Tüber, J.O. Schumacher, and C. Hebling. Characterizing PEM fuel cell performance using a current distribution measurement in comparison with a CFD model. *Fuel Cells*, 4(3):185–189, 2004.
- [153] Dilip Natarajan and Trung Van Nguyen. Current distribution in pem fuel cells. part 1: Oxygen and fuel flow rate effects. *AIChE Journal*, 51(9):2587–2598, 2005.
- [154] Dilip Natarajan and Trung Van Nguyen. Current distribution in pem fuel cells. part 2: Air operation and temperature effect. *AIChE Journal*, 51(9):2599–2608, September 2005.
- [155] Dilip Natarajan and Trung Van Nguyen. Effect of electrode configuration and

- electronic conductivity on current density distribution measurements in pem fuel cells. *Journal of Power Sources*, 135(1):95–109, September 2004.
- [156] Daniel J. L. Brett, Stephen Atkins, Nigel P. Brandon, Velisa Vesovic, Nikos Vasileiadis, and Anthony R. Kucernak. Measurement of the current distribution along a single flow channel of a solid polymer fuel cell. *Electrochemistry Communications*, 3(11):628–632, November 2001.
- [157] T. Hottinen, M. Nojonen, T. Mennola, O. Himanen, M. Mikkola, and P. Lund. Effect of ambient conditions on performance and current distribution of a polymer electrolyte membrane fuel cell. *Journal of Applied Electrochemistry*, 33:265–271, 2003.
- [158] COMSOL. *COMSOL 3.2 Multiphysics User's Guide*, September 2005.
- [159] R. Songprakorp. *Investigation of Dynamic Behaviors of Proton Exchange Fuel Cells*. PhD thesis, University of Victoria, to be submitted in 2008.
- [160] Lixin You and Hongtan Liu. A two-phase flow and transport model for the cathode of PEM fuel cells. *International Journal of Heat and Mass Transfer*, 45:2277–2287, 2002.
- [161] P.C. Sui and N. Djilali. Analysis of coupled electron and mass transport in the gas diffusion layer of a pem fuel cell. *Journal of Power Sources*, 161(1):294–300, October 2006.
- [162] G. Sasikumar, J.W. Ihm, and H. Ryu. Optimum Nafion content in PEM fuel cell electrodes. *Electrochimica Acta*, 50(2-3):601–605, 2004.
- [163] E. Passalacqua, F. Lufrano, G. Squadrito, A. Patti, and L. Giorgi. Nafion content in the catalyst layer of polymer electrolyte fuel cells: effects on structure and performance. *Electrochimica Acta*, 46:799–805, 2001.

- [164] E. Antolini, L. Giorgi, A. Pozio, and E. Passalacqua. Influence of nafion loading in the catalyst layer of gas-diffusion electrodes for pemfc. *Journal of Power Sources*, 77:136–142, 1999.
- [165] Zhong Xie, Titichai Navessin, Ken Shi, Robert Chow, Qianpu Wang, Datong Song, Bernhard Andreaus, Michael Eikerling, Zhongsheng Liu, and Steven Holdcroft. Functionally graded cathode catalyst layers for polymer electrolyte fuel cells. II. experimental study of the effects of nafion distribution. *Journal of the Electrochemical Society*, 152(6):A1171–A1179, 2005.
- [166] N. Cunningham, E. Irissou, M. Lefevre, M.-C. Denis, D. Guay, and J.-P. Dodelet. Pemfc anode with very low pt loadings using pulsed laser deposition. *Electrochemical and Solid-State Letters*, 6(7):A125–8, July 2003.
- [167] S. Mukerjee, S. Srinivasan, and A. J. Appleby. Effect of sputtered film of platinum on low platinum loading electrodes on electrode kinetics of oxygen reduction in proton exchange membrane fuel cells. *Electrochimica Acta*, 38(12):1661–1669, August 1993.
- [168] M. S. Saha, A. F. Gulla, R. J. Allen, and S. Mukerjee. High performance polymer electrolyte fuel cells with ultra-low pt loading electrodes prepared by dual ion-beam assisted deposition. *Electrochimica Acta*, 51(22):4680–4692, July 2006.
- [169] W. Li, L. Huyse, and S. Padula. Robust airfoil optimization to achieve drag reduction over a range of mach numbers. *Structural and Multidisciplinary Optimization*, 24:38–50, 2002.
- [170] David W. Zingg and Samy Elias. Aerodynamic optimization under a range of operating conditions. *AIAA Journal*, 11(44):2787–2792, November 2006.
- [171] M. F. Mathias, R. Makharia, H. A. Gasteiger, J. J. Conley, T. J. Fuller, C. J. Gittleman, S. S. Kocha, D. P. Miller, C. K. Mittelsteadt, T. Xie, S. G. Van, and

- P. T. Yu. Two fuel cell cars in every garage? *Electrochemical Society Interface*, 14(3):24–35, Fall 2005.
- [172] H.A. Gasteiger, J.E. Panels, and S.G. Yan. Dependence of PEM fuel cell performance on catalyst loading. *Journal of Power Sources*, 127:162–171, 2004.
- [173] Paola Costamagna and Supramaniam Srinivasan. Quantum jumps in the PEMFC science and technology from the 1960s to the year 2000. part i. fundamental scientific aspects. *Journal of Power Sources*, 102:242–252, 2001.
- [174] E-TEK. E-tek product catalogue. <http://www.etek-inc.com>, (Accessed Nov. 2006).
- [175] S. Litster and G. McLean. PEM fuel cell electrodes. *Journal of Power Sources*, 130(1-2):61–76, May 2004.
- [176] I. Das. Multi-objective optimization. <http://www-fp.mcs.anl.gov/otc/Guide/OptWeb/multiobj>, (Accessed July 2007).
- [177] I.Y. Kim and O.L. de Weck. Adaptive weighted sum method for bi-objective optimization: Pareto front generation. *Structural and Multidisciplinary Optimization*, 29:149–158, 2005.
- [178] Jiguan G. Lin. Multiple-objective problems: Pareto-optimal solutions by method of proper equality constraints. *IEEE Transactions on Automatic Control*, 21(5):641–650, October 1976.
- [179] Wolfram Stadler, editor. *Multicriteria optimization in engineering and in the sciences*. Plenum Press, 1988.
- [180] I.Y. Kim and O.L. de Weck. Adaptive weighted sum method for multiobjective optimization: a new method for pareto front generation. *Structural and Multidisciplinary Optimization*, 31:105–116, 2006.

- [181] Achille Messac and Christopher A. Mattson. Normal constraint method with guarantee of even representation of complete pareto frontier. *AIAA Journal*, 42(10):2101–2111, October 2004.
- [182] I. Das and J.E. Dennis. Normal-boundary intersection: a new method for generation pareto optimal points in multicriteria optimization problems. *SIAM Journal of Optimization*, 8:631–657, 1998.
- [183] I. Das and J.E. Dennis. A closer look at drawbacks of minimizing weighted sums of objectives for Pareto set generation in multicriteria optimization problems. *Structural Optimization*, 14:63–69, 1997.
- [184] D.G. Cacuci. *Sensitivity and Uncertainty Analysis: Theory*, volume 1. Chapman and Hall/CRC, Boca Raton, Florida, USA, 2003.
- [185] M. Secanell, B. Carnes, A. Suleman, and N. Djilali. Numerical optimization of proton exchange membrane fuel cell cathodes. *Electrochimica Acta*, 52(7):2668–2682, 2007.
- [186] Jian Xie, Karren L. More, Thomas A. Zawodzinski, and Wayne H. Smith. Porosimetry of meas made by "thin film decal" method and its effects on performance of PEFCs. *Journal of the Electrochemical Society*, 151(11):A1841–A1846, 2004.
- [187] Guangchun Li and Peter G. Pickup. Ionic conductivity of PEMFC electrodes. *Journal of the Electrochemical Society*, 150(11):C745–C752, 2003.
- [188] Qianpu Wang, Michael Eikerling, Datong Song, Zhongsheng Liu, Titichai Navessin, Zhong Xie, and Steven Holdcroft. Functionally graded cathode catalyst layers for polymer electrolyte fuel cells. I. theoretical modeling. *Journal of the Electrochemical Society*, 151(7):A950–A957, 2004.

- [189] Gonçalo Pedro. *A General Purpose, Modular Computational Platform for Fluid-Structure Interaction Problems*. PhD thesis, University of Victoria, 2005.
- [190] Bijan Mohammadi and Olivier Pironneau. *Applied Shape Optimization for Fluids*. Oxford University Press, 2001.
- [191] M.P. Bendsøe and O. Sigmund. *Topology Optimization*. Springer-Verlag, 2nd edition, 2003.